MICROCOPY RESOLUTION TEST CHART
NATIONAL BUREAU OF STANDARDS-1963-A

AD

MODELS FOR MUNITION DUST CLOUDS

JUNE 1979

Prepared by

JAMES H. THOMPSON

General Electric Company
Center For Advanced Studies
Santa Barbara, California 93102

D D C
RECEIVED
AUG 6 1979
E

US Army Electronics Research and Development Command
ATOMSPHERIC SCIENCES LABORATORY
White Sands Missile Range, NM 88002

79 08 02 101

NOTICES

Disclaimers

The findings in this report are not to be construed as an official Department of the Army position, unless so designated by other authorized documents.

The citation of trade names and names of manufacturers in this report is not to be construed as official Government indorsement or approval of commercial products or services referenced herein.

Disposition

Destory this report when it is no longer needed. Do not return it to the originator.

(18) ERADCOM/ASL

REPORT DOCUMENTATION PAGE

READ INSTRUCTIONS
BEFORE COMPLETING FORM

1. REPORT NUMBER	2. GOVT ACCESSION NO.	3. RECIPIENT'S CATALOG NUMBER
ASL-CR-79-0005-2		

4. TITLE (and Subtitle)	5. TYPE OF REPORT & PERIOD COVERED
Models for Munition Dust Clouds.	Final Report.
	6. PERFORMING ORG. REPORT NUMBER
	GE78TMP-99

7. AUTHOR(s)	8. CONTRACT OR GRANT NUMBER(s)
James H. Thompson	DAAD07-78-C-0005

9. PERFORMING ORGANIZATION NAME AND ADDRESS	10. PROGRAM ELEMENT, PROJECT, TASK AREA & WORK UNIT NUMBERS
General Electric Company - TEMPO 816 State Street Santa Barbara, CA 93102	DA Task 1L162111AH71

11. CONTROLLING OFFICE NAME AND ADDRESS	12. REPORT DATE
US Army Electronics Research and Development Command	June 1979
	13. NUMBER OF PAGES
	114

14. MONITORING AGENCY NAME & ADDRESS(if different from Controlling Office)	15. SECURITY CLASS. (of this report)
US Army Atmospheric Sciences Laboratory White Sands Missile Range, NM 88002	Unclassified
	15a. DECLASSIFICATION/DOWNGRADING SCHEDULE

16. DISTRIBUTION STATEMENT (of this Report)

(12) 118 p.

Approved for public release; distribution unlimited.

17. DISTRIBUTION STATEMENT (of the abstract entered in Block 20, if different from Report)

18. SUPPLEMENTARY NOTES

Contract Monitor: Roberto Rubio

19. KEY WORDS (Continue on reverse side if necessary and identify by block number)

Dust
Dust Clouds
Battlefield environment
Tactical munitions
Radiation transport

20. ABSTRACT (Continue on reverse side if necessary and identify by block number)

This report presents models for the dust clouds which are produced by battlefield munitions impacting the ground. Models are developed for:

- Dust mass lofted into the cloud,
- Cloud rise and expansion time history,
- Dust mass distribution within the cloud,
- Dust particle wind transport, diffusion, and fallout,

(continued)

DD FORM 1473 EDITION OF 1 NOV 65 IS OBSOLETE
1 JAN 73

346420

20. ABSTRACT (cont)

- Dust particle size probability distributions ; *and*
- Radiation cross sections of the dust particles .

2

CONTENTS

ILLUSTRATIONS

TABLES

6

SECTION 1
INTRODUCTION

There are a wide variety of electro-optical (E-O) sensors employed
in the modern tactical battlefield environment. Models for all sources
of degradation are required before the battlefield performance of these
E-O sensors can be predicted. The two categories of degradation sources
are the ambient (adverse weather, wind driven dust, etc.) and the battle-
field induced contaminants (BIC, any adverse sources introduced by man).
The two major BIC sources are countermeasures smoke and the dust clouds
due to tactical munitions impacting the ground. In this report we begin
the task of modeling the munitions dust clouds.

The dust models we will develop will be the first generation models.
As more information, primarily experimental, becomes available, succeed-
ing improved generations of models can be developed. Our data sources,
both theoretical and experimental, are severely limited at this time.
Because of the importance of tactical dust clouds, a series of test
programs have begun. In November and December of 1977 six dust cloud
tests were conducted at the Dugway Proving Ground. Dust clouds were
generated using static TNT charges to simulate the detonation of high
explosive munitions rounds. Table 1 shows trial number, the munition
simulated and the amount of TNT used. Photographic data were taken of
the dust clouds produced. Data were collected from various electro-
optical instruments operating at several wavelengths. At Fort Sill in
May 1978 tests involving live firings were conducted. Table 2 shows the
trials and the number of rounds fired (both single and multiple round
tests were conducted). Again both photographic and electro-optical data
were taken of the resulting dust clouds. In October 1978 a series of
tests of both static and live rounds were conducted at White Sands
Missile Range.

8

Table 1. List of explosives and simulated rounds
for Dugway tests.

Trial Number	Simulated Round	Weight of TNT (lbs)
DPG-002-D1	81 mm motar	3.5
DPG-002-D2	4.2 inch mortar	5.0
DPG-002-D4	120 mm mortar	8.0
DPG-002-D3	105 mm tank HEP	6.75
DPG-002-D5	155 mm artillery projectile	15.0
DPG-002-D6	8 inch artillery projectile	35.0

Table 2. List of Fort Sill test parameters.

Trial Designation	Weapon System	Number of Rounds Fired
T3	155 mm, M107	1
T4-T8	155 mm, M107	3
T9-T11	155 mm, M107	2
T12-T20	105 mm, M1	1
T21	105 mm, M1	4
T22	105 mm, M1	5

Unfortunately at this time only a limited amount of reduced data
are available from the test series for use in the dust cloud modeling
effort. For the Dugway tests, a preliminary copy of the test report
was made available to us. The report gives the data taken with the
electro-optical sensors. In addition the dust cloud length, width,
and vertical extent at 10 second intervals (out to about 60-90 seconds)
were separately provided. For the Fort Sill tests, some preliminary
data and the cloud dimensions (out to about 15 seconds) were provided.
No data were available from the just completed White Sands Missile
Range tests.

Figure 1 is a simplified flow chart of the elements required to construct a model for the effects of dust clouds in a tactical battlefield environment. The primary purpose of this report is to develop the models for the dust cloud itself (those items in the CLOUD MODEL box of Figure 1). We will develop models for the munition dust cloud size, location and distribution of mass within the cloud as a function of time. For the cloud model development, it was necessary to also develop the MIE MODEL parameters and parts of the PARTICLE MODEL, RADIATION TRANSPORT and OUTPUTS parameters. The basic modeling philosophy is to use first principle physics or similarity theory to set the form of the equation for a given effect, then use the experimental data, if they exist, to set the magnitudes of any adjustable parameters in the equation. We first give an overview of the whole dust cloud model. We then develop the details of the model in the following sections. The MIE MODEL details are given in the appendix.

Figure 2 is a sketch of the dust cloud formation and development. We ignore the extremely fast formation processes and assume an initial cloud is formed instantaneously at burst time. We assume that the dust mass lofted by the munition explosion consists of dust particles ranging in size from 0 to 1 cm in diameter. The upper limit of particle sizes is somewhat arbitrary but is of little significance since the larger particles fall out so rapidly.

We divide the particle size range into a number of individual size groups. Table 3 shows a preliminary choice of size groups. We want a large enough number of size groups to provide a continuous cloud description, but a small enough number for rapid computer calculations. All size groups are assumed to occupy the same volume of the initial cloud at time zero. We model the rise, expansion, wind transport and diffusion of each size group separately. The lightest particles will rise, expand, transport and diffuse at the fastest rates, while the heavier particles lag behind and fall out. Figure 3 shows a sketch of the size groups in the dust cloud.

Figure 1. Flowchart of tactical dust model.

```
                         ┌─────────────────────────────┐
                         │           INPUTS            │
                         │  BATTLEFIELD GEOMETRY       │
                         │  SHELL TYPE                 │
                         │  SURFACE SOIL               │
                         │  VEGETATION                 │
                         │  WINDS                      │
                         │  RADIATION WAVELENGTH       │
                         │  TRANSMIT - RECEIVE         │
                         │      SPECIFICATIONS         │
                         └─────────────────────────────┘
              ┌────────────────────┴────────────────────┐
┌───────────────────────────────┐     ┌───────────────────────────────┐
│         CLOUD MODEL           │     │        PARTICLE MODEL         │
│  SIZE - SHAPE (E)             │     │  SIZE DISTRIBUTION (E)        │
│  DUST LOADING (E)             │     │     DUST                      │
│  SMOKE CONTENT (E)            │     │     SMOKE                     │
│  WIND TRANSPORT (E-A)         │     │  BULK DENSITY (E)             │
│  TURBULENCE-DIFFUSION (E-A)   │     │  INDEX OF REFRACTION (E-A)    │
└───────────────────────────────┘     └───────────────────────────────┘
                 │                                    │
                 │                     ┌───────────────────────────────┐
                 │                     │          MIE MODEL            │
                 │                     │  SCATTER CROSS SECTION (A)    │
                 │                     │  ABSORPTION CROSS SECTION (A) │
                 │                     │  ANGULAR SCATTERING PATTERN (A)│
                 │                     └───────────────────────────────┘
                 └──────────────┐      ┌───────────┘
              ┌───────────────────────────────────────────────┐
              │         RADIATION TRANSPORT MODEL             │
              │  GEOMETRY (A)                                │
              │  RAY PATH INTEGRATION (A)                    │
              │  SINGLE AND MULTIPLE SCATTER EFFECTS (A)     │
              │  INTEGRATION OVER ANTENNA PATTERNS (A)       │
              └───────────────────────────────────────────────┘
                              │
                    ┌────────────────────┐
                    │       OUTPUTS      │
                    │  ATTENUATION       │
                    │  BACKSCATTER       │
                    │  NOISE-CLUTTER     │
                    │  SCINTILLATIONS    │
                    │  SIGNAL/NOISE      │
                    └────────────────────┘
```

E - EMPIRICAL MODEL
A - ANALYTIC MODEL

Figure 2. Munition dust cloud development.

CLOUD MODEL

INITIAL PHASE

SHOCK AND BLAST
EXTREMELY SHORT TIME DURATION

RISE PHASE

INITIAL UPWARD VELOCITIES
PLUS BUOYANT RISE
SHORT TO INTERMEDIATE TIME
DURATION

WIND

DISPERSION PHASE

TRANSPORT BY WIND
TURBULENT EDDY DIFFUSION
DUST PARTICLE FALLOUT
LONG TIME DURATION

12
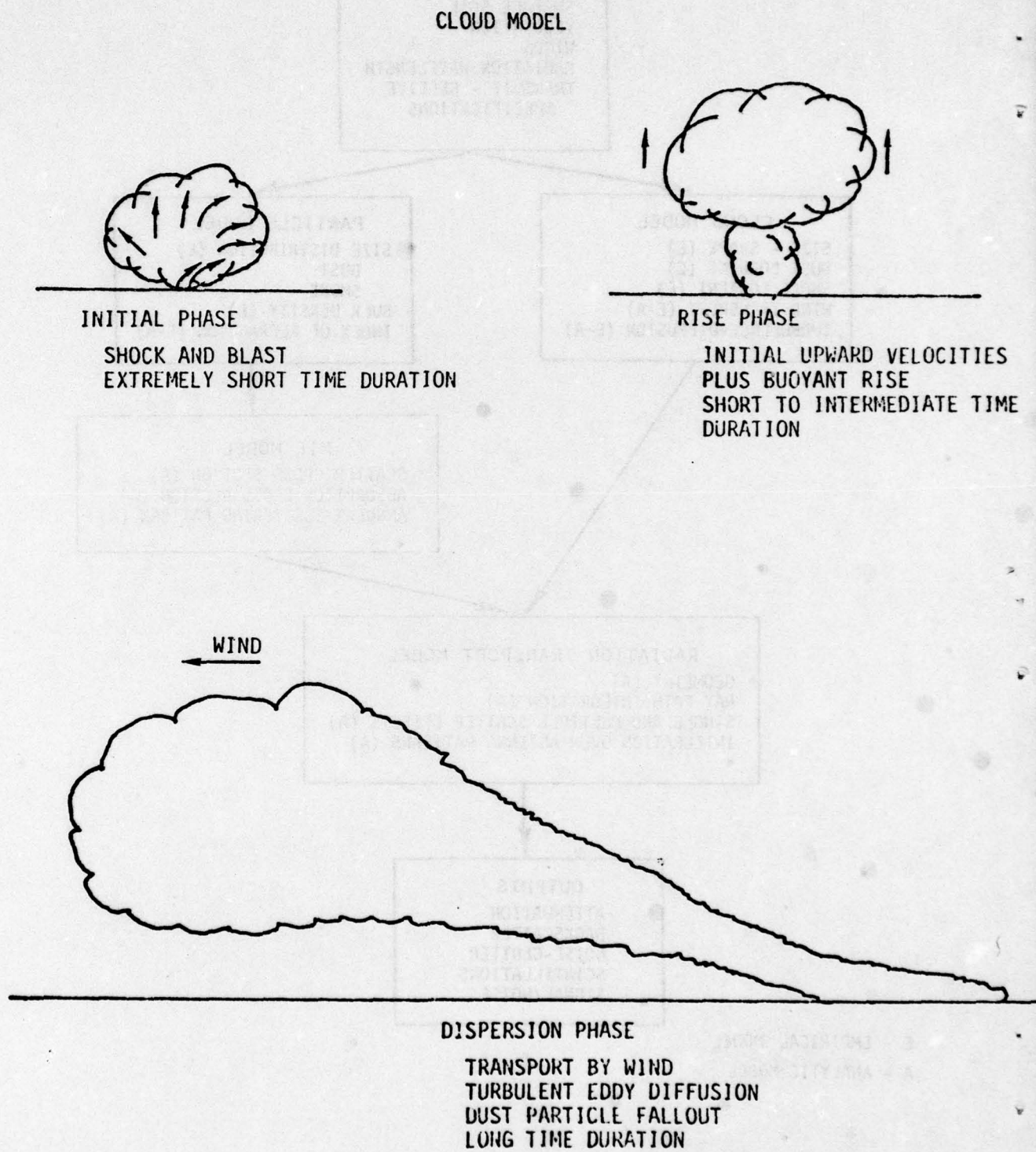
Table 3. Particle size groups.

Group	Range of Particle Diameters (cm)
1	0 - 0.001
2	0.001 - 0.002
3	0.002 - 0.004
4	0.004 - 0.006
5	0.006 - 0.008
6	0.008 - 0.01
7	0.01 - 0.02
8	0.02 - 0.03
9	0.03 - 0.04
10	0.04 - 0.05
11	0.05 - 0.06
12	0.06 - 0.07
13	0.07 - 0.08
14	0.08 - 0.09
15	0.09 - 0.1
16	0.1 - 0.2
17	0.2 - 0.4
18	0.4 - 0.6
19	0.6 - 0.8
20	0.8 - 1.0

Consider an x, y, z rectangular coordinate system with origin at ground level at the explosion point. z is in the vertical direction; x is along the wind direction; and y is in the cross wind direction.

We take the geometry of each size group to be spheroidal with cloud radii R_x, R_y and R_z (see Figure 4). The radii are measured from the centroid of each size group, (x_c, y_c, z_c). We will model the centroid positions and radii as a function of time.

Each size group has a relatively small range of particle sizes in it. We assume no size separation within a given group. That is, each element of mass anywhere in the volume of a given size group has the same particle
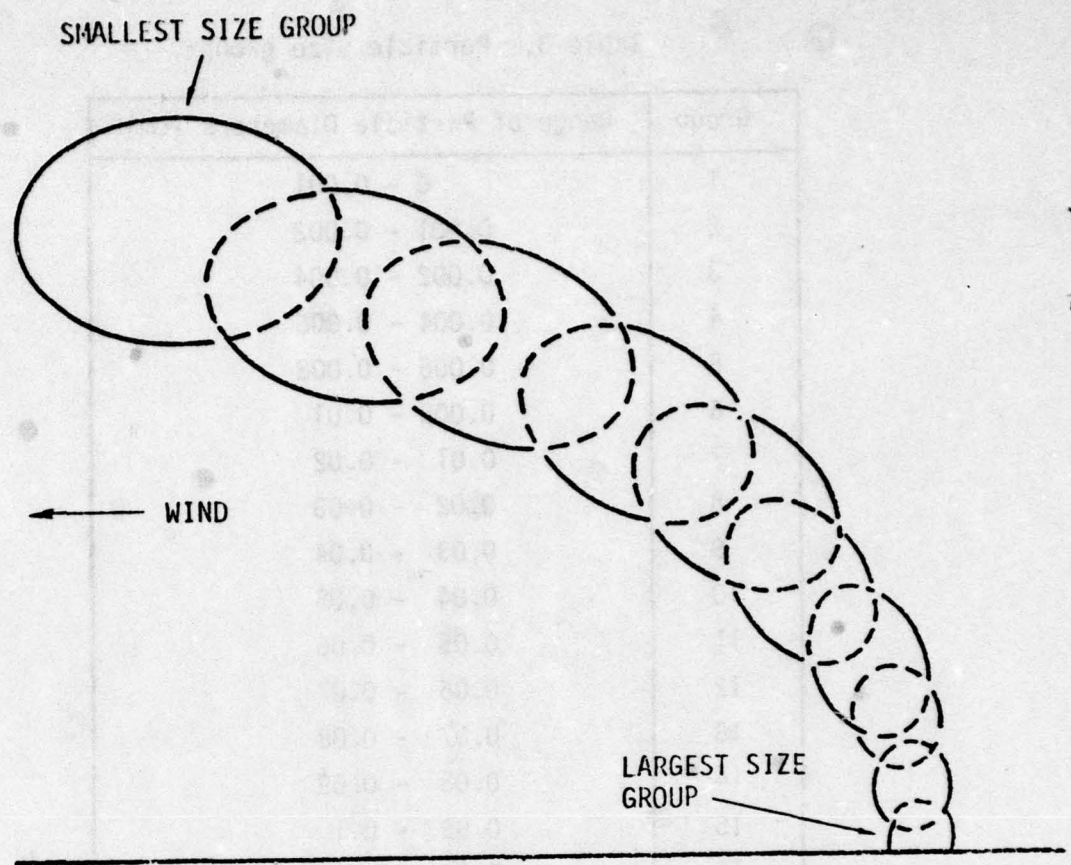
13

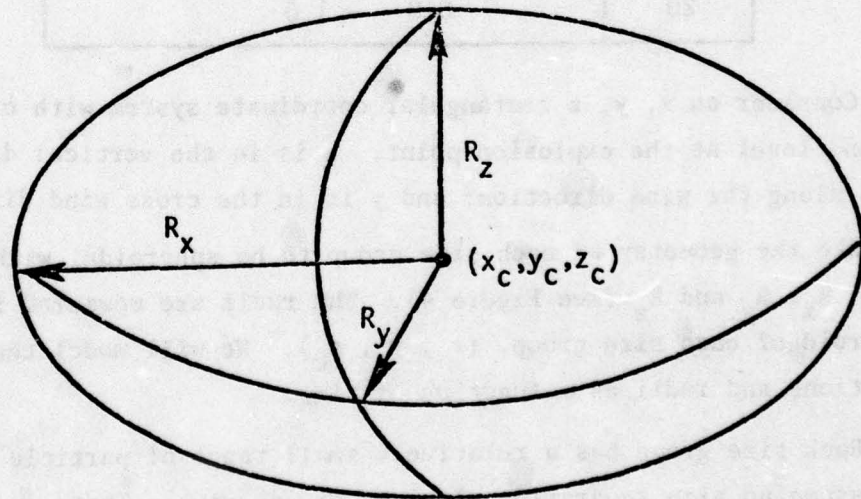Figure 3. Size groups in dust cloud.

Figure 4. Spheroidal geometry.

14

size distribution. This uniform size mixing assumption allows us to
calculate the scattering and absorption mass coefficients for each size
group only once. The scatter and attenuation of each size group is
then only a function of the mass penetrated. We assume that within each
size group spheroid, the mass distribution is Gaussian.

$$\rho(x,y,z) = \frac{M}{(2\pi)^{3/2}\sigma_x\sigma_y\sigma_z} \exp\left[-\frac{1}{2}\left\{ \left(\frac{x-x_c}{\sigma_x}\right)^2 + \left(\frac{y-y_c}{\sigma_y}\right)^2 + \left(\frac{z-z_c}{\sigma_z}\right)^2 \right\} \right] \quad (1)$$

where

ρ = dust mass density at point (x,y,z) within the size group
    volume $(g\ m^{-3})$

M = total mass in given size group (g)

σ_x^2 = variance of mass density in the x direction (m^2)

x_c = x-coordinate of centroid of size group volume (m)

M is a constant determined by the dust loading model. The variances
and the centroid coordinates are functions of time. We assume the
visible cloud radii and the mass variances are related by

$$R_i = C_r\sigma_i \quad\quad\quad\quad\quad\quad\quad\quad (2)$$

where

i = x, y or z

C_r = constant

The value of C_r depends upon the measurement technique. The visible
cloud dimensions are generally determined by photographic data. If we
assume the image brightness at any point is proportional to the mass
penetrated through the cloud at that point, then a common assumption is
the visible cloud edge occurs at a mass penetrated value which is a
constant fraction of that at the cloud center. A typical fraction value
is 0.1, in which case C_r is 2.15 (Reference 5). Other assumptions and
measurement techniques give different values for C_r, but C_r is almost
always in the range from 1 to 3. Until we have more data for the muni-
tion clouds, we take

$$C_r = 2.15 \quad\quad\quad\quad\quad\quad\quad\quad (3)$$

15

SECTION 2

INITIAL DUST CLOUD
RADIUS AND SHAPE

Consider a munitions round impacting the ground. Depending on the
fusing, the round can detonate at or under the ground surface. The ex-
plosive energy release will lead to crater formation and the lofting of
dust into the air. Part of the energy released will couple into the air
and appear as hydrodynamic, ie, as shock, energy. The formation of a
blast shock will lead to a very rapid expansion of the explosive cloud.
At first the pressure inside the cloud is much greater than the ambient
pressure. But as the cloud expands, the internal pressure drops. When
the cloud comes into approximate pressure equilibrium with the ambient
atmosphere, the rapid expansion ceases and the initially high internal
air flow velocities rapidly decrease.

The initial size of the dust cloud is not a precisely defined quantity.
The early rapid expansion slows and continuously merges into the slow
expansion of the rise and diffusion phase. The time scale of the air
shock motion is extremely short; pressure equilibrium is reached in a
few milliseconds or less. However, it may take several tenths of sec-
onds for the initial high dust particle velocities to slow. We take the
initial cloud size as the size at the end of the rapid expansion phase
and the beginning of the slow expansion phase. We ignore the details of
the rapid expansion phase and assume the initial dust cloud is formed
instantaneously at burst time.

We will rely upon the theory of shock physics for the functional form
of the initial dust cloud radius. We then use the experimental data to
set the value of any adjustable parameters. The motion of a spherical
shock in uniform air with a constant gas gamma can be expressed in similarity
equations. The normalizing distance and time constants are

16

$$R_o = \left(\frac{E_H}{P}\right)^{1/3} \text{ cm} \tag{4}$$

$$t_o = \left(\frac{\rho}{P}\right)^{1/2} R_o \text{ s} \tag{5}$$

where

E_H = hydrodynamic yield of the explosion producing the shock (ergs)

P = ambient pressure (dynes cm^{-2})

ρ = ambient density (g cm^{-3}).

Then in terms of R/R_o, t/t_o all shocks are similar. Figure 5 from Reference 1 gives the properties at the shock front.

We assume that the initial radius of the cloud is the shock radius at pressure equilibrium time. From hydro code calculations and observations of nuclear fireballs, the pressure equilibrium time is approximately

$$\frac{t_{PE}}{t_o} \approx 0.162 \tag{6}$$

at which time

$$\frac{R}{R_o} \approx 0.562 \tag{7}$$

If we assume 1 Lb TNT = 5×10^5 cal = 2.09×10^{13} ergs, and

$$\frac{\rho}{\rho_o} = \frac{P}{P_o} \quad \text{(by custom in weapon effects scaling, } \rho/\rho_o \text{ is used instead of } P/P_o\text{)}$$

Then the initial explosive cloud radius can be written

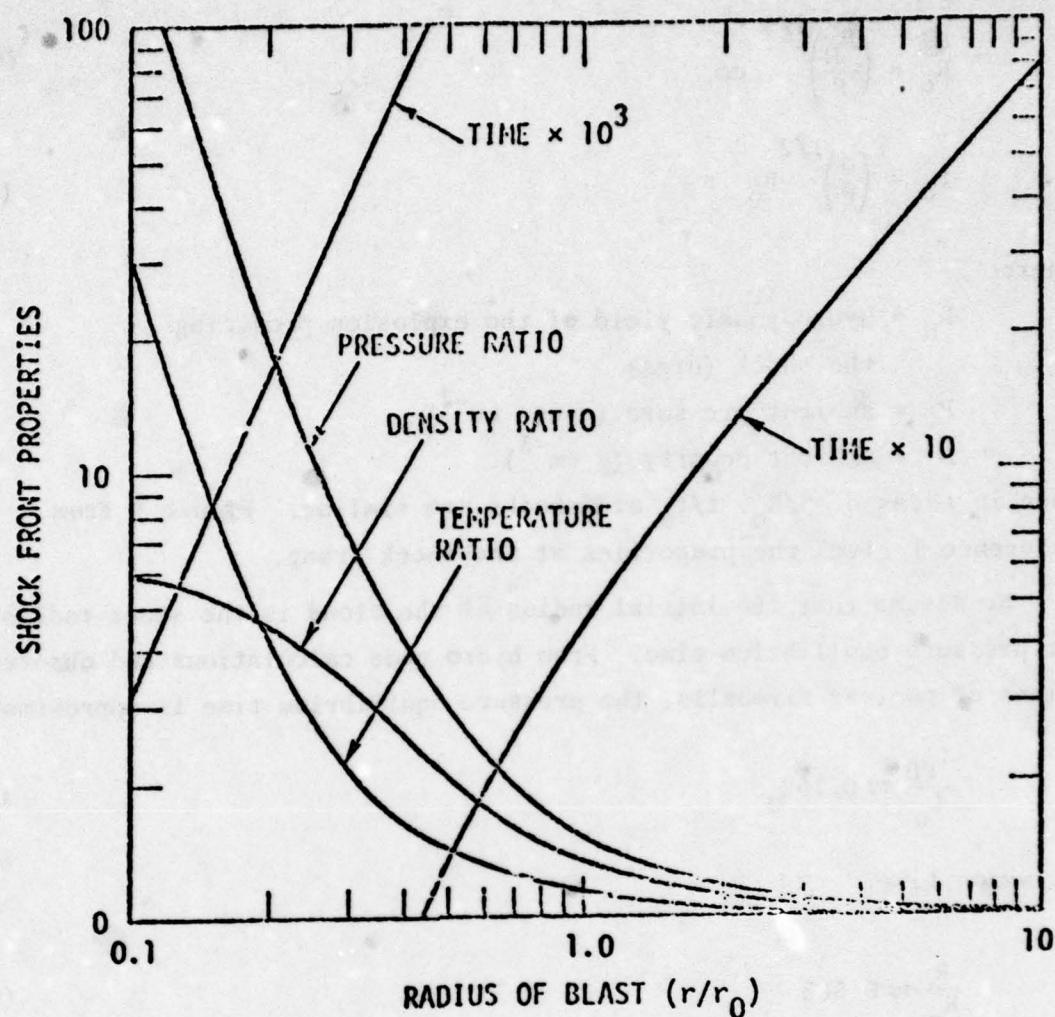$$R_I = 1.54 \left(f W \frac{\rho_o}{\rho}\right)^{1/3} \text{ m} \tag{8}$$

17

Figure 5. Shock front properties.

where

R_I = initial cloud radius (m)

W = munition yield (Lb TNT)

ρ = air density at blast site (g cm^{-3})

ρ_o = sea level air density (g cm^{-3})

f = a fraction which depends on the explosive type.

16

For a free air explosion, f would be the fraction of the total yield which appears as effective hydrodynamic energy. For a munition explosion in free air,

$f \approx 1$

For a conventional nuclear device detonated in free air,

$f = 0.633$

The remaining fraction of the nuclear yield is radiated away from the nuclear fireball as thermal emissions (an effect not present in the munitions explosion).

For our case of surface or below surface munitions detonations, f can be considered an empirical factor, to be set primarily from the experimental data. f will depend on shell type, explosion depth, and soil type. Table 4 from Reference 2 gives the currently available dust cloud size data from the Dugway dust tests. The data are given at 10-second intervals, with initial dimensions given at z-time (which we assume to be a time very shortly after detonation). The initial Dugway clouds are roughly spherical. We take as the experimental initial radius one half (the test data are diameters) of the average of the X, Y, and Z initial dimensions. Figure 6 shows the initial radius versus yield and the fit to the data. The Dugway explosives were static TNT charges buried so that the top of the charge was at the ground surface. For these type of charges and for the Dugway soil type,

$f = 0.84$ (9)

Tables 5 through 13 from Reference 3 give the currently available data for single round tests from the Fort Sill test series. Trial T-3 is a 155-mm round; the other eight tests are for the 105-mm round. The size data are given at 0.1 second intervals for the first second, then at 1 second intervals thereafter. There is considerable scatter in the size data from one test to the next. But in general the early cloud

19

Table 4. Dugway dust cloud measurements.

All data in meters; X = length, Y = width, Z = height

	X	Y	Z	X	Y	Z	X	Y	Z	X	Y	Z
		D1			D2			D3			D4	
Z Time	3	5	3	5	8	3	6	6	6	4	4	6
Z + 10 sec.	24	-22	3	40	22	15	20	19	7	39	20	14
Z + 20 "	58	-28	3	64	23	25	87	38	11	67	34	18
Z + 30 "	50	23	13	66	25	34	99	46	21	88	38	27
Z + 40 "	51	20	13	57	40	30	143	50	24	84	53	25
Z + 50 "	47	19	13	65	39	31	Cloud			78	58	23
Z + 60 "	46	18	13	41	48	30	moved			100	64	28
Z + 70 "	No visible			No visible			outside			Cloud		
Z + 80 "	cloud			cloud			camera			moved		
Z + 90 "							coverage			outside		
Z + 100 "										camera		
Z + 110 "										coverage		
Z + 120 "												

	X	Y	Z	X	Y	Z
		D5			D6	
Z Time	10	N*	9	12	N*	11
Z + 10 sec.	42	0	12	56	0	26
Z + 20 "	50		12	71	D	38
Z + 30 "	47	D	19	69	A	53
Z + 40 "	58	A	10	66	T	49
Z + 50 "	60	T	17	84	A	47
Z + 60 "	51	A	18	Cloud moved		
Z + 70 "	53		12	outside camera		
Z + 80 "	55		16	coverage		
Z + 90 "	59		15			

*Dust from high winds obscured view of camera. Width measurements cannot be provided.
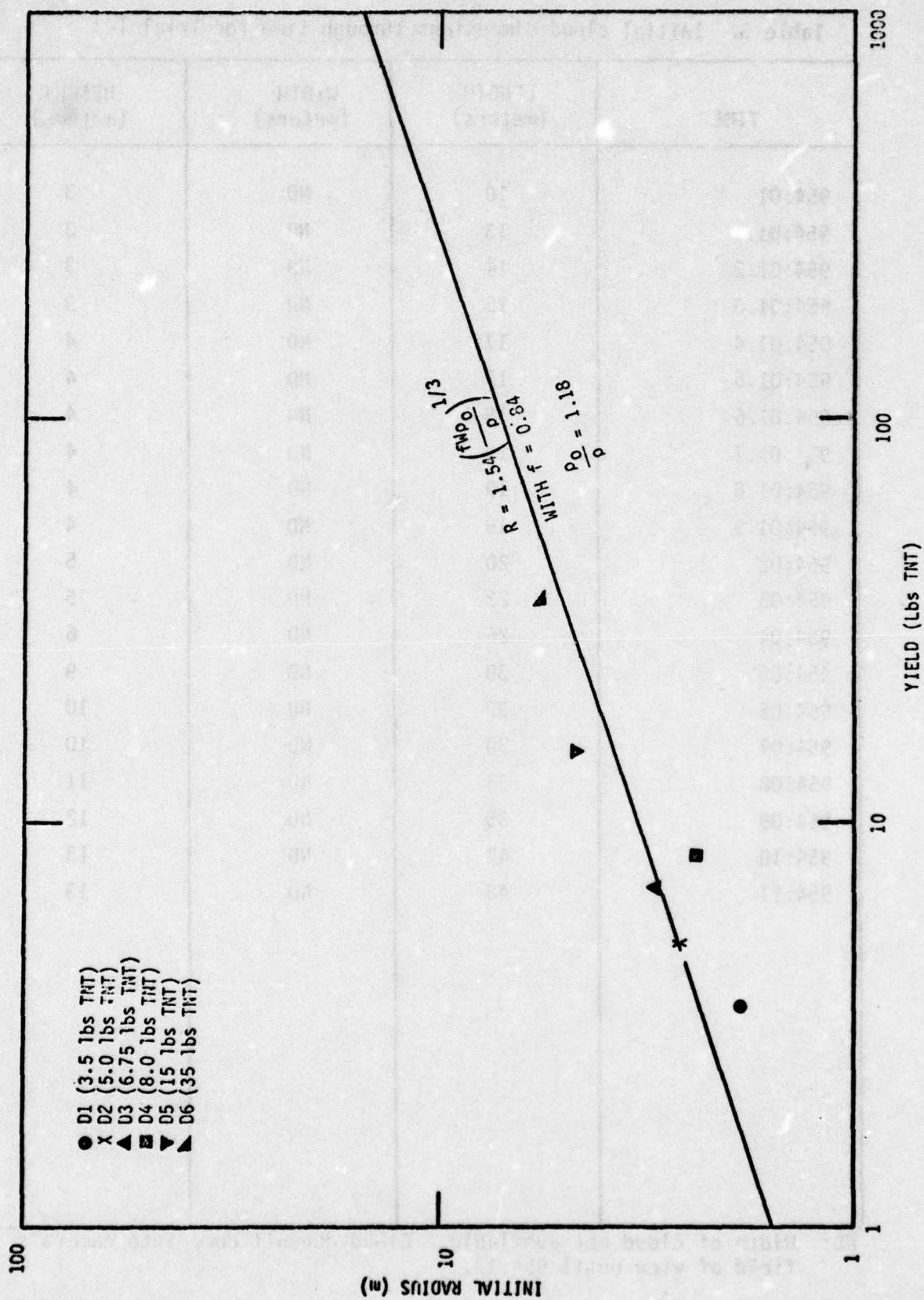
Figure 6. Initial cloud radius (DUGWAY).

$$R = 1.54 \left(\frac{FW\rho_0}{\rho} \right)^{1/3}$$

WITH f = 0.34

$$\frac{\rho_0}{\rho} = 1.18$$

YIELD (Lbs TNT)

INITIAL RADIUS (m)

● D1 (3.5 lbs TNT)
✕ D2 (5.0 lbs TNT)
◀ D3 (6.75 lbs TNT)
■ D4 (8.0 lbs TNT)
▶ D5 (15 lbs TNT)
◣ D6 (35 lbs TNT)

Table 5. Initial cloud dimensions through time for Trial T-3.

TIME	LENGTH (meters)	WIDTH (meters)	HEIGHT (meters)
954:01	10	ND	3
954:01.1	13	ND	3
954:01.2	14	ND	3
954:01.3	15	ND	3
954:01.4	17	ND	4
954:01.5	17	ND	4
954:01.6	18	ND	4
954:01.7	19	ND	4
954:01.8	19	ND	4
954:01.9	19	ND	4
954:02	20	ND	5
954:03	22	ND	5
954:04	26	ND	6
954:05	30	ND	9
954:06	30	ND	10
954:07	30	ND	10
954:08	33	ND	11
954:09	35	ND	12
954:10	43	ND	13
954:11	48	ND	13

ND: Width of cloud not available. Cloud doesn't come into camera's field of view until 954:13.

Table 6. Initial cloud dimensions through time for Trial T-12.

TIME	LENGTH (meters)	WIDTH (meters)	HEIGHT (meters)
921:00	4	4	2
921:00.1	4	9	3
921:00.2	7	9	3
921:00.3	7	11	3
921:00.4	8	11	3
921:00.5	8	11	4
921:00.6	8	11	4
921:00.7	9	12	4
921:00.8	10	12	5
921:00.9	10	12	6
921:01	11	12	6
921:02	15	16	7
921:03	17	18	8
921:04	17	22	9
921:05	18	23	9
921:06	18	25	9
921:07	19	25	10
921:08	21	33	12
921:09	21	36	12
921:10	23	37	12
921:11	26	39	11
921:12	36	ND	11
921:13	42	ND	11
921:14	42	ND	10
921:15	42	ND	10

ND: Width of cloud not available. Camera stopped at 921:11.

Table 7. Initial cloud dimensions through time for Trial T-13.

TIME	LENGTH (meters)	WIDTH (meters)	HEIGHT (meters)
927:02	1	2	1
927:02.1	3	10	2
927:02.2	5	12	2
927:02.3	7	13	3
927:02.4	7	14	3
927:02.5	8	14	3
927:02.6	8	15	3
927:02.7	8	15	4
927:02.8	8	15	4
927:02.9	9	17	4
927:03	9	17	4
927:04	11	22	6
927:05	13	29	7
927:06	15	32	8
927:07	19	32	9
927:08	21	35	9
927:09	26	39	10

24

Table 8. Initial cloud dimensions through time for Trial T-14.

TIME	LENGTH (meters)	WIDTH (meters)	HEIGHT (meters)
934:00	2	6	1
934:00.1	3	10	2
934:00.2	4	11	2
934:00.3	7	12	2
934:00.4	7	12	3
934:00.5	8	13	3
934:00.6	10	14	3
934:00.7	10	15	3
934:00.8	10	15	3
934:00.9	10	15	3
934:01	10	16	3
934:02	13	19	5
934:03	15	24	5
934:04	15	28	7
934:05	16	32	7
934:06	17	35	7

Table 9. Initial cloud dimensions through time for Trial T-15.

TIME	LENGTH (meters)	WIDTH (meters)	HEIGHT (meters)
957:59	ND	2	2
957:59.1	ND	4	3
957:59.2	ND	4	3
957:59.3	ND	4	4
957:59.4	ND	5	5
957:59.5	ND	5	5
957:59.6	ND	5	5
957:59.7	ND	5	5
957:59.8	ND	5	5
957:59.9	ND	5	5
958:00	ND	6	5
958:01	ND	8	6
958:02	ND	10	7
958:03	ND	11	7
958:04	ND	13	9
958:05	ND	16	10
958:06	ND	16	10
958:07	ND	18	10
958:08	ND	19	11
958:09	ND	20	12
958:10	ND	20	13
958:11	ND	20	13
958:12	ND	21	14
958:13	ND	23	15
958:14	ND	23	15

ND: Length of cloud not available. Camera did not run.

Table 10. Initial cloud dimensions through time for Trial T-16.

TIME	LENGTH (meters)	WIDTH (meters)	HEIGHT (meters)
1004:01	ND	2	3
1004:01.1	ND	3	3
1004:01.2	ND	3	3
1004:01.3	ND	5	3
1004:01.4	ND	5	3
1004:01.5	ND	6	3
1004:01.6	ND	7	3
1004:01.7	ND	7	3
1004:01.8	ND	7	3
1004:01.9	ND	7	3
1004:02	ND	7	4
1004:03	ND	8	5
1004:04	ND	10	6
1004:05	ND	13	7
1004:06	ND	18	7
1004:07	ND	19	7
1004:08	ND	23	7
1004:09	ND	23	7
1004:10	ND	23	7
1004:11	ND	23	7
1004:12	ND	28	8
1004:13	ND	28	9
1004:14	ND	28	10
1004:15	ND	29	10
1004:16	ND	31	11
1004:17	ND	31	11
1004:18	ND	31	13

ND: Length of cloud not available. Camera did not run.

Table 11. Initial cloud dimensions through time for Trial T-17.

TIME	LENGTH (meters)	WIDTH (meters)	HEIGHT (meters)
1010:01	ND	3	4
1010:01.1	ND	4	4
1010:01.2	ND	5	4
1010:01.3	ND	6	4
1010:01.4	ND	6	4
1010:01.5	ND	7	4
1010:01.6	ND	7	4
1010:01.7	ND	8	4
1010:01.8	ND	8	4
1010:01.9	ND	8	4
1010:02	ND	8	4
1010:03	ND	11	6
1010:04	ND	12	7
1010:05	ND	12	8
1010:06	ND	13	9
1010:07	ND	15	10
1010:08	ND	17	11
1010:09	ND	19	11
1010:10	ND	19	12
1010:11	ND	23	13
1010:12	ND	23	13
1010:13	ND	24	14
1010:14	ND	26	15
1010:15	ND	26	15
1010:16	ND	26	16
1010:17	ND	28	18

ND: Length of cloud not available. Camera did not run.

Table 12.   Initial cloud dimensions through time for Trial T-19.

TIME	LENGTH (meters)	WIDTH (meters)	HEIGHT (meters)
1141:00	ND	5	1
1141:00.1	ND	7	2
1141:00.2	ND	8	2
1141:00.3	ND	8	2
1141:00.4	ND	9	2
1141:00.5	ND	9	3
1141:00.6	ND	10	3
1141:00.7	ND	10	3
1141:00.8	ND	10	3
1141:00.9	ND	10	3
1141:01	ND	10	3
1141:02	ND	13	3
1141:03	ND	15	3
1141:04	ND	15	5
1141:05	ND	16	6
1141:06	ND	18	6
1141:07	ND	19	7
1141:08	ND	19	7
1141:09	ND	23	8
1141:10	ND	23	8

ND: Length of cloud not available.   Camera did not run

Table 13. Initial cloud dimensions through time for Trial T-20.

TIME	LENGTH (meters)	WIDTH (meters)	HEIGHT (meters)
1148:00	ND	6	2
1148:00.1	ND	6	2
1148:00.2	ND	6	2
1148:00.3	ND	8	2
1148:00.4	ND	10	2
1148:00.5	ND	11	2
1148:00.6	ND	11	2
1148:00.7	ND	12	3
1148:00.8	ND	12	3
1148:00.9	ND	12	3
1148:01	ND	15	3
1148:02	ND	15	3
1148:03	ND	15	5
1148:04	ND	16	5
1148:05	ND	18	6
1148:06	ND	19	8

ND: Length of cloud not available. Camera did not run.

30

(time less than about 0.3 seconds) is not spherical; the vertical dimension is about half of the horizontal dimension. In contrast to the static charges of the Dugway tests, the Fort Sill tests are firings of live rounds. The rounds impact the ground at an angle with considerable velocity, penetrate the ground to the fusing depth, and explode. In a dynamic detonation of this sort, it is not surprising that the resulting dust cloud is nonspherical. The forward momentum of the shell may lead to an initial cloud that is elongated along the shell track with a suppressed vertical dimension. At present the data are too sketchy to draw any firm conclusions. We will assume that the initial cloud radius in the horizontal direction perpendicular to the shell track is given by the pressure equilibrium radius, Equation 8. The initial dimensions in the horizontal along track direction and the vertical direction will be taken as constants times the cross track dimension.

The preliminary Fort Sill data give length, width, and height measurements for the dust cloud, but unfortunately give neither the shell track direction nor the wind direction. At early times we expect the cloud to be elongated along the shell track direction and at later times elongated along the wind direction. We use the width dimensions of Tables 9 through 13 for both the initial cross track cloud size and the later cross wind dimension. The cross track dimension expands fairly rapidly for the first 0.2 to 0.3 seconds, then expands at a considerably slower rate thereafter. We take as the initial size of the dust cloud the width radius at about 0.3 seconds, corrected for the amount of expansion due simply to cloud rise in this time. For a munition explosion, we expect f to have its largest value, f = 1, for a free air burst and then decrease as the depth of burial of the burst increases. To determine f for the Fort Sill munitions, we utilize both the initial size data and the later time expansion data (detailed in the next section). A reasonable fit to both early and late data gives for the 105- and 155-mm rounds and the Fort Sill soil type

$$f = 0.5 \tag{10}$$

31

We assume the initial shape of any dust cloud is spheroidal, with initial radii

R_T = initial horizontal radius along the shell track (m)

R_P = initial horizontal radius perpendicular to the shell track (m)

R_V = initial vertical radius (m).

We take

$$R_T = C_T R_I \qquad (11a)$$
$$R_P = C_P R_I \qquad (11b)$$
$$R_V = C_V R_I \qquad (11c)$$

where R_I is the initial radius given by Equation 8, and C_T, C_P, and C_V are shape constants. The shape constants depend upon munition and soil type. For the static charges and the soil type at Dugway Proving Grounds

$$C_T = C_P = C_V = 1 \qquad (12)$$

For the 105- and 155-mm rounds and the soil types at Fort Sill

$$C_T \approx 2 \qquad (13a)$$
$$C_P = 1 \qquad (13b)$$
$$C_V = \frac{1}{2} \qquad (13c)$$

We have reasonable confidence in the C_P and C_V values for the Fort Sill shape factors; see the early time fits of Figures 10 and 11 The C_T value is less certain. The chosen value of 2 is not incompatible with the width to length ratios of Tables 6 to 8 for the first several tenths of seconds. Moreover the value 2 conserves the total volume; that is, the spheroid volume is the same as the volume of a sphere with the shape factors equal to unity. As yet we do not have sufficient data to take the conservation of volume as a general rule.

32

As more data become available for different munitions and soils, general rules can be formulated for the functional dependencies of f and the shape factors. The initial cloud size and shape are significant only for the first several seconds. The rapid expansion rates in the wind, cross wind, and vertical directions quickly dominate any initial effects. The expansion rates determine the cloud size and shape and any initial influence is quickly lost.

33

SECTION 3
DUST CLOUD RISE PHASE

The initial explosively formed cloud will have an average internal temperature higher than the ambient temperature. Consequently, the cloud will rise buoyantly. The early cloud is highly turbulent. The differential velocity between the rising cloud and the ambient air is a continuing source of cloud turbulence during the rise phase. The initial and continuing turbulence during rise will cause the cooler ambient air to be entrained and mixed with the warmer cloud air. The cloud will continue rising until the cooling due to mass entrainment and adiabatic expansion bring the cloud into temperature equilibrium with the atmosphere. In this section we will model the cloud size, shape, and altitude time history during the rise phase.

For experimental data we have the cloud dimensions given in Tables 4 through 13 from the Dugway and Fort Sill test series. Unfortunately at this early stage in the test data reduction, there are no cloud altitude data available. We will proceed in the modeling of the dust cloud rise phase as follows. We will use shock physics to determine the temperature of the initial cloud. We then use a theoretical buoyant bubble rise with entrainment model to calculate the cloud size and altitude time history. We then set any adjustable parameters to give a good match to the experimental size data.

The shock code of Reference 1 was used to calculate the temperature, density, and pressure profiles inside a spherical shock in free air as a function of time. At pressure equilibrium time, the shock front is at the pressure equilibrium radius of Equation 8 . The average temperature as defined by

$$\overline{T} = \frac{\int_0^{R_I} \rho T r^2 \, dr}{\int_0^{R_I} \rho r^2 \, dr} \quad °K \tag{14}$$

is

$$\overline{T} = 1.4 \, T_o \quad °K \tag{15}$$

where T_o is the ambient temperature. As time increases, the shock front moves farther out; the density inside the R_I radius decreases to an average value

$$\overline{\rho} = \frac{T_o}{\overline{T}} \rho_o = \frac{\rho_o}{1.4} \quad ,$$

but the average temperature remains very close to $1.4 \, T_o$. Hence we take the temperature of the initial dust cloud to be $1.4 \, T_o$; this corresponds to $403°K$ for a typical ambient temperature of $288°K$.

We will use the GE—TEMPO buoyant fireball rise computer model to calculate the rise and expansion of the dust cloud. Details of the rise model are given in Reference 4; for reader convenience we give a very brief synopsis. The basic rise model assumptions are:

- The cloud is in pressure equilibrium with the ambient atmosphere at all times during the rise history.
- The cloud is isothermal at all times.
- As the cloud rises, it entrains a constant fraction, α, of the ambient air encountered. The entrained air is instantly mixed with the cloud air.
- The drag force on the rising cloud can be described by a constant drag parameter, C_D.
- The shape of the rising cloud does not change; the cloud merely gets larger.

With these assumptions the equations for the cloud temperature rise velocity, and total mass are

35

$$\frac{dT}{dt} = T\left\{\left[\frac{\gamma-1}{\gamma}\right]\frac{1}{P}\frac{dP}{dt} + \left[\frac{\gamma-1}{\gamma_a-1}\frac{\gamma_a}{\gamma}\frac{Z_a}{Z}\frac{T_a}{T} - 1\right]\frac{1}{M}\frac{dM}{dt} + \frac{1}{\gamma(\gamma-1)}\frac{d(\gamma-1)}{dt}\right.$$

$$\left. - \frac{1}{Z}\frac{dZ}{dt}\right\} \, ^\circ K \, s^{-1} \tag{16}$$

$$\frac{dv}{dt} = \left[\frac{\rho_a}{\rho} - 1\right]g - \frac{C_{D/2} + \alpha}{M}\rho_a v^2 A_\perp \quad cm \, s^{-2} \tag{17}$$

$$\frac{dM}{dt} = \alpha\rho_a v A_\perp \quad gm \, s^{-1} \tag{18}$$

where

T = temperature of cloud ($^\circ$K)

P = pressure of cloud (dynes cm^{-2})

v = cloud rise velocity ($cm \, s^{-1}$)

$A_\perp$ = cross sectional area (perpendicular to v) (cm^2)

M = mass of air in cloud (gm)

Z = number of moles of hot air of temperature T and pressure
P per mole of cold air

γ = effective gas constant at temperature T and pressure P

α = constant entrainment parameter

C_D = constant drag parameter

g = acceleration of gravity ($cm \, s^{-2}$)

T_a, P_a, Z_a, γ_a are the corresponding quantities for the
ambient air.

In Equation 16 the first term on the right-hand side is the
adiabatic expansion term, the second term is the mass entrainment term,
and the third and fourth terms are the changing equation of state of
air terms. The third and fourth terms are significant for the high
temperatures of a nuclear fireball cloud, but are insignificant for the

36

lower temperatures of a munitions cloud. The shape of the cloud is specified by the user—whether spherical, spheroidal, toroidal, or other. Given the initial cloud size and temperature, the rise program numerically integrates the rise equations forward in time and prints out the cloud altitude, size, and temperature.

The important parameters controlling the rise of a buoyant cloud are the hydrodynamic yield, fW, which determines the initial size and temperature of the cloud, and the mass entrainment factor, α. The drag coefficient, C_D, has no effect upon the cloud size and temperature versus altitude, but merely affects the time at which the cloud reaches that altitude. The present rise and expansion experimental data base is incomplete; so the cloud shape, entrainment factor, and drag coefficient cannot be determined with a high confidence level. We again employ the reasonable procedure of using the theoretical rise program to determine the functional form of the cloud rise and expansion; we then adjust the resulting equations to fit the existing experimental data (in this case, the expansion data since there are no rise data). We choose the simplest case for the rise program calculation, a spherical cloud. We take hydrodynamic yields (fW) of 1, 10, 100, and 1000 pounds of TNT, and a range of entrainment factors (α) of 0.5, 1, and 2. The drag coefficient (C_D) is set equal to 0.8 (a typical value for low-altitude nuclear clouds). The initial cloud radius is calculated from Equation 8 and the initial cloud temperature was set at 403°K (1.4 times the ambient temperature of 288°K). Figure 7 shows the altitude of the cloud center as a function of time for a neutral stability atmosphere (see Post Rise Phase section). Figure 8 shows the cloud radius versus time. In the two figures, the point at which the solid and the dotted lines join is the point at which the cloud temperature has fallen to about 5°K above the ambient temperature.

The idealized turbulent entrainment of ambient air by the rising spherical cloud results in a radial growth which is described by the classical diffusion equation
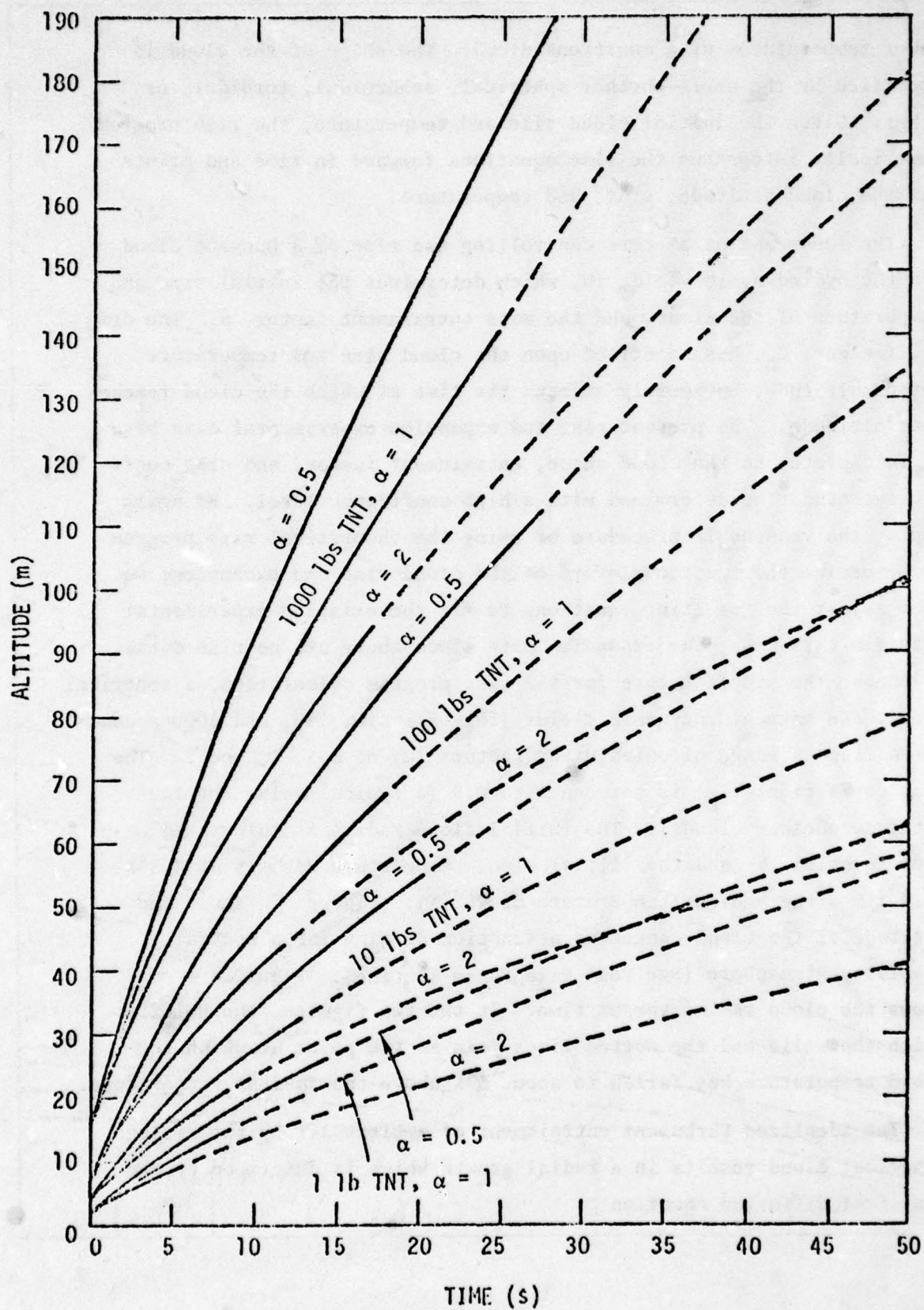
37

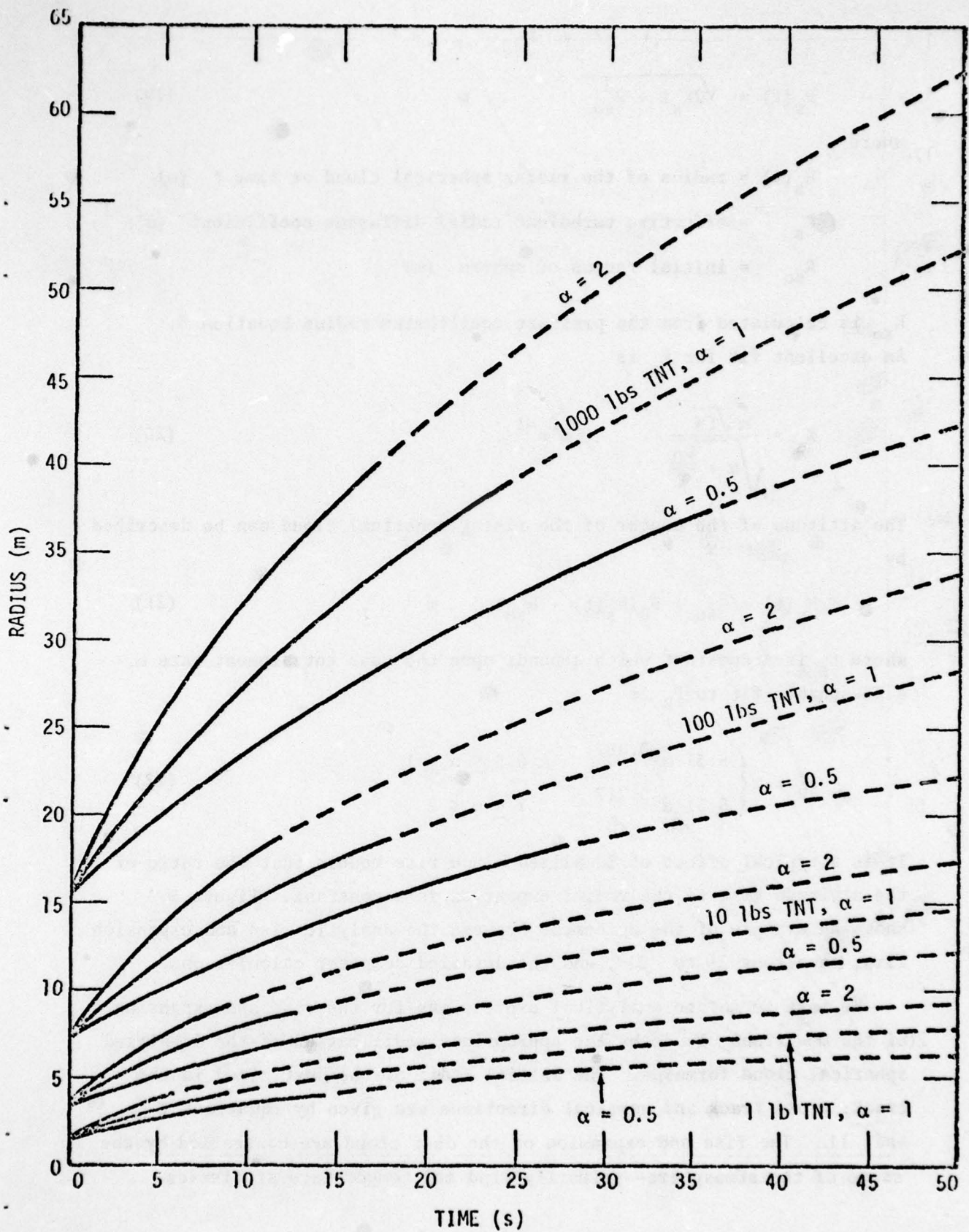Figure 7. Altitude of ideal spherical buoyant cloud.

38

Figure 8. Radius of ideal spherical buoyant cloud.

39

$$R_s(t) = \sqrt{2K_s t + R_{so}^2} \qquad \text{m} \qquad\qquad (19)$$

where

$R_s(t)$ = radius of the rising spherical cloud at time t   (m)

K_s = effective turbulent radial diffusion coefficient   ($m^2 s^{-1}$)

R_{so} = initial radius of sphere   (m)

R_{so} is calculated from the pressure equilibrium radius Equation 8.
An excellent fit for K_s is

$$K_s = \frac{\alpha \sqrt{fW}}{\sqrt{\alpha + \dfrac{C_D}{2}}} \qquad m^2 s^{-1} . \qquad\qquad (20)$$

The altitude of the center of the rising spherical cloud can be described
by

$$H_s(t) = R_{so} + F_R(R_s(t) - R_{so}) \qquad \text{m} \qquad\qquad (21)$$

where F_R is a constant which depends upon the mass entrainment rate α.
A reasonable fit to F_R is

$$F_R = \begin{cases} 5.31\ \alpha^{-0.857} & 0.5 \le \alpha \le 1 \\ 5.31\ \alpha^{-0.717} & 1 \le \alpha \le 2 \end{cases} . \qquad\qquad (22)$$

It is a typical effect of idealized cloud rise models that the ratio of
the altitude rise to the radial expansion is a constant. Figure 9
shows an example of the agreement between the analytic rise and expansion
fits, Equations 19 to 21 , and the detailed computer calculations.

   We next formulate analytical expressions for the rise and expansion
of the munitions clouds by the appropriate modification of the idealized
spherical cloud formulas. The initial radii of the dust cloud in the
track, cross track and vertical directions are given by Equations 8
and 11.   The rise and expansion of the dust cloud are controlled by the
state of the atmosphere—primarily wind and temperature statistics.

40

The Pasquill Stability Categories, Reference 5, are commonly used descriptors of the atmospheric state. Another parameter, often used in similarity equations, is the atmospheric turbulent dissipation rate, ε (ergs s^{-1} g^{-1}). The Pasquill parameters are easier to measure and are our preferred atmospheric descriptors. For our analytic formulas, our eventual goal is to correlate α, and possibly C_D, with the observed atmospheric state. In the related program of analyzing clouds from countermeasure smoke devices, the cloud behavior is being correlated with the Pasquill parameters.

For the Dugway munition series, tests D1 and D6 were Pasquill Category C (slightly unstable); the other tests were Category D (neutral). No atmospheric descriptors were available in the pre-liminary Fort Sill data. With the sparsity of data at this time, we will not be able to correlate the analytic parameters with the atmospheric state. We expect a fairly high air entrainment rate due to the initial and induced turbulence during the rise phase. We set α equal to 1, a value not incompatible with our limited data base. We set C_D equal to 0.8. There is considerable scatter in the experimental data; but, on the average, the expansion rate in the horizontal direction is about twice the expansion rate in the vertical direction. With the stated choices of α and C_D, a reasonable fit to the experimental data is to take the vertical expansion rate equal to about 0.92 of the idealized spherical cloud radial expansion rate, and to take the horizontal ex-pansion rate at twice the vertical rate. Lacking any rise experimental data, we simply take the altitude of the munition cloud equal to the spherical cloud altitude. Thus the munition cloud equations during the rise phase are
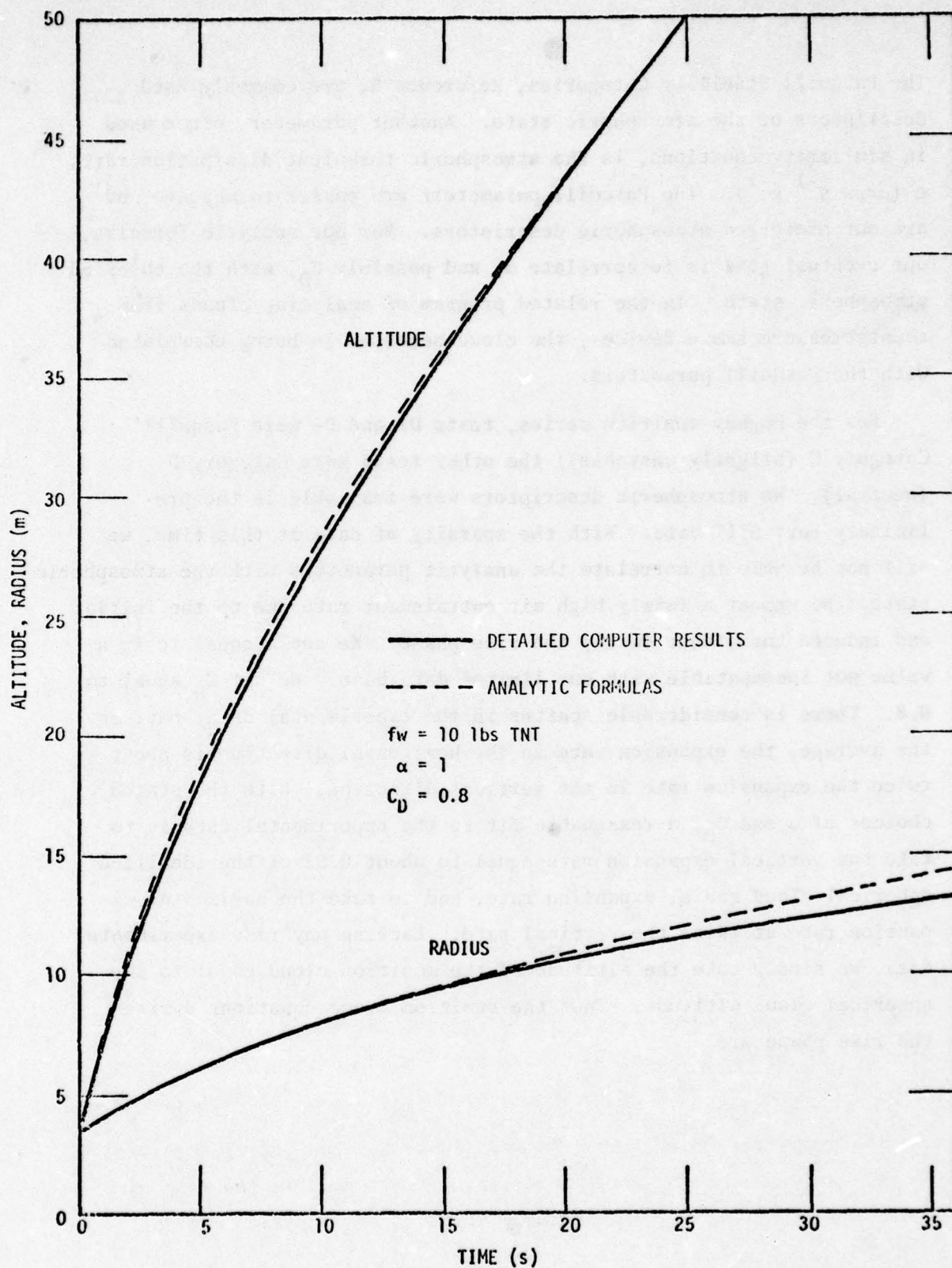
ALTITUDE

RADIUS

DETAILED COMPUTER RESULTS

ANALYTIC FORMULAS

fw = 10 lbs TNT
α = 1
C_D = 0.8

TIME (s)

Figure 9.   Comparison of computer and analytic results
for ideal cloud.

$$R_H(t) = \sqrt{2K_H t + R_{HO}^2} \qquad \text{m} \tag{22}$$

$$R_V(t) = \sqrt{2K_V t + R_{VO}^2} \qquad \text{m} \tag{23}$$

$$H(t) = R_{VO} + 5.31(R_s(t) - R_I) \qquad \text{m} \tag{24}$$

where

R_H = radius in horizontal direction, either cross track or along track

R_V = radius in the vertical direction (m)

K_V = effective vertical turbulent diffusion coefficient

$$= (0.92)^2 K_s = 0.715 \sqrt{fW} \qquad (\text{m}^2 \text{ s}^{-1}) \tag{25}$$

K_H = effective horizontal turbulent diffusion coefficient

$$= 4 K_V \qquad (\text{m}^2 \text{ s}^{-1}) \tag{26}$$

R_I is given by Equation 8 , R_s by Equation 19 with $R_{so} = R_I$. R_{HO} and R_{VO} are calculated from Equation 11.

We are assuming that the effective diffusion in the horizontal plane is independent of direction. Relative to the center of mass of the cloud the diffusion is the same in the cross wind and the down wind directions. Studies of puffs released in the atmosphere have found no evidence to contradict this assumption (Reference 5). Here we are speaking of the hot air cloud and the lightest dust particles which move with the air velocity. Heavier dust particles will lag the air velocities and will fall out, leading to an elongation of the overall dust cloud in the wind direction. In addition, if the vertical dimension of the cloud is large enough, the shear structure of the wind will distort the cloud.

For comparing the analytic formulations with the experimental data, we use the vertical and cross wind test dimensions. In the down wind direction, the length of the primary cloud is not separated in the

reported data from the overall length which includes elongation due to fallout. In our model fallout is treated by considering separate volume elements for the heavier dust particles. There is no doubt which is the vertical dimension in the reported data. For the Dugway data, the width (Y dimension) is obviously the cross wind direction. For the very preliminary Fort Sill data, it is not readily apparent which is the wind direction. After a survey of the length and width data versus time, we conclude that the width dimensions of the Tables 9 through 13 are cross wind dimensions for the Fort Sill tests. At this time the cross wind dimension cannot be determined for the other Fort Sill cases. For the test comparisons the following values were used for the analytic calculations.

Table 14.   Values for Dugway analytic calculations.

Trial	Yield (lbs TNT)	Other Parameters
D1	3.5	
D2	5.0	$f = 0.84$
D3	6.75	$\dfrac{\rho_0}{\rho} = 1.18$
D4	8.0	
D5	15.0	(Dugway elevation $\approx$ 4400 ft)
D6	35.0	$C_T = C_P = C_V = 1$

Table 15. Values for Fort Sill analytic calculations.

Trial	Yield (lbs TNT)	Other Parameters
T - 3	15.0	$f = 0.5$
T-12 to T-20	6.75	$\dfrac{\rho_0}{\rho} = 1.04$
		(Fort Sill elevation $\approx$ 1110 ft)
		$C_T = 2 \quad C_P = 1 \quad C_V = 1/2$

The yields of the 155 and 105 mm Fort Sill rounds were not specified in the preliminary data. Trials D5 and D3 of the Dugway series were simulations of 155 and 105 mm rounds, respectively; so we assume the same yields for the Fort Sill rounds. Figure 10 shows the Fort Sill height data and the analytic model comparison for the 155 mm round test T-3. The fit is excellent; in fact the fit is better than could be expected from the statistical variability. There are no width data for the 155 mm round. Figure 11 shows the height comparisons for the 105 mm Fort Sill rounds. This figure is a good illustration of the variability to be expected from clouds with identical yields. The model is again a good fit to the mean of the test data. The Fort Sill width comparisons for the 105 mm round are shown in Figure 12. The T-16 cloud is considerably broader than the model prediction at later times; otherwise the model is a reasonable fit to the mean width data. Each of the six Dugway tests has a different yield. In order to show all tests on the same figure, we have normalized the dimensions by dividing by $W^{1/4}$. Except for the first several seconds, this normalization will reduce all model predictions to one curve. Figure 13 shows the Dugway height comparisons. There is such a wide variability in the data that it is difficult to assess the model fit. Figure 14 shows the Dugway width comparisons. Except for the anomalous fall off in the size of D1 after 20 seconds, the model is a good fit to the mean of the data.
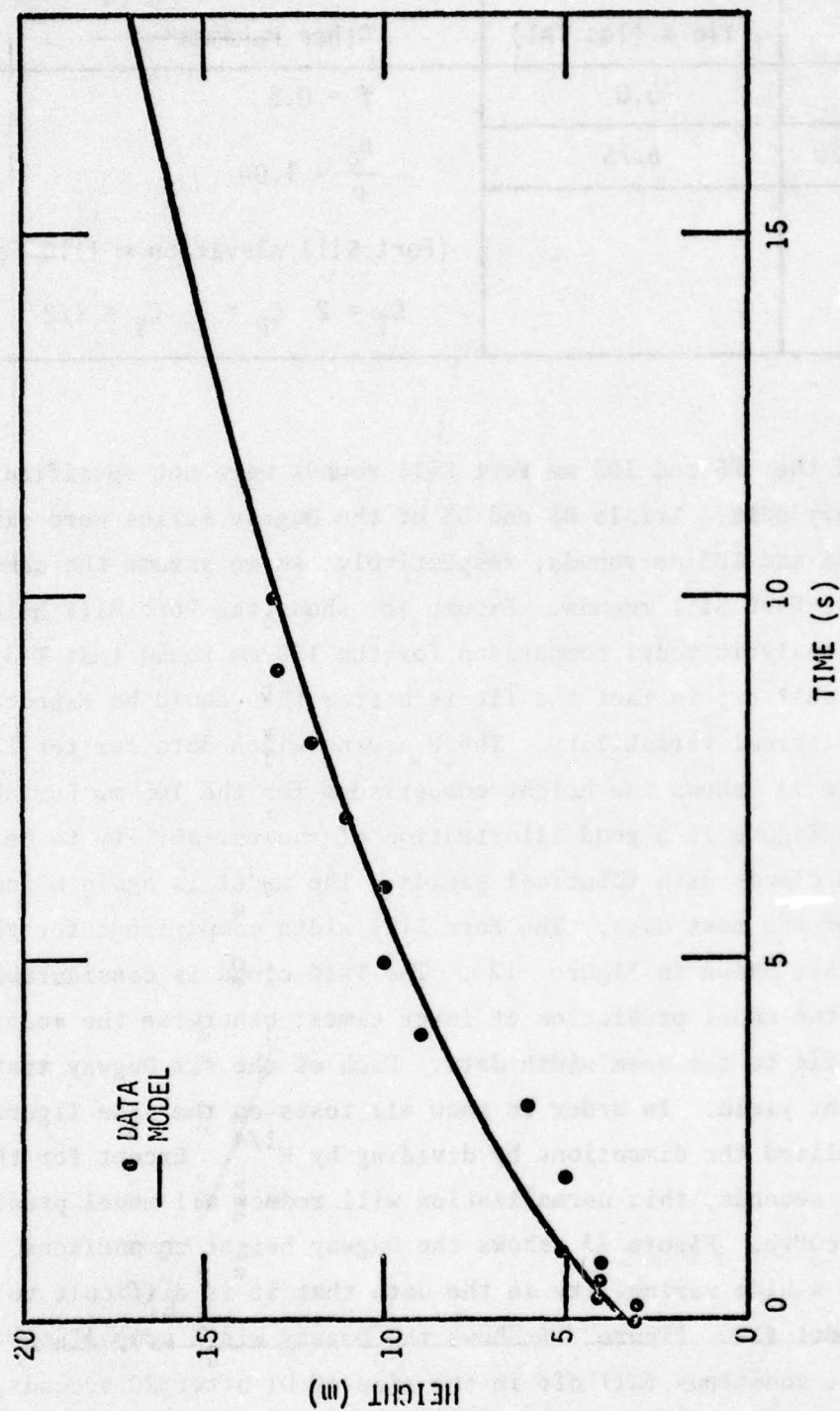
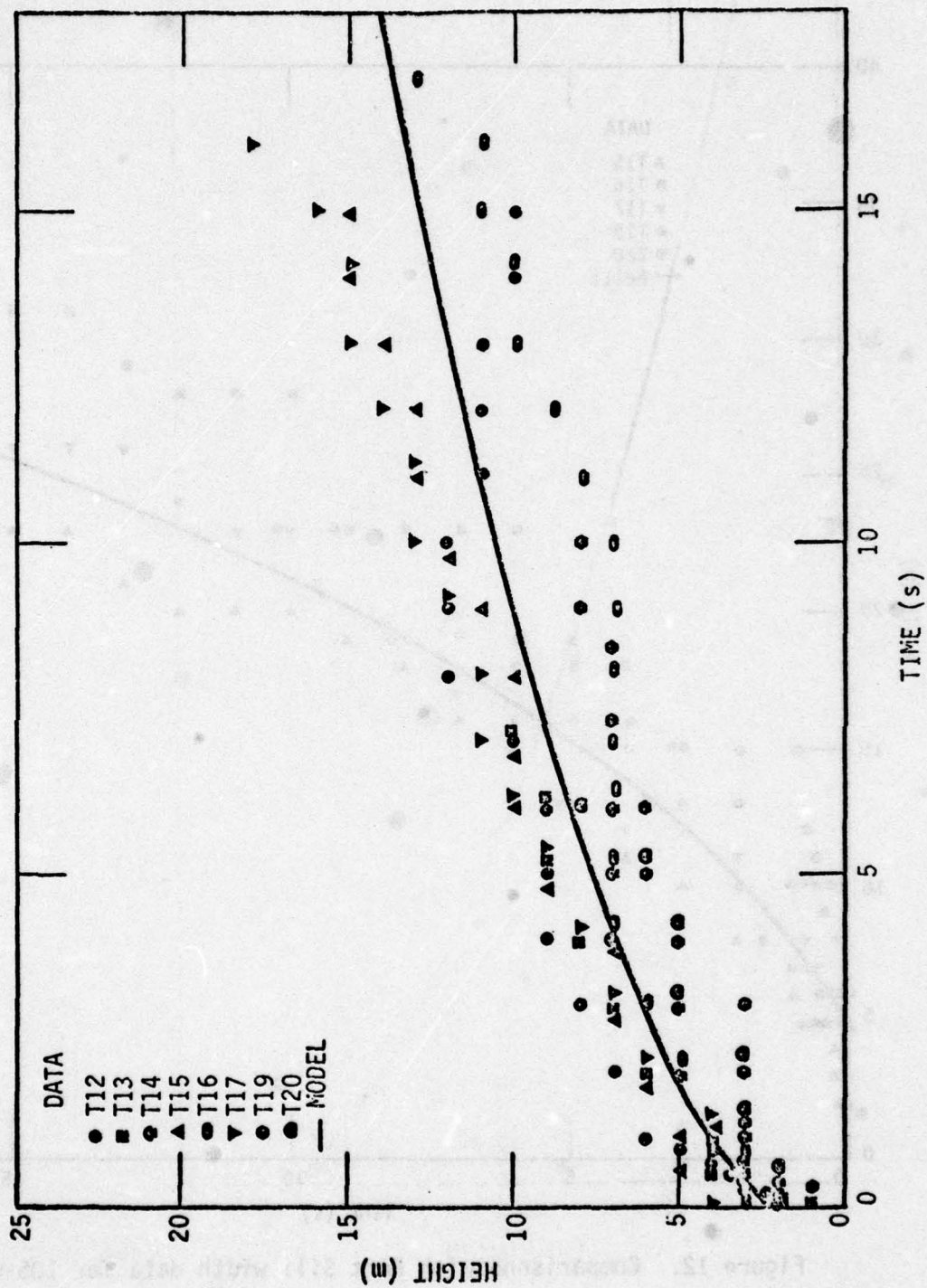Figure 10. Comparison with Fort Sill height data for T3.

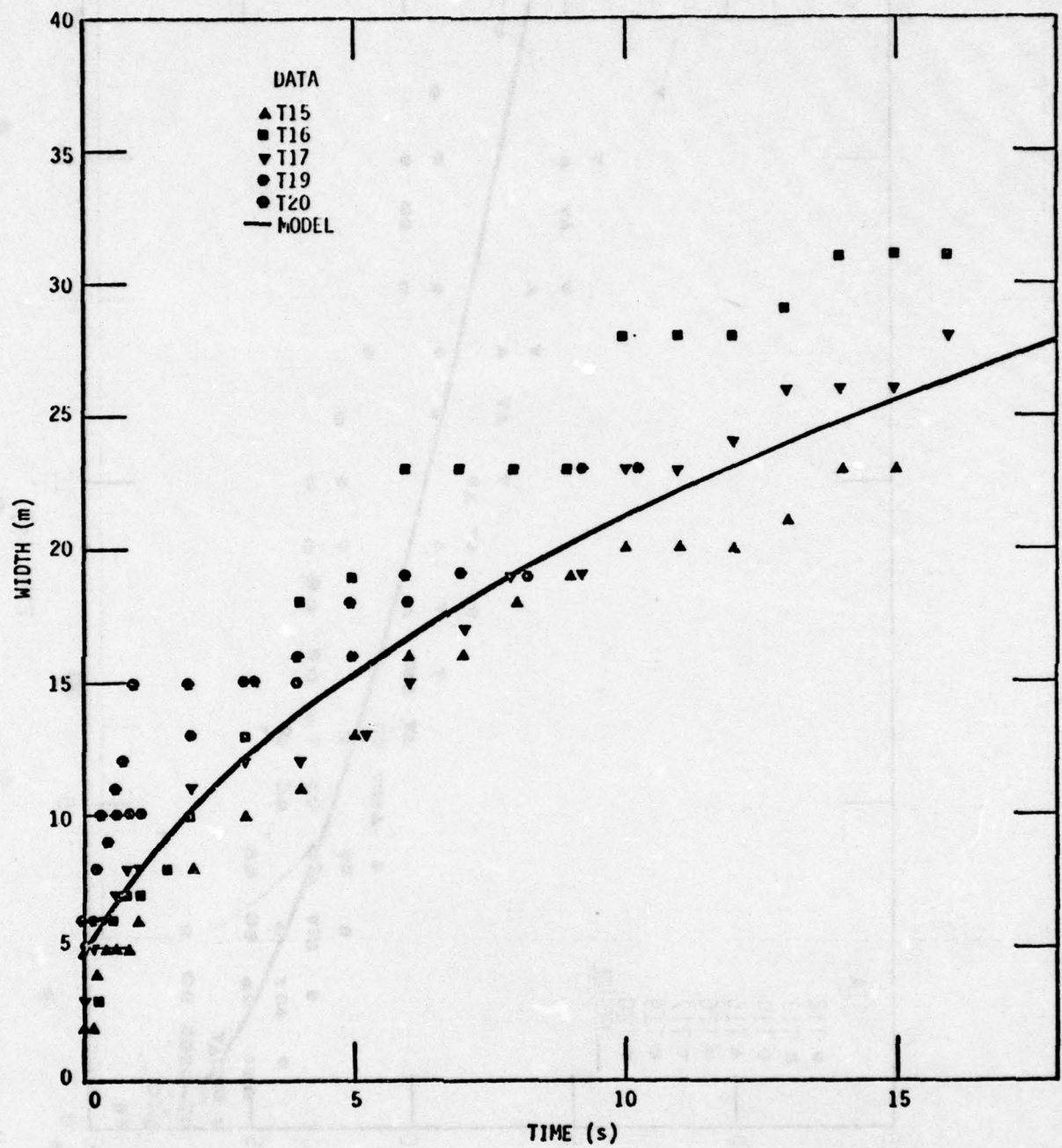Figure 11. Comparisons with Fort Sill height data for 105-mm rounds.

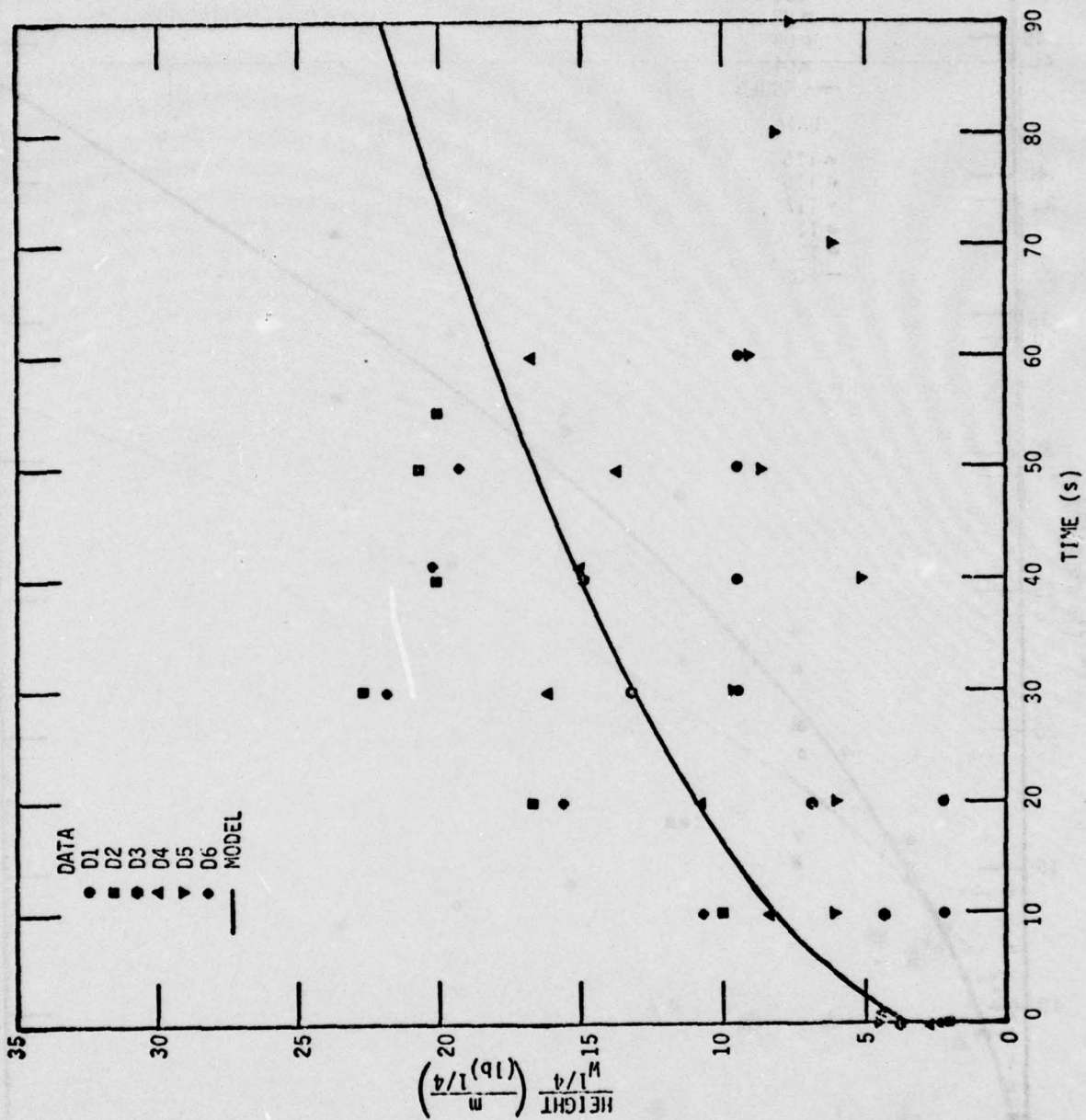Figure 12. Comparisons with Fort Sill width data for 105-mm rounds.

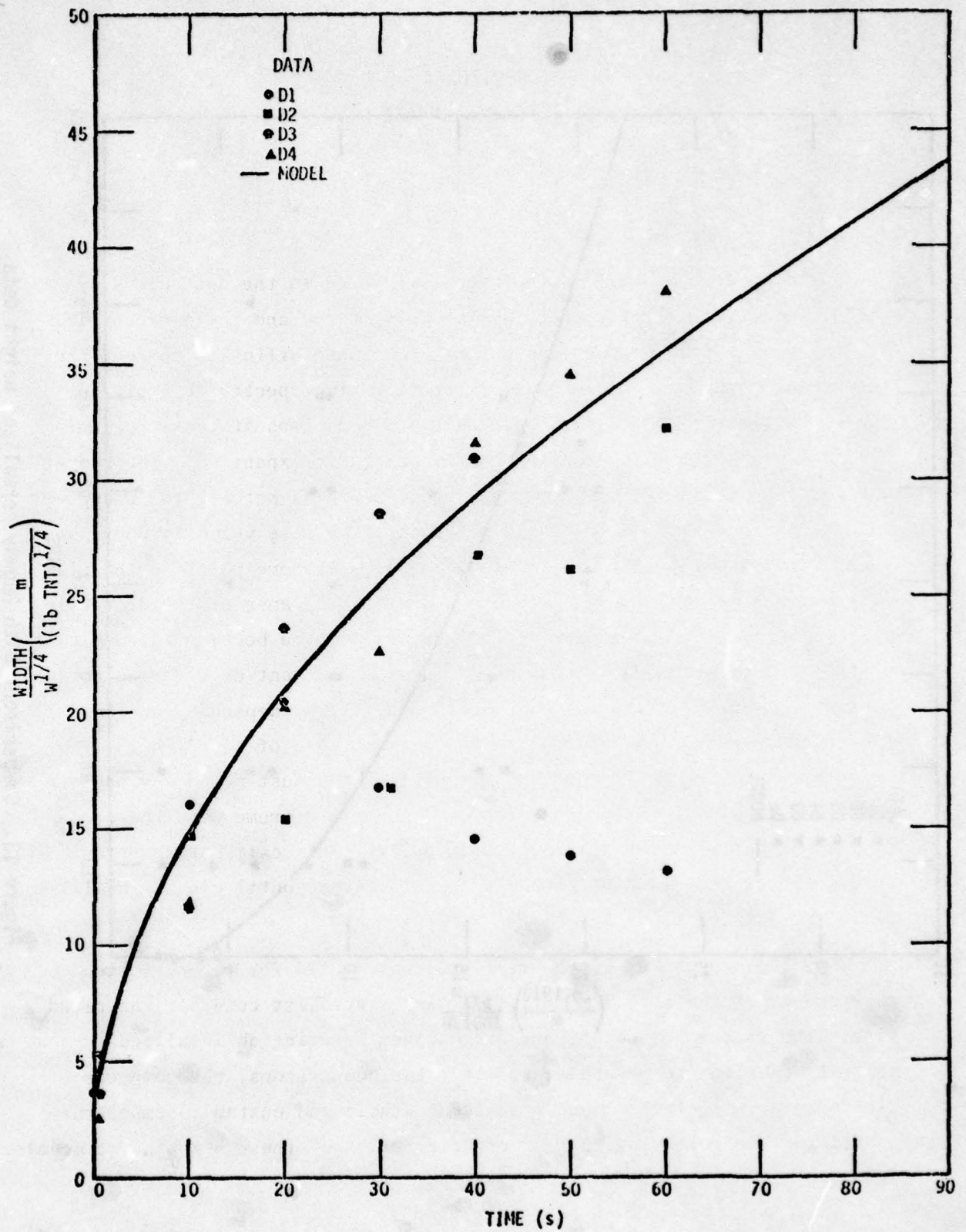Figure 13. Comparisons with Dugway normalized height data.

Figure 14. Comparisons with Dugway normalized width data.

50

SECTION 4
POST RISE PHASE

During the rise phase, turbulence is induced in the dust cloud by
the differential velocity between the rising cloud and the ambient air.
As long as the induced turbulence is the dominant diffusion source, the
rise model equations of the previous section are expected to apply to
the cloud altitude and expansion. As the cloud rises it cools, primar-
ily from mass entrainment but also from adiabatic expansion. The buoy-
ant force is driven by the temperature differential between the cloud
and the ambient air. So as the cloud cools, the rise velocity decreases.
Eventually, the cloud stabilizes in altitude. At some point in the rise
history, the induced turbulence becomes so weak because of the decreasing
rise velocity that the ambient atmosphere turbulence becomes the dominant
diffusion mechanism. The crossover point from buoyant driven rise to
ambient controlled diffusion can occur at any time, depending on the
ambient atmosphere conditions. In the extreme case of a very high
velocity wind with strong ambient turbulence, the dust cloud may be torn
apart and dissipated near ground level. In this extreme case the cross-
over time occurs essentially instantaneously. In a calm stable atmos-
sphere the crossover point probably is not reached until cloud stabili-
zation at late time.

The model equations of the rise phase are valid for the dust cloud
rise and expansion only for a limited time. We first consider the cloud
rise. The rise model equations were derived assuming an idealized
neutral stability temperature profile. For comparisons, the computer
rise program was also run assuming ideal stable and unstable temperature
profiles. The following is a brief description of these atmospheric models.

51

Assume that the ideal exponential pressure equation obtains for some altitude range above the surface. Then in this altitude regime

$$P_A = P_o e^{-\frac{H}{H_{SP}}} \qquad \text{dynes cm}^{-2} \qquad (27)$$

where

P_A = ambient pressure at altitude H (dynes cm^{-2})

P_o = ambient pressure at zero altitude (dynes cm^{-2})

H_{SP} = ambient pressure scale height (m).

The adiabatic lapse rate, Γ, of the atmosphere is the temperature change with altitude due to adiabatic expansion (of a rising cloud or balloon). Using Equation 16 we can write the adiabatic lapse rate as

$$\Gamma = \frac{dT}{dH} = T \left\{ \frac{\gamma-1}{\gamma} \frac{1}{P_A} \frac{dP_A}{dH} \right\} \qquad \text{°K m}^{-1} \qquad (28)$$

For our ideal pressure model

$$\frac{1}{P_A} \frac{dP_A}{dH} = -\frac{1}{H_{SP}} \qquad (29)$$

so that

$$\Gamma = -T \left(\frac{\gamma-1}{\gamma} \right) \frac{1}{H_{SP}} \qquad \text{°K m}^{-1} \qquad (30)$$

For air $\gamma = 1.4$. For the U.S. Standard Atmosphere

$H_{SP} = 8.4 \text{ km} = 8400 \text{ m at sea level}$

$T_o = 288 \text{ °K at sea level}$

so that in the standard case at sea level

$\Gamma = -9.8 \text{ °K km}^{-1} = -9.8 \times 10^{-3} \text{ °K m}^{-1}$.

Let the temperature of a balloon be T_o, the ambient temperature at H = 0. As the balloon rises and expands the adiabatic temperature is

$$T = T_o e^{-\frac{\gamma-1}{\gamma}\frac{H}{H_{SP}}} \quad {}^\circ K \quad . \tag{31}$$

For our rise model atmosphere we take the ambient temperature profile to be

$$T_A = T_o e^{-F_s\left(\frac{\gamma-1}{\gamma}\right)\frac{H}{H_{SP}}} \quad {}^\circ K \tag{32}$$

where

T_A = ambient temperature at altitude H (${}^\circ K$)

T_o = ambient temperature at zero altitude (${}^\circ K$)

F_s = stability factor.

If in a given altitude range the ambient temperature profile is the same as the adiabatic temperature profile, then by definition that portion of the atmosphere has neutral stability with respect to the temperature profile. If the ambient temperature falls off faster with increasing altitude than the adiabatic temperature, the atmosphere is unstable. In a stable atmosphere the adiabatic temperature falls faster than the ambient temperature. For our model atmosphere

F_s = 1 for neutral stability

F_s > 1 for an unstable atmosphere

F_s < 1 for a stable atmosphere.

Let a balloon be at rest at altitude H with the ambient temperature. Let the balloon be displaced slightly in the upward direction and consider the buoyant force on the balloon. In a neutral atmosphere the balloon temperature drop due to adiabatic expansion is identical to the ambient temperature drop; so that after displacement the balloon temperature is still equal to the ambient temperature. The buoyant force on the balloon after displacement is zero. The balloon is "neutral"; after displacement it has no tendency to move either in the up or down directions. Next consider displacement in an unstable atmosphere. After an upward displacement, the balloon temperature will now be higher than the ambient temperature. There will be an upward buoyant force,

53

and the balloon will continue moving in the upward direction. Once displaced from its equilibrium position, the balloon is "unstable." In a stable atmosphere the opposite effect occurs. After upward displacement, the balloon temperature is lower than the ambient temperature. The buoyant force is negative (downward) and the balloon is returned to its previous position; the balloon is in stable equilibrium. Turbulence in the atmosphere will displace parcels of air from their original positions. The turbulent induced motion can be amplified in an unstable atmosphere, suppressed in a stable atmosphere, or unaffected in a neutral atmosphere.

For the model atmosphere the ambient density is taken as

$$\rho_A = \frac{M_o P_A}{R_o T_A} = \frac{P_A}{2.875 \times 10^6 T_A} \qquad g \ cm^{-3} \ . \qquad (33)$$

What are the characteristics of the idealized spherical cloud rise and expansion in the three types of atmospheres? Let P_o and T_o be identical for all three atmospheres. Then the initial cloud will have the same size and temperature in each atmosphere. The fractional decrease in cloud temperature due to adiabatic expansion is the same in each atmosphere and is minor compared to the mass entrainment effect. The temperature profile of the entrained mass is the primary factor controlling the cloud rise and expansion. The early rise and expansion in each atmosphere is essentially identical; it is only after the cloud temperature has fallen to within several degrees of ambient that the differing ambient temperature profiles produce differences in the rise and expansion time histories. As long as the idealized cloud is in a neutral or unstable atmosphere it will continue rising; it will not stabilize until it encounters a stable portion of the atmosphere. The cloud rapidly cools to within a few degrees of ambient, then asymptotically approaches the ambient temperature. In a stable atmosphere, the cloud rises and cools until ambient temperature is reached and the cloud stabilizes. Table 16 shows the stabilization altitudes for ideal clouds in a stable atmosphere with a temperature stability factor of

$$F_S = -1 \ .$$

54

Table 16. Stabilization altitudes in a stable
atmosphere with $F_s = -1$.

Hydro Yield (fW) lbs TNT	Stabilization Altitude, m		
	$\alpha = 0.5$	1	2
1	90	64	46
10	146	103	77
100	239	168	130
1000	390	278	213

Besides using the model atmospheres described here, the rise program can
also use the actual measured atmospheric profiles, if they are known for
a given munitions test. Then the stabilization of the ideal cloud in
the test site atmosphere can be computed.

Thus, given sufficient atmospheric information, we can calculate
the rise and expansion characteristics of any ideal munition cloud.
Unfortunately, the behavior of real munitions clouds can differ signifi-
cantly from an ideal cloud, especially at latter times. Consider an
unstable or neutral atmosphere with the tropopause (temperature invert-
sion) at 10 kilometers. All ideal clouds (and any real adiabatic
balloons) will rise, however slowly, until they encounter the temperature
inversion. We would not expect a real cloud, say from a 1 lb munition
round, to rise 10 kilometers. In a calm windless atmosphere, the 1 lb
cloud might retain its identity long enough to rise several hundred
meters; under turbulent windy conditions, the cloud might not reach 5
meters altitude.

At present, there is little experimental data for guidance. None
of the rise data from the munitions test series have been published.
However, the related problem of the rise of a continuous plume from a
smokestack has been studied, both experimentally and theoretically,
for many years. Cloud and plume rise in the real atmosphere is a very

55

complex process and it is not surprising that no complete and exact theory has emerged. After surveying the theoretical and experimental data, Pasquill (Reference 5) concludes that the best estimate for the stabilization altitude of a continuous plume in a neutral or near neutral atmosphere is the Briggs formula (Reference 6)

$$\Delta H = 5 \frac{F^{1/3} \, X^{*2/3}}{\bar{u}} \qquad m \tag{34}$$

where

ΔH = total rise from altitude of emission (m)

F = stack factor, which depends upon the heat content and temperature of the emitted stack gases ($m^4 s^{-3}$)

$X^* = 0.45 \, F^{2/5} \, (\beta^{-3} \bar{u} \epsilon^{-1})^{3/5}$ (m)

β = ratio of Lagrangian and Eulerian time scales ≈ 4.

ϵ = rate of dissipation of turbulent kinetic energy per unit mass of air (joules $kg^{-1} \, s^{-1}$)

$\bar{u}$ = average wind speed ($m \, s^{-1}$).

Variations of as much as 50 percent from the formula are observed for real plumes. For stabilization in an unstable atmosphere, Briggs concludes that, pending further evidence, the neutral formula given above is the current best estimate, but he emphasizes that larger individual fluctuations must be expected. In terms of $\bar{u}$ and ϵ,

$$H \propto (\bar{u}^3 \, \epsilon^2)^{-1/5} \, . \tag{35}$$

The rise and stabilization of a discrete munitions cloud are expected to differ from those of a continuous plume. We take the stabilization altitude in neutral or unstable conditions to be

$$H_{MAX} = \frac{C_H (fW)^{1/4}}{(\bar{u}^3 \epsilon^2)^{1/5}} \qquad m \tag{36}$$

56

where

$$C_H = \text{constant} \quad .$$

The rise rate of an ideal cloud is proportional to the one-fourth power of the hydro yield. The $\bar{u}$ and ε dependencies were chosen in analogy with the plume analysis. The constants C_H can be set if sufficient experimental data become available from the munitions test series. For rise in a stable atmosphere, we begin with the stabilization altitude predictions of the ideal cloud rise program. We then modify these estimates to account for the average wind and the atmospheric turbulence. Again, final forms will be set when the experimental data become available.

The Briggs formula, Equation 34, and our analogy, Equation 36, are in terms of the atmospheric dissipation parameter ε. This parameter is difficult to measure and is probably not known for most munitions tests. A better technique will be to correlate the stabilization altitudes with the Pasquill Stability Categories, when sufficient data become available.

At some point in the dust cloud rise history, the ambient turbulence becomes the dominant diffusion mechanism. The crossover point depends upon the ambient atmosphere parameters. If the rising cloud encounters a temperature inversion and stabilizes at a relatively early time, then the stabilization time is probably the crossover time. For other clouds, the crossover time will occur during the rise phase.

There are several different approaches we can take for estimating the atmospheric diffusion rates. One approach is to use similarity theory; the similarity equations utilize the dissipation rate parameter, ε. Another method is to correlate the diffusion rates with the Pasquill Stability Categories. We will develop the equations for both the similarity theory and the Stability Categories. We expect to adopt the Stability Category method in our final model, but as yet we do not have sufficient data to make a final choice.

57

In the atmosphere similarity theory and experimental observation indicates that the cloud diffusion due to turbulence has the following time behavior (References 7 and 8). For diffusion in the horizontal direction

$$\frac{d\,\sigma_H^2(t)}{dt} = \begin{cases} 2.66\,C_1(t-t_o)(\varepsilon\sigma_{HO})^{2/3} & t_o \leq t \leq t_o + t_1 \\[3mm] C_2\,\varepsilon(t-t_o)^2 & t \geq t_o + t_1 \end{cases} \tag{37}$$

For diffusion in the vertical direction

$$\frac{d\,\sigma_V^2(t)}{dt} = 2\,K_z \tag{38}$$

where

σ^2 = variance of the cloud concentration (m^2)

σ_{HO}^2 = initial variance of the cloud in the horizontal direction at time t_o (m^2)

t_o = time the neutral cloud (i.e., cloud of same temperature and density of ambient atmosphere) was introduced into the atmosphere (s)

ε = rate of dissipation of turbulent kinetic energy per unit mass of air (joules $g^{-1}\,s^{-1}$)

K_z = effective constant vertical diffusion coefficient ($m^2\,s^{-1}$)

t_1 = transition time from t to t^2 behavior for horizontal diffusion
= $C_3\,\sigma_{HO}^{2/3}\,\varepsilon^{-1/3}$ (s).

C_1, C_2, and C_3 are nondimensional constants of order unity resulting from the dimensional analysis. In our analysis we are assuming that the relationship between the cloud variance and the cloud radius is

$$R(t) = C_r\sigma(t)\quad, \tag{39}$$

where C_r is a constant, generally in the range from 1 to 3. Writing the velocity equations in terms of the radius we have

$$\frac{d\,R_{HA}^2(t)}{dt} = \begin{cases} 2.66\,C_1 C_r^{4/3}\,(\varepsilon\,R_{HOA}^{})^{2/3}(t-t_o)^2 & t_o \le t \le t_o + t_1 \\[1em] C_2 C_r^2\,\varepsilon(t-t_o)^3 & t > t_o + t_1 \end{cases} \tag{40}$$

$$\frac{d\,R_{VA}^2(t)}{dt} = 2\,K_{VA} \tag{41}$$

where

$$K_{VA} = C_r^2\,K_z \tag{42}$$

$$t_1 = C_3 C_r^{-2/3}\,R_{HOA}^{2/3}\,\varepsilon^{-1/3} \quad . \tag{43}$$

The subscript A distinguishes this case of atmospheric diffusion of a neutral cloud from that of a buoyant cloud.

Let the crossover time from buoyantly controlled diffusion to atmospheric diffusion be t_c. We assume the radial expansion equations of the previous section apply for times before t_c, namely

$$R_H^2(t) = 2\,K_H t + R_{HO}^2 \quad m^2 \tag{44a}$$

$$R_V^2(t) = 2\,K_V t + R_{VO}^2 \quad m^2 \qquad 0 \le t \le t_c \quad . \tag{44b}$$

Define the cloud radii at crossover time

$$R_{HC}^2 = 2\,K_H t_c + R_{HO}^2 \quad m^2 \tag{45a}$$

$$R_{VC}^2 = 2\,K_V t_c + R_{VO}^2 \quad m^2 \quad . \tag{45b}$$

Then the vertical diffusion after crossover time is taken to be simply

$$R_V^2(t) = 2\,K_{VA}(t - t_c) + R_{VC}^2 \quad m^2 \qquad t > t_c \quad . \tag{46}$$

The vertical dimension of the cloud is continuous over the crossover time, but the expansion velocity changes discontinuously.

For the horizontal dimension, we assume the following dust cloud diffusion behavior after crossover time

$$R_H^2(t) = \begin{cases} R_{HOA}^2 + 1.33 \ C_1 C_r^{4/3} (\epsilon \ R_{HOA})^{2/3} (t - t_o)^2 & t_c < t \le t_2 \\ R_{3A}^2 + C_2 C_r^2 \dfrac{\epsilon}{3} (t - t_o)^3 & t > t_2 \end{cases} \quad m^2 \qquad (47)$$

We arbitrarily set C_1 equal to unity. The fictitious neutral cloud parameters R_{HOA} and t_o will be set so as to provide size continuity and, if possible, velocity continuity at crossover time t_c. The expansion velocities about t_c are

$$\frac{d \ R_H^2(t)}{dt} = \begin{cases} 2 \ K_H & 0 \le t \le t_c \\ 2.66 \ C_r^{4/3} (\epsilon \ R_{HOA})^{2/3} (t - t_o) & t_c < t \le t_2 \end{cases} \qquad (48)$$

Define

$$t_A = \left(\frac{K_H}{2\epsilon}\right)^{1/2} C_r^{-1} - \frac{R_{HO}^2}{2 \ K_H} \quad s \ . \qquad (49)$$

t_A is the time the atmospheric diffusion velocity equals the buoyant rise expansion velocity. The crossover time is taken as

$$t_c = MIN[t_A, \ t_{ST}] \quad s \qquad (50)$$

where

t_{ST} = stabilization time (s).

When the stabilization time (t_{ST}) occurs before the time the atmospheric diffusion becomes dominant (t_A), the velocity is discontinuous at the crossover time (t_c), with the velocity lower after crossover. This case would correspond to the buoyant cloud encountering a temperature inversion and stabilizing fairly early in time. The atmospheric diffusion rate is still relatively weak when the stabilization ends the buoyant diffusion.

For $t_c = t_A$

$$R_{HOA} = \frac{R_{HC}}{2} \quad m \qquad\qquad (51)$$

$$t_o = -\left[\frac{t_A}{2} + \frac{3 \, R_{HO}^2}{4}\right] \quad s \quad . \qquad\qquad (52)$$

Thus if a neutral cloud of half the size of the munition cloud at cross-over had been released $-t_o$ seconds before detonation time, both the neutral and the munition clouds would have the same size and expansion velocity at crossover time t_c.

For $t_c = t_{ST} < t_A$ we choose R_{HOA} and t_o so as to maximize the expansion velocity at t_c. Thus

$$R_{HOA} = \frac{R_{HC}}{2} \quad m \qquad\qquad (53)$$

$$t_o = t_c - \frac{3}{2}\left(\frac{R_{HC}^2}{4 \, C_r^2 \epsilon}\right)^{1/3} \quad s \quad . \qquad\qquad (54)$$

Next we develop the equations for the Stability Category diffusion. The expansion of plumes from continuous sources (chimney emission, for example) has been the object of extensive theoretical and experimental research. The research indicates that the diffusion in the cross wind and vertical dimensions can be described by

$$\sigma_y = a_y (X_D)^{S_y} \quad m \qquad\qquad (55a)$$

$$\sigma_z = a_z (X_D)^{S_z} \quad m \qquad\qquad (55b)$$

where

a_y, a_z = constants
X_D = downwind distance in the plume at which the σ's are evaluated (m).

For the individual munitions clouds, time instead of downwind distance is the dependent variable. Since

$$X_D = \bar{u}t \tag{56}$$

where

$$\bar{u} = \text{mean wind speed (m s}^{-1})$$

we take the standard deviations to be

$$\sigma_y = b_y(\bar{u}t)^{S_y} \qquad m \tag{57a}$$

$$\sigma_z = b_z(\bar{u}t)^{S_z} \qquad m \tag{57b}$$

Observations indicate that the instantaneous (cloud) and continuous sources have the same power law dependence, but different constant coefficients. The constants and power exponents are functions of the Stability Categories.

For matching the buoyant controlled rise to the atmospheric controlled diffusion we define a fictitious atmospheric controlled cloud which was introduced into the atmosphere at time t_o. We take the radii of the cloud as

$$R_{HA}(t) = C_r b_y(\bar{u}[t-t_{HO}])^{S_y} \qquad m \tag{58a}$$

$$R_{VA}(t) = C_r b_z[\bar{u}(t-t_{vo})]^{S_z} \qquad m \tag{58b}$$

The t_o constants will be defined so as to provide radii continuity at the crossover time. Again, let the crossover time be t_c. Radii continuity requires

$$t_{HO} = t_c - \frac{1}{u}\left(\frac{R_{HC}}{C_r b_y}\right)^{1/S_y} \qquad s \tag{59a}$$

$$t_{vo} = t_c - \frac{1}{u}\left(\frac{R_{VC}}{C_r b_z}\right)^{1/S_y} \qquad s \tag{59b}$$

and R_{HC} and R_{VC} are given in Equation 45. The radius of the munition cloud is given by Equation 44 before crossover time and by Equation 58 after crossover time. The time of crossover will be determined from

62

experimental observations when sufficient data are available.

The rise phase radial expansion behavior is a $t^{1/2}$ variation. Similarity theory predicts that the horizontal radial expansion will change from this $t^{1/2}$ variation to a t and then a $t^{3/2}$ variation. The Stability Category predicts a t^{S_y} variation; S_y varies with the atmosphere stability but is always greater than one half. Examining the horizontal radial expansion data in Figures 12 and 14, we observe no noticeable deviation from the characteristic rise $t^{1/2}$ behavior. Either the cross-over time has not been reached, or the data reduction technique has lost the required accuracy to show the deviation. The radius is taken from photographic data. We are assuming that the measured radius corresponds to a constant fraction of the mass penetrated through the cloud center. As the cloud expands, the edges become wispy and faint on the photographic image. It is difficult to make a consistent measurement as the cloud becomes photographically transparent. Whatever the reason, for the present we have no munitions test data for the expansion behavior after the $t^{1/2}$ rise controlled phase. Hopefully, as more data become available from the munitions tests and the related countermeasures smoke tests, the behavior during the atmospheric controlled phases can be determined.

SECTION 5
DUST MASS LOADING

When a munition round detonates at or below the ground surface, a quantity of soil or rock mass will be lofted into the air. Most of the lofted mass will quickly fall back to earth as crater ejecta and fallback. A smaller fraction of the mass will remain aloft in the dust cloud for long periods. Figure 15 shows a sketch of an idealized crater formed by an explosion. The total mass lofted can be determined by measuring the volume of the true crater,

$$M_T = \rho V_T \qquad g \qquad (60)$$

where

M_T = total mass lofted (g)

ρ = average density of soil (g cm^{-3})

V_T = volume of true crater (cm^3).

By gathering and weighing the crater fallback and ejecta, the mass lofted into the dust cloud can be determined

$$M_C = M_T - M_F - M_E \qquad g \qquad (61)$$

where

M_C = dust mass lofted into the cloud which remains aloft for long periods (g)

M_F = mass in crater fallback (g)

M_E = mass in crater ejecta (g).

Terlecky (References 9 and 10) has made careful mass measurements on 5 craters from 8 lb TNT detonations and 1 crater from a 1000 lb TNT detonation. Not surprisingly, most crater data consist of the apparent crater measurements - radius, depth and volume. We assume that the total mass lofted and the dust cloud mass are related to the apparent crater volume by

$$M_T = F_T \rho V_A \qquad g \qquad (62a)$$
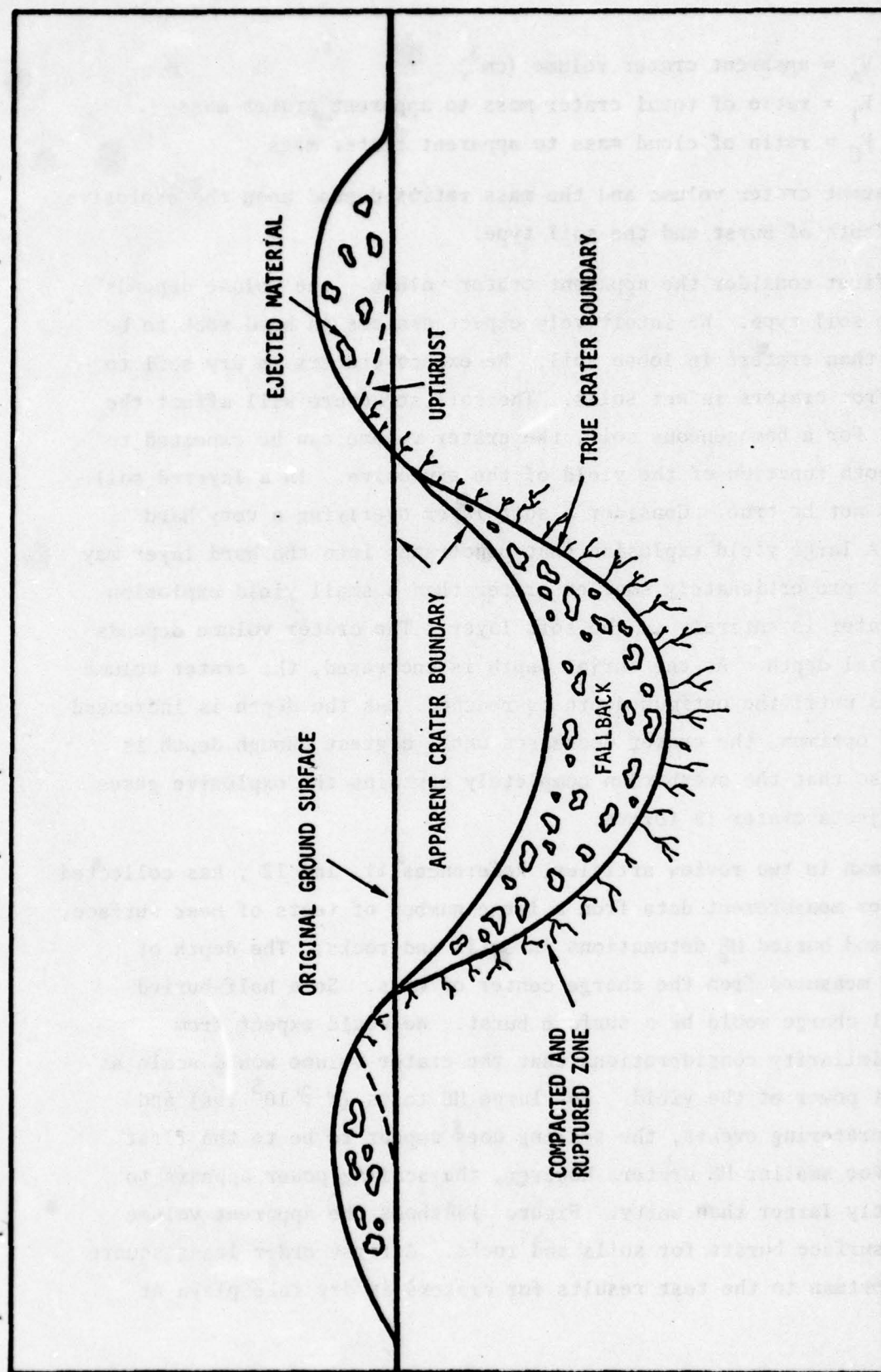
$$M_C = F_C \rho V_A \qquad g \qquad (62b)$$

64

Figure 15. Ideal crater geometry.

where

$$V_A = \text{apparent crater volume (cm}^3)$$
$$F_T = \text{ratio of total crater mass to apparent crater mass}$$
$$F_C = \text{ratio of cloud mass to apparent crater mass}$$

The apparent crater volume and the mass ratios depend upon the explosive yield, depth of burst and the soil type.

We first consider the apparent crater volume. The volume depends upon the soil type. We intuitively expect craters in hard rock to be smaller than craters in loose soil. We expect craters in dry soil to differ from craters in wet soils. The soil structure will affect the crater. For a homogeneous soil, the crater volume can be expected to be a smooth function of the yield of the explosive. In a layered soil this may not be true. Consider a soft layer overlying a very hard layer. A large yield explosion that penetrates into the hard layer may produce a proportionately smaller crater than a small yield explosion whose crater is entirely in the soft layer. The crater volume depends upon burial depth. As the burial depth is increased, the crater volume increases until the optimum depth is reached. As the depth is increased past the optimum, the crater decreases until a great enough depth is reached so that the overburden completely contains the explosive gases and no ejecta crater is formed.

Vortman in two review articles, References 11 and 12 , has collected the crater measurement data from a large number of tests of near surface, surface and buried HE detonations in soils and rocks. The depth of burst is measured from the charge center of mass. So a half-buried spherical charge would be a surface burst. We would expect from simple similarity considerations that the crater volume would scale as the first power of the yield. For large HE tests (W $\gtrsim 10^5$ lbs) and nuclear cratering events, the scaling does appear to be to the first power. For smaller HE craters however, the scaling power appears to be slightly larger than unity. Figure 15A shows the apparent volume for TNT surface bursts for soils and rocks. A first order least square fit by Vortman to the test results for craters in dry lake playa at
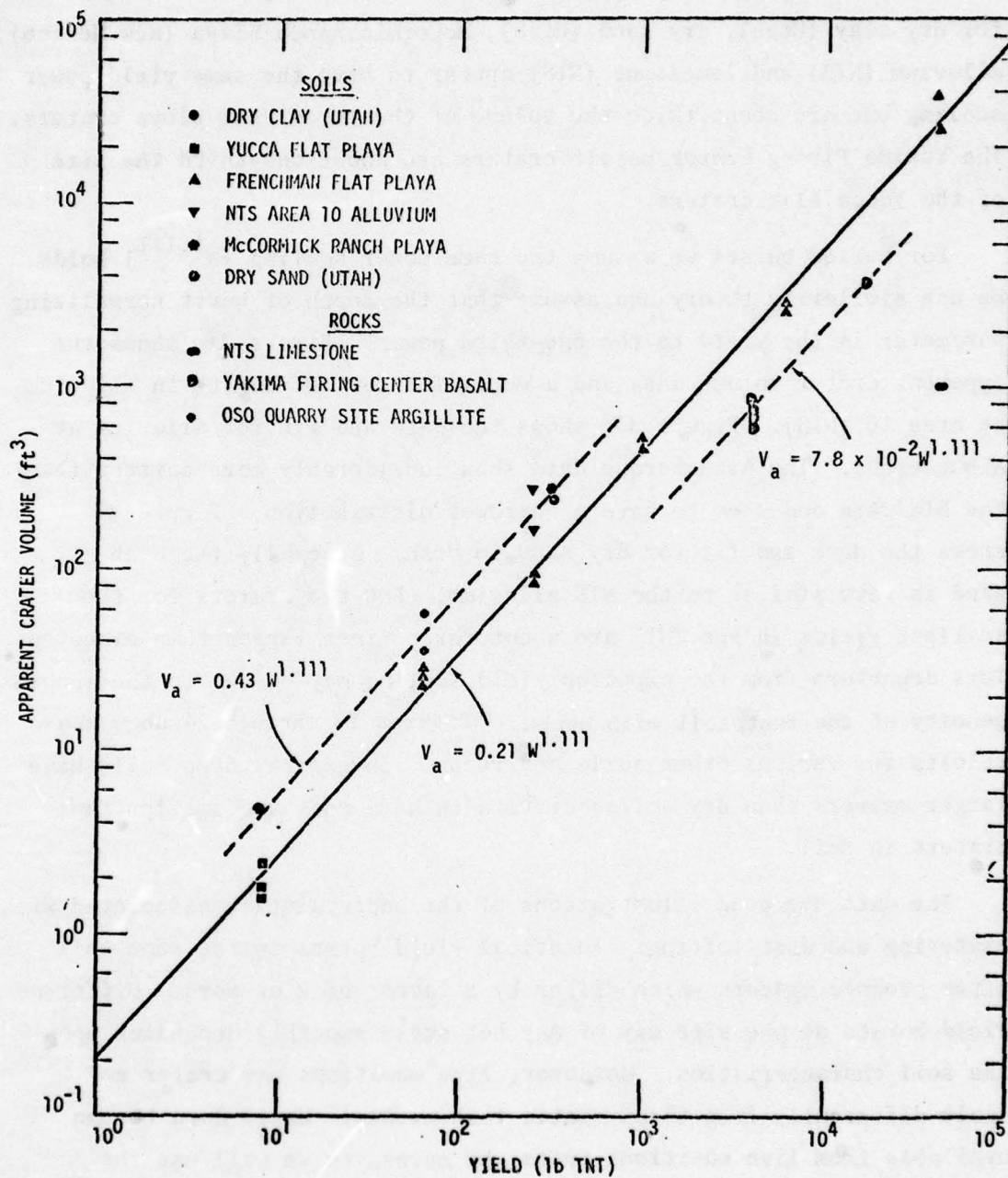
66

Figure 15A. Apparent crater volume for surface bursts.

67

Frenchman Flat at the Nevada Test Site (NTS) indicates a scaling of

$$V_A = 0.21 \ W^{1.111} \qquad ft^3$$

$$= 2.8 \times 10^4 W^{1.111} \qquad cm^3 \tag{63}$$

The Yucca Flat playa also appears to fit this scaling. The craters for dry clay (Utah), dry sand (Utah), McCormic Ranch Playa (New Mexico), alluvium (NTS) and limestone (NTS) appear to have the same yield power scaling but are about twice the volume of the Yucca Flat playa craters. The Yakima Firing Center basalt craters are about one-third the size of the Yucca Flat craters.

For buried bursts we assume the same power scaling ($W^{1.111}$) holds. We use similarity theory and assume that the depth of burst normalizing parameter is the yield to the one-third power. Figure 16 shows the apparent crater volume data and a model fit for TNT bursts in alluvium at area 10 (NTS). Figure 17 shows the data and fit for alluvium at Albuquerque. The Albuquerque data show considerably more scatter than the NTS data and seem to have a narrower distribution. Figure 18 shows the data and fit for dry sand in Utah. Generally the Utah dry sand is very similar to the NTS alluvium. But the craters for the smallest yields (8 lbs TNT) are about three times larger than expected. This departure from the expected yield scaling may be due to the inhomogeneity of the test soil with depth. Figures 19 through 24 show the results for various other soils and rocks. In general damp soils have larger craters than dry soils; craters in hard rock are smaller than craters in soil.

The data are good illustrations of the uncertainties associated with cratering and dust lofting. Identical yield bursts in the same soil often produce craters which differ by a factor of 2 or more. Different yield bursts at one site may or may not scale smoothly depending upon the soil characteristics. Moreover, live munitions may crater and scale differently from these static test events. Until data become available from live munitions tests, by necessity we will use the

Figure 16. Apparent crater volume for buried bursts in NTS alluvium.
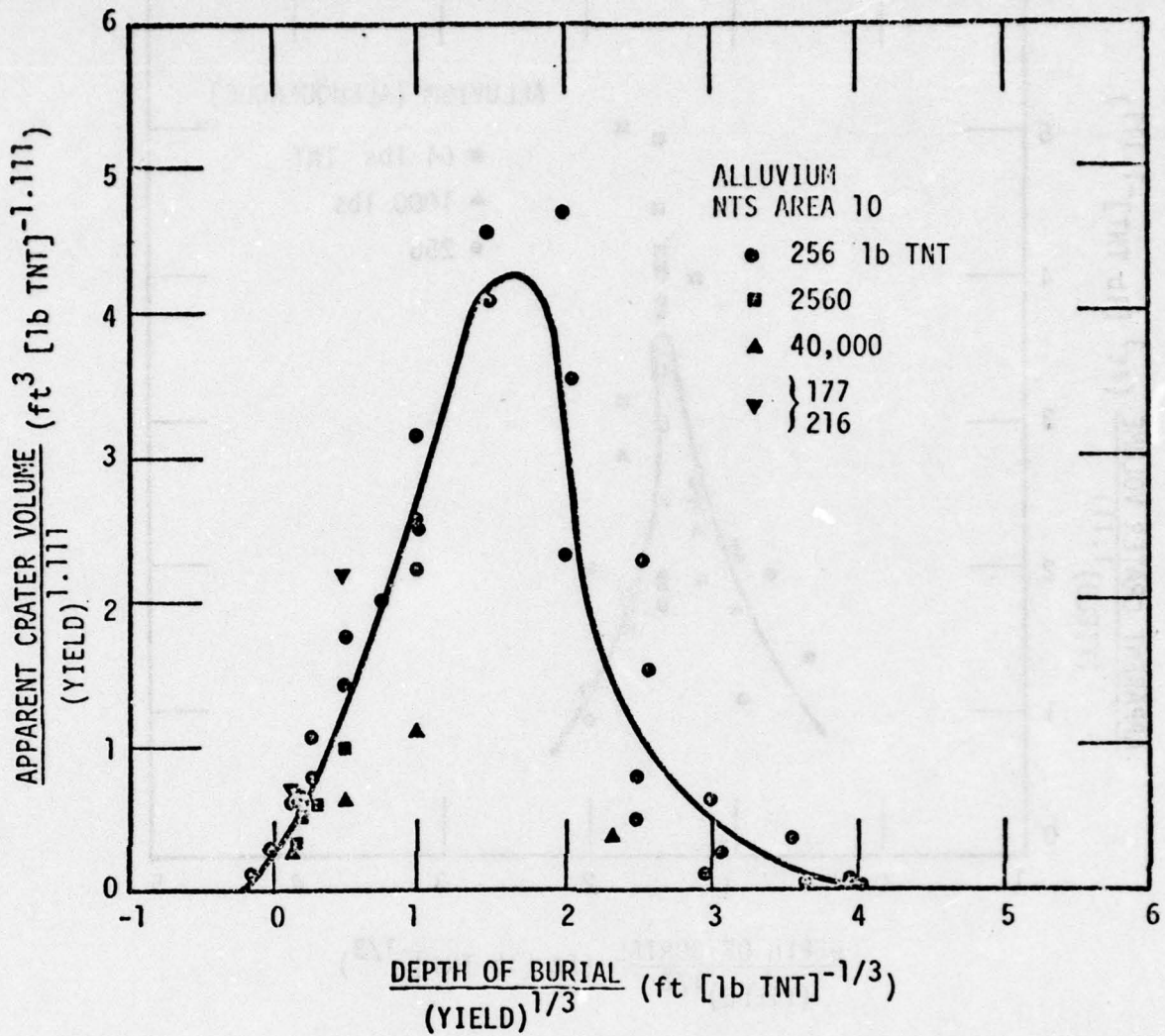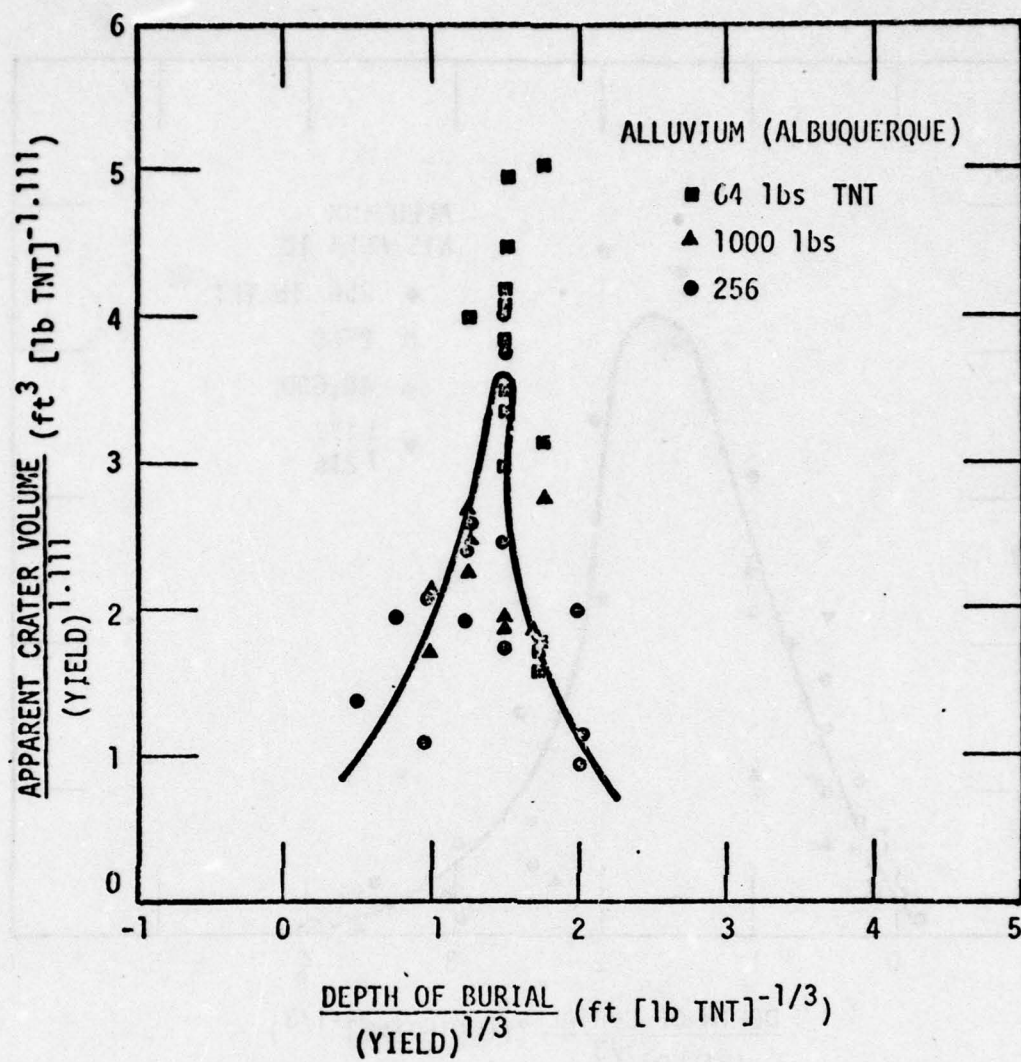
Figure 17.   Apparent crater volume for buried bursts in Albuquerque alluvium.

Figure 18. Apparent crater volume for buried bursts in Utah dry sand.
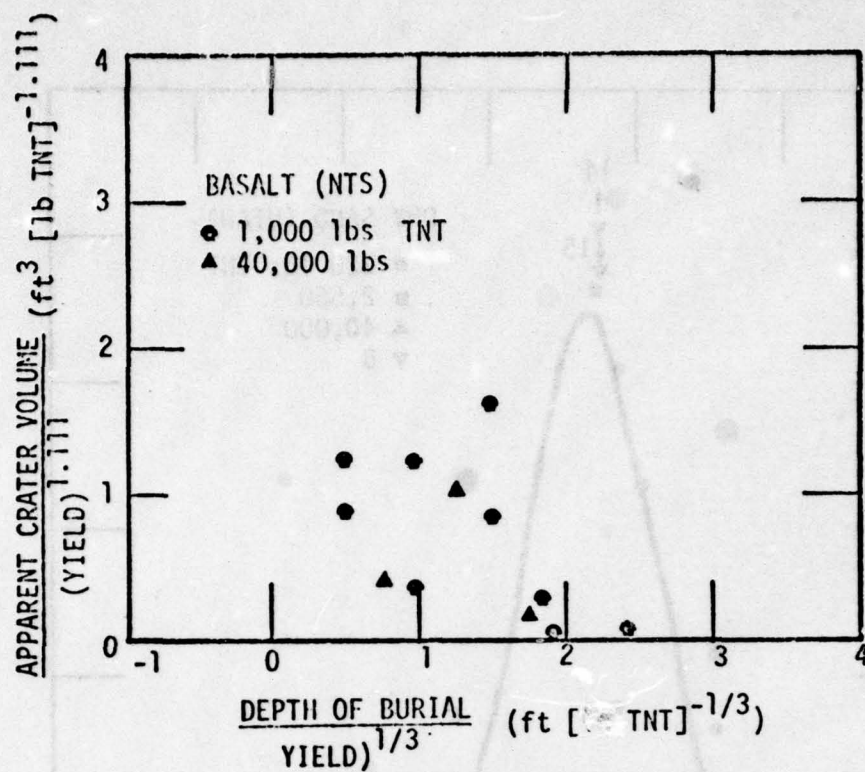
Figure 19.   Apparent crater volume for buried
bursts in NTS basalt.

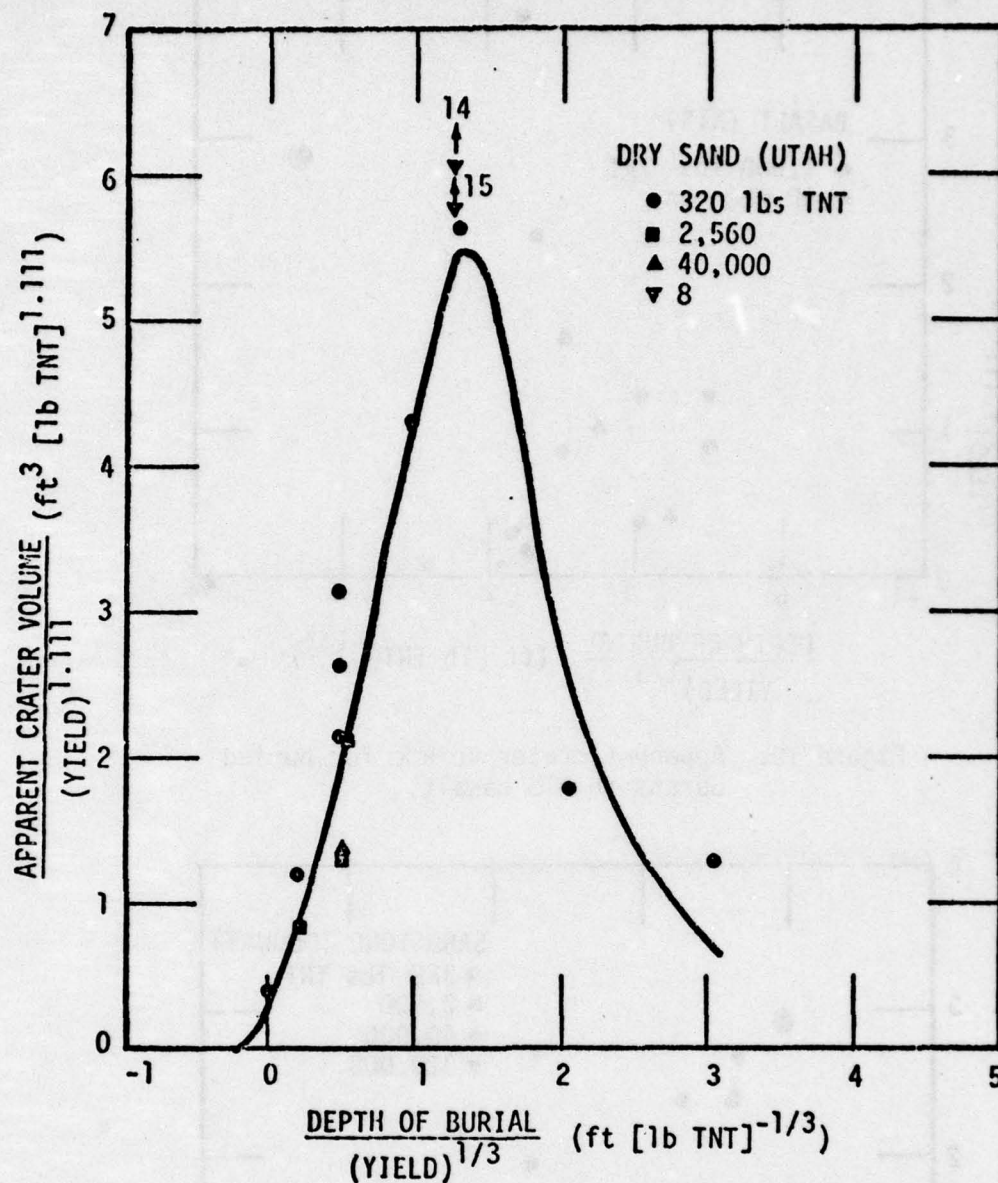Figure 20.   Apparent crater volume for buried
bursts in Utah sandstone.

72

Figure 21.   Apparent crater volume for buried bursts in Utah dry clay.

73

Figure 22. Apparent crater volume for buried bursts in California wet sand and moist clay.

74
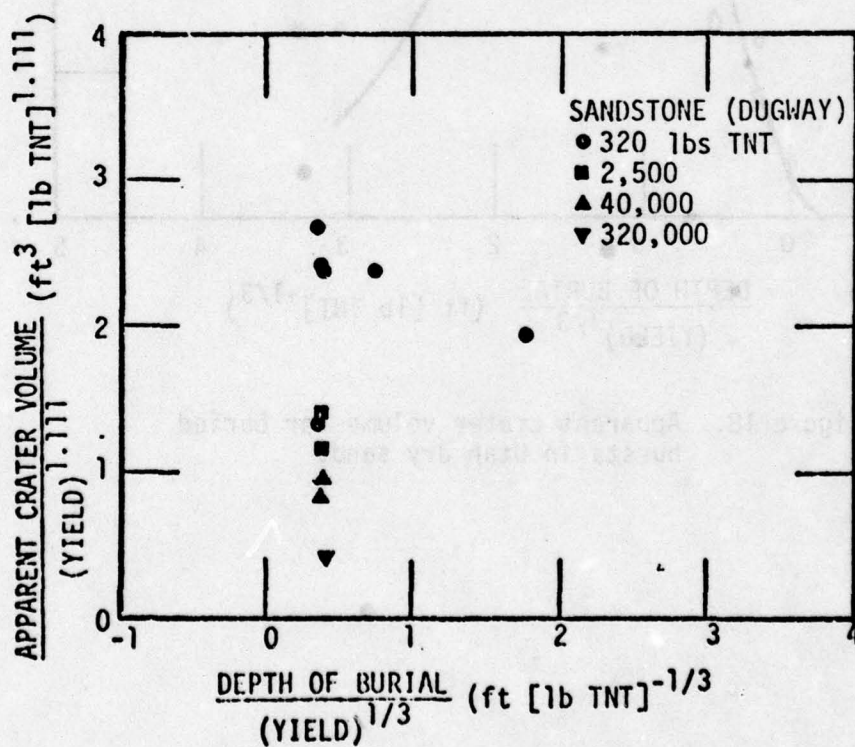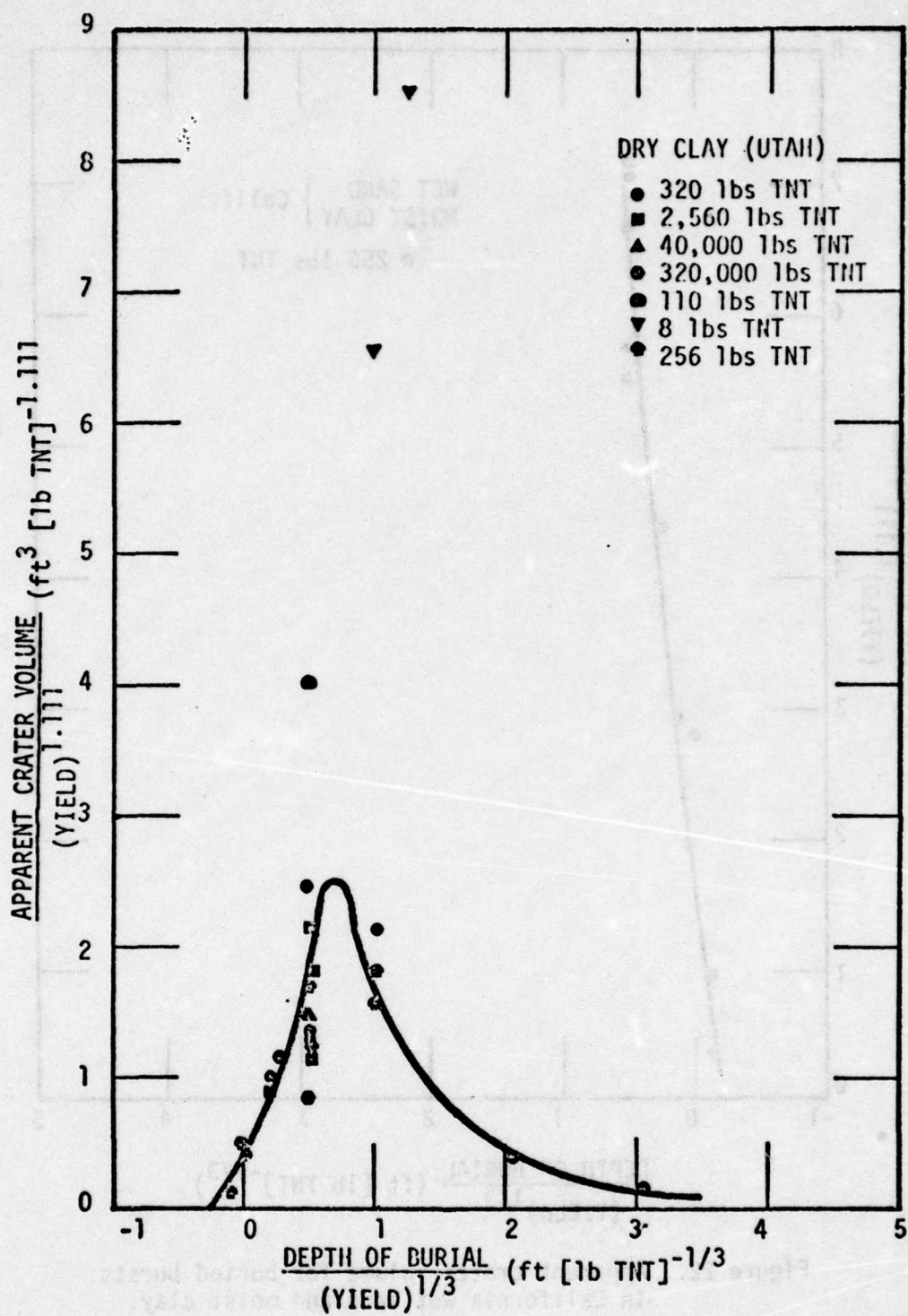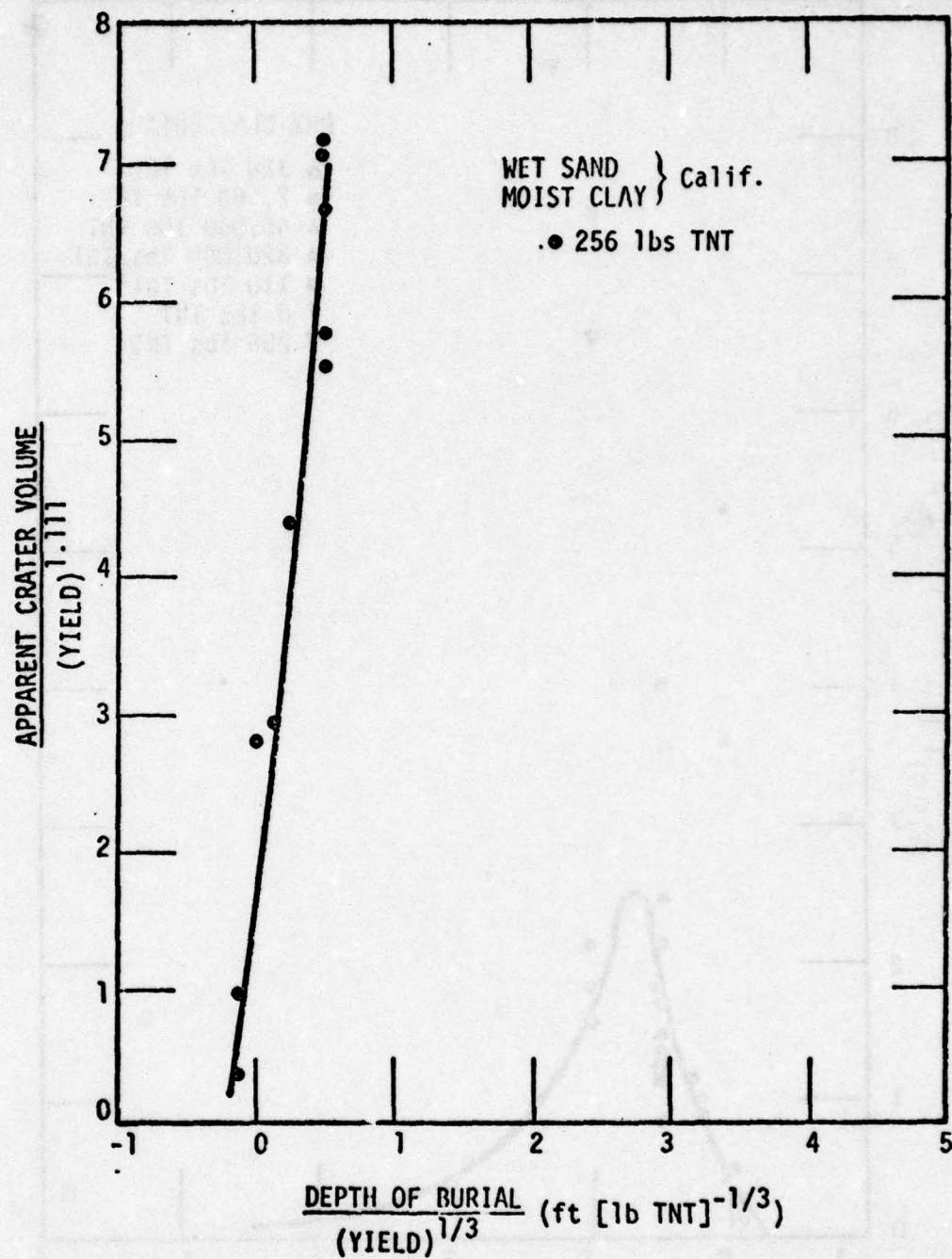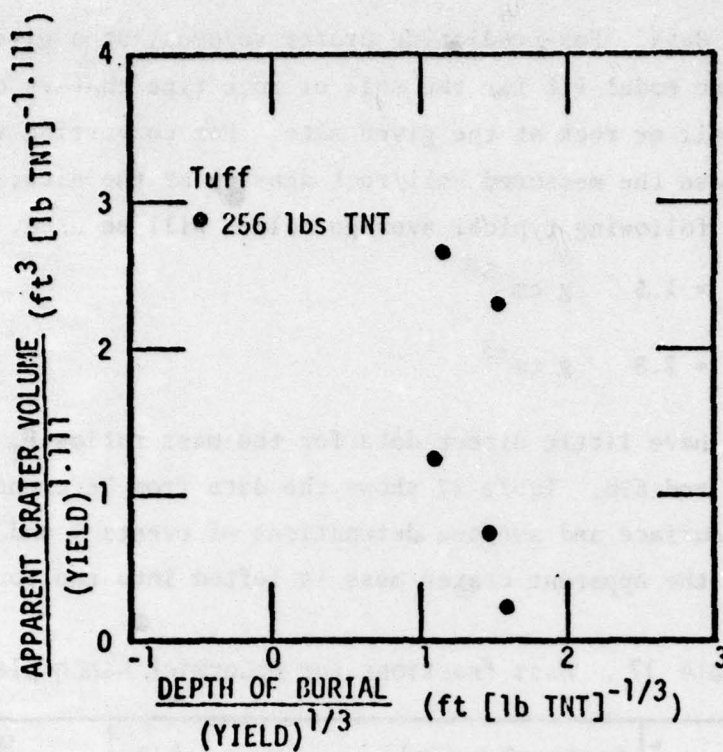
Figure 23. Apparent crater volume for bursts in tuff.
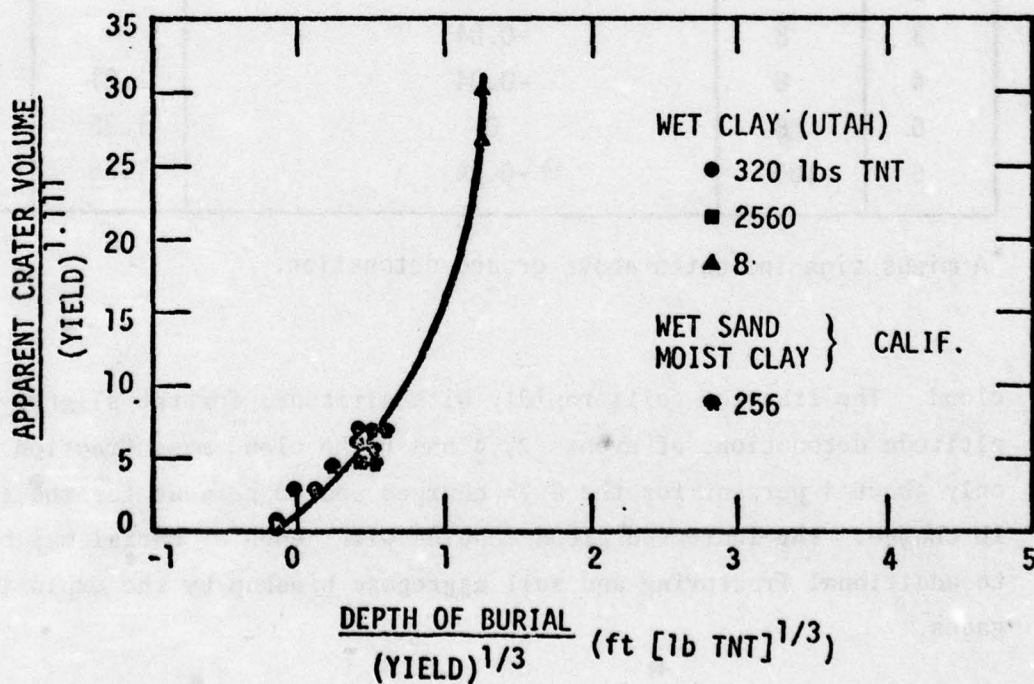
Figure 24. Apparent crater volume for buried bursts in wet soils.

static crater data. For predicting crater volumes, at a given site, we will use the model fit for the soil or rock type that is closest to the type of soil or rock at the given site. For converting volume to mass we will use the measured soil/rock density at the site, if known. Otherwise the following typical average values will be used.

$$\bar{\rho}_{SOIL} = 1.5 \quad g \ cm^{-3}$$

$$\bar{\rho}_{ROCK} = 2.8 \quad g \ cm^{-3}$$

At present we have little direct data for the mass ratios F_T and F_C of equations 62a and 62b. Table 17 shows the data from Reference 10. For the near surface and surface detonations of events 1 and 5, about 25 percent of the apparent crater mass is lofted into the long lasting

Table 17. Mass fractions for McCormick Ranch playa.

Event	Yield (lb TNT)	$\dfrac{Depth \ of \ Burial}{Yield^{1/3}}$ (ft [lb TNT]$^{-1/3}$)	$F_T = \dfrac{M_T}{M_A}$	$F_C = \dfrac{M_C}{M_A}$
1	8	-0.02*	1.21	0.27
2	8	-0.04	1.98	0.040
3	8	-0.04	--	--
4	8	-0.04	2.21	0.044
5	8	0	1.35	0.24
6	1000	-0.04	1.66	0.099

*A minus sign indicates above ground detonation.

cloud. The fraction falls rapidly with altitude; for the slightly higher altitude detonations of events 2, 4 and 6 the cloud mass fraction is only about 4 percent for the 8 lb charges and 10 percent for the 1000 lb charge. The increased cloud loading with depth of burial may be due to additional fracturing and soil aggregate breakup by the explosive gases.

76

The transmission experiments of the munitions test series will provide a source of indirect data for dust cloud loading. The dust mass penetrated along the transmission path can often be deduced from the test data. Utilizing photographic data to estimate cloud size, the total dust mass in the cloud can be calculated. When sufficient munitions test data become available, they will become our basic data base. Until that time we utilize the existing static charge data.

SECTION 6
DUST PARTICLE SIZE DISTRIBUTIONS

For reader convenience we reproduce the first five pages of Section 3 of Reference 13. The equations governing the two most common and one special particle size distributions are discussed.

The two most common probability distributions used to describe particulate (whether dust, smoke, haze, fog, rain, or debris) size statistics are the power law and the log-normal distributions. The power law probability distribution is

$$P_p(a) = \frac{(p-1)\, a^{-p}}{a_{min}^{-(p-1)} - a_{max}^{-(p-1)}} \qquad a_{min} \le a \le a_{max} \tag{64}$$

where

a = particle diameter (cm)

$P_p(a)\, da$ = fraction of the particles with diameters between n and a + da

p = power law exponent

a_{min} = minimum particle diameter in the distribution (cm)

a_{max} = maximum particle diameter in the distribution (cm).

The log-normal distribution is

$$P_L(a) = \frac{e^{-\frac{1}{2}\left[\frac{\ln a/a_m}{\ln S}\right]^2}}{\sqrt{2\pi}\, a\, \ln S} \qquad 0 \le a \le \infty \tag{65}$$

where

a_m = mean particle diameter (cm)

S = standard deviation parameter.

The two distributions given are probability distributions, ie;

78

$$\int_{a_{min}}^{a_{max}} P_p(a) \, da = \int_0^\infty P_L(a) \, da = 1 \quad . \tag{66}$$

Let

N_{TP} = total number of particles in the power law distribution

N_{TL} = total number of particles in the log-normal distribution,

then

$$f_p(a) = N_{TP} P_p(a)$$

$$f_L(a) = N_{TL} P_p(a)$$

are the number distributions for the two cases, where

$f_p(a) \, da$ = number of particles in the power law distribution which have diameters between a and a + da.

Let

M_T = total mass of particulates (g)

ρ_b = bulk density of the particulate material (g cm^{-3}),

then

$$N_{TP} = \frac{M_T}{\frac{\pi}{6} \rho_b (a^3)_p} \tag{67a}$$

$$N_{TL} = \frac{M_T}{\frac{\pi}{6} \rho_b \overline{(a^3)_L}} \quad , \tag{67b}$$

where

$$\overline{(a^3)_p} = \int_{a_{min}}^{a_{max}} a^3 P_p(a) \, da$$

$$= \frac{p-1}{a_{min}^{-(p-1)} - a_{max}^{-(p-1)}} \begin{cases} \ln \dfrac{a_{max}}{a_{min}} & p = 4 \\[2ex] \dfrac{1}{4-p}\left[a_{max}^{4-p} - a_{min}^{4-p} \right] & p \neq 4 \end{cases} \tag{68}$$

79

$$\overline{(a^3)}_L = \int_0^\infty a^3 P_L(a) \ da = a_m^3 \ e^{\frac{9}{2} [\ell n \ S]^2} \ . \tag{69}$$

Condensates, such as water droplets or the particles reformed from the weapon vaporized material, are generally well described by the log-normal size distribution. Some typical values used in previous particulate models are $a_m = 1.4 \times 10^{-5}$ cm (0.14 μm), $S = 1.9$ for recondensed weapon material particulates and $a_m = 5 \times 10^{-4}$ cm (5 μm), $S = 2.0$ for water droplets within a nuclear cloud.

Dust and crater ejecta particulates are generally better described by a power law distribution, at least for particles greater than a few hundredths of a centimeter in diameter. Experimental data from a number of HE (high explosive) and nuclear tests, References 14 and 15, indicate that typical values for the power law exponent are $p \sim 3.5$ for rock and cohesive soils (such as clay or shale) and $p \sim 4$ for loose unconsolidated soils (such as desert alluvium or sand). Fine soils may have $p \sim 5$.

The log-normal distribution is well behaved mathematically at both limits of small and large particle diameters. The power law distribution is not well behaved at either limit. As a_{min} goes to zero both the probability distribution $P_p(a_{min})$ and the total number of particles N_{TP} go to infinity. As a_{max} goes to infinity, the probability distribution $P(a_{max})$ goes to a well behaved zero, but N_{TP} goes to zero for a finite M_T. There are several techniques employed to eliminate mathematical difficulties at the endpoints. The most common technique, and the one we implicitly assumed when we defined the power law, is simply to cut the distribution off at some lower and upper limits, a_{min} and a_{max}. Another technique is to assume an upper limit, a_{max}, but to attach a mathematically well behaved tail at the lower end of the distribution. This lower limit tail can be some artificial mathematical expression chosen for computational convenience, or, as is often the case, can be a fit to the actual experimental data in the small particle limit.

80

SAI, Reference 15, reviewed the experimental data on dust particle size distributions from nuclear test events. They then analyzed in detail the more recent (and more complete) dust size data from HE tests. Their conclusion was that the small size particles have a log-normal size distribution, while the larger particles have a power law size distribution. The size division between small and large particles occurs at a particle diameter of about 0.018 cm (180 μm). We will develop the equations for the hybrid size distribution of a log-normal small-limit tail attached to a power law distribution.

The hybrid probability distribution is given by

$$P_H(a) = \begin{cases} C_1 P_L(a) & 0 \le a \le a_{min} \\ \\ C_2 P_p(a) & a_{min} \le a \le a_{max} \end{cases} \tag{69}$$

where C_1 and C_2 are normalization constants which ensure that

$$\int_0^{a_{max}} P_H(a)\ da = 1 \tag{70}$$

$$C_1 P_L(a_{min}) = C_2 P_p(a_{min}) \quad , \tag{71}$$

ie, the constants ensure that the total probability distribution is properly normalized to unity and that the log-normal and the power law distributions join at a_{min}. C_1 and C_2 are given by

$$C_1 = \frac{P_p(a_{min})}{P_L(a_{min})} C_2 \tag{72}$$

$$C_2 = \left[1 + F_U \left(\frac{\ell n \frac{a_{min}}{am}}{\ell n\ S} \right) \frac{P_p(a_{min})}{P_L(a_{min})} \right]^{-1} \quad , \tag{73}$$

where

81

$$F_U(x) = \frac{1}{\sqrt{2\pi}} \int_{-\infty}^{x} e^{-\frac{1}{2}t^2} dt \tag{74}$$

= cumulative probability of the standardized normal random probability distribution.

For the hybrid distribution,

$$\overline{(a^3)}_H = \int_0^{a_{max}} a^3 P_H(a) \, da = C_1 \int_0^{a_{min}} a^3 P_L(a) \, da + C_2 \int_{a_{min}}^{a_{max}} a^2 P_p(a) \, da$$

$$= C_1 \overline{(a^3)}_L \ F_U \left(\frac{\ln \frac{a_{min}}{am}}{\ln S} - 3 \ln S \right) + C_2 \overline{(a^3)}_p \tag{75}$$

and the total number of particles for a given mass M_T is

$$N_{TH} = \frac{M_T}{\frac{\pi}{6} \rho_b \overline{(a^3)}_H} \quad . \tag{76}$$

For the hybrid distribution, the fraction of the total number of particles in the power law segment and the log-normal segment is

$$f_{NP} = \frac{(N_{TH})_P}{N_{TH}} = C_2 \tag{77a}$$

$$f_{NL} = \frac{(N_{TH})_L}{N_{TH}} = 1 - C_2 \quad . \tag{77b}$$

The fractions of the total dust mass which lie in the two segments are

$$f_{MP} = \frac{(M_T)_P}{M_T} = C_2 \ \frac{\overline{(a^3)}_P}{\overline{(a^3)}_H} \tag{78a}$$

$$f_{ML} = \frac{(M_T)_L}{M_T} = 1 - f_{MP} \quad . \tag{78b}$$

In the SAI analysis the smallest particles measured were on the order of about 0.002 cm (20 μm). The smaller particles were no interest for the problem being analyzed. However, these smaller particles may be very significant with respect to visible and infrared transmission through late-time munition dust clouds. We require improved small particle statistics.

Patterson and Gillette, Reference 16 , have examined the size distributions of soil derived aerosols. Under conditions of heavy aerosol loading, they conclude that there are two distinct size modes present. The two modes are log normally distributed. The smaller mode has a peak near 1-μm particle diameter and seems to be independent of the soil type. The larger mode has a peak between about 8 and 80 μm, depending on soil type. The speculation is that the smaller mode, labeled mode A by Patterson and Gillette, is due to the breaking up of the loose soil aggregates by the sandblasting process due to wind erosion. The larger mode, mode B, is due to the soil aggregates themselves. In our problem of dust lofted by a cratering explosion we would expect considerable fracturing and breaking up of the soil aggregates.

The hybrid distribution measured on the large HE and nuclear detonations appears to correspond to the mode B aerosol distribution, but with a power law tail for the explosively ejected larger particles (which are not present in the wind driven aerosols). The mode A particles were not measured in that particular series of tests, but have been measured in some late time nuclear dust clouds. Dust cloud samplers mounted on aircraft have measured the size statistics of dust particles in nuclear dust clouds at times several hours after detonation. At these late times particles from mode A are the dominant dust constituent in the cloud.

For our size model, we adopt the two mode distribution. We assume there are two distinct size groups present, the mode A and mode B particles. We take the mode A particles to be log normally distributed, and the mode B particles to have the hybrid distribution. Table 18 gives

83

Table 18 . Size probability distribution parameters.

Mode	Probability Distribution	Soils	Size Parameters	
A	Log normal	All	$a_m = 10^{-4}$ cm (1 μm)	
			$S = 2.2$	
B	Hybrid	Rock and cohesive soils	$a_m = 0.002$ cm (20 μm)	
			$S = 2$	
			$a_{min} = 0.018$ cm (180 μm)	
			$a_{max} = 1$ cm	
			$p = 3.5$	
		Unconsolidated soils	$a_m = 0.002$ cm (20 μm)	
			$S = 2$	
			$a_{min} = 0.018$ cm (180 μm)	
			$a_{max} = 1$ cm	
			$p = 4.0$	

the presently recommended values for the probability distribution parameters (References 15 and 16). Figure 25 shows the probability distributions. The mode curves shown are probability curves; that is, the area under each curve is unity. The fraction of the lofted dust mass that is in each size mode can be determined by direct size measurements or by the indirect transmission data. For wavelengths of a few microns or less, the two modes have significantly different scattering and absorption properties per gram of dust mass. If we have an estimate of the total dust mass in the cloud, then the mass fraction in each mode can be varied until a match with the transmission data is obtained.
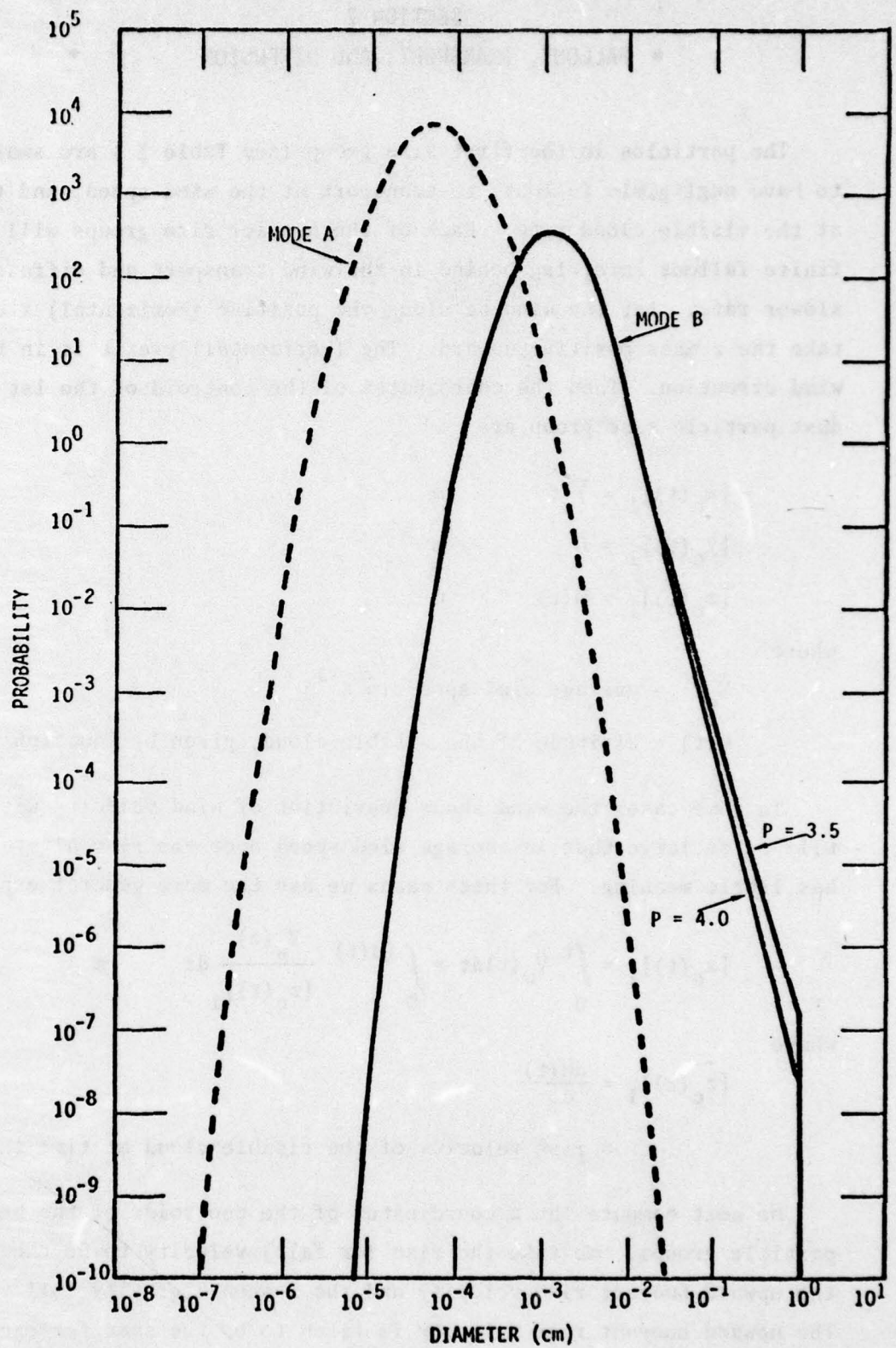
Figure 25. Particle size probability distributions.

SECTION 7
FALLOUT, TRANSPORT, AND DIFFUSION

The particles in the first size group (see Table 3) are small enough to have negligible fallout, to transport at the wind speed, and to diffuse at the visible cloud rate. Each of the heavier size groups will have a finite fallout rate, lag behind in the wind transport and diffuse at a slower rate. Let the wind be along the positive (horizontal) x axis and take the z axis positive upward. The (horizontal) y-axis is in the cross wind direction. Then the coordinates of the centroid of the 1st (smallest) dust particle size group are

$$[x_c(t)]_1 = \overline{V}_w t \qquad m \tag{79a}$$

$$[y_c(t)]_1 = 0 \qquad m \tag{79b}$$

$$[z_c(t)]_1 = H(t) \qquad m \tag{79c}$$

where

$\overline{V}_w$ = average wind speed (m s^{-1}).

$H(t)$ = altitude of the visible cloud, given by Equation 24 (m).

In some cases the wind shear (variation of wind velocity with altitude) will be so large that an average wind speed over the rise altitude range has little meaning. For these cases we use the more general expression

$$[x_c(t)]_1 = \int_0^t V_w(t)dt = \int_0^{(H(t)} \frac{V_w(z)}{[\dot{z}_c(t)]_1} dz \qquad m \tag{80}$$

where

$$[\dot{z}_c(t)]_1 = \frac{dH(t)}{dt}$$

= rise velocity of the visible cloud at time t (m s^{-1}).

We next compute the z coordinates of the centroids of the heavier particle groups. We take the rise (or fall) velocity to be the sum of the upward buoyant rise velocity and the downward gravity fall velocity. The upward buoyant rise velocity is taken to be the same for each size group and is equal to the visible cloud rise velocity. The downward velocity is taken as the terminal velocity under gravity fall. Thus

86

$$[\dot{z}_c(t)]_i = [\dot{z}_c(t)]_1 - (V_t)_i \quad \text{m s}^{-1} \tag{81}$$

$$[z_c(t)]_i = [z_c(t)]_1 - (V_t)_i T \quad \text{m} \tag{82}$$

where

$\quad$ i $\qquad$ = 2 to 20, the index of the particle size group

$\quad [\dot{z}_c(t)]_i$ $\quad$ = rise velocity of the centroid of size group i (m s^{-1})

$\quad (V_t)_i$ $\qquad$ = terminal velocity of size group i under gravity fall (m s^{-1})

$\quad [z_c(t)]_i$ $\quad$ = altitude of centroid of size group i (m).

The terminal velocity equation of a spherical particle falling under gravity in still air is

$$\frac{3\rho_a C_D}{4\rho_p d} V^2 - g = 0 \tag{83}$$

where

$\quad$ V = terminal fall velocity

$\quad \rho_a$ = ambient air density

$\quad \rho_p$ = particle density

$\quad$ d = diameter of spherical particle

$\quad$ g = acceleration of gravity.

For a spherical dust particle we can use (Reference 17)

$$C_D = \frac{24}{R_e} + 0.44 \tag{84}$$

where R_e is the Reynolds number, given by

$$R_e = \frac{\rho_a V d}{\mu_a} \tag{85}$$

and μ_a is the air viscosity. Thus the velocity equation becomes

$$\frac{1}{3} \frac{\rho_a}{\rho_p d} V^2 + \frac{18\mu_a}{\rho_p d^2} V - g = 0 \tag{86}$$

which has the solution

$$V = \sqrt{\left(\frac{27 \mu_a}{\rho_a d}\right)^2 + \frac{3g\rho_p d}{\rho_a}} - \frac{27\mu_a}{\rho_a d} \tag{87}$$

This terminal velocity equation is more familiar in the limits of large and small dust particles. For small dust particles ($d \leq 0.01$ cm)

$$C_D \approx \frac{24}{R_e} \quad \text{and}$$

$$V = \frac{g\rho_p d^2}{18\mu_a}$$

which is Stokes law. For large dust particles ($d \geq 0.1$ cm)

$$V = \sqrt{\frac{4\rho_p g d}{3\rho_a C_D}}$$

which is the dynamic drag equation. We assume the following numerical values for air near sea level

$$\rho_a = 1.225 \times 10^{-3} \text{ g cm}^{-3}$$
$$\rho_p = 2.6 \text{ g cm}^{-3}$$
$$g = 980.6 \text{ cm s}^{-2}$$
$$\mu_a = 1.81 \times 10^{-4} \text{ poises.}$$

With these values the terminal velocity equation becomes

$$V = \sqrt{\left(\frac{3.9894}{d}\right)^2 + 6.2438 \times 10^6 d} - \frac{3.9894}{d} \quad \text{cm s}^{-1} \tag{88}$$

where d is in cm.

Now, each size group of dust particles has a range of particle sizes in it, but we assume the whole group falls with one characteristic velocity. So we need to define a characteristic diameter to use in the

88

terminal velocity equation. We make the simple assumption that the
characteristic terminal velocity of each size group is the particle
terminal velocity of the midpoint diameter of the size group. Table
19 shows some terminal velocities in sea level air. The buoyant rise
velocity for a cloud with a hydro yield (fW) of 10 lbs of TNT is about
3 m s^{-1} at early times. For this case particles less than about 0.03 cm
(300 μm) in diameter would be carried upward for some distance until
the buoyant rise velocity slowed sufficiently. Larger particles would
begin falling immediately.

Table 19. Terminal velocities.

Particle Diameter (cm)	Terminal Velocity (m s^{-1})
0	0
0.001	0.0078
0.003	0.0702
0.006	0.276
0.01	0.718
0.03	3.20
0.06	5.49
0.1	7.51
1.0	24.9

Next we consider the horizontal transport of the larger particle
groups by the wind. We will develop the equations for the constant wind
case; for a varying wind the velocity equations are integrated as a func-
tion of time (or altitude). Let

89

$$[V_D(t)]_i = \bar{V}_w - [\dot{x}_c(t)]_i \quad m\ s^{-1} \tag{89}$$

= horizontal difference velocity for centroid of particle group i

$[\dot{x}_c(t)]_i$ = horizontal velocity of centroid of particle group i (m s^{-1}).

Eliminating the gravity term from Equation 86 , the drag force per unit mass on a spherical particle of diameter d is

$$F_D = C_1 V_D^2 + C_2 V_D \quad newtons\ kg^{-1}$$

where

$$C_1 = \frac{10^2}{3} \frac{\rho_a}{\rho_p d} \quad m^{-1} \tag{90}$$

$$C_2 = \frac{18\mu_a}{\rho_p d^2} \quad s^{-1} \ . \tag{91}$$

For constant $\bar{V}_w$,

$$F_D = \frac{d[\dot{x}_c(t)]}{dt} = -\frac{dV_D}{dt} \ .$$

Solving for V_D,

$$V_D = \frac{C_2 \bar{V}_w}{(C_2 + C_1 \bar{V}_w)\ e^{C_2 t} - C_1 \bar{V}_w} \quad m\ s^{-1} \ . \tag{92}$$

Thus

$$[\dot{x}_c(t)]_i = \bar{V}_w \left[1 - \frac{C_2}{(C_2 + C_1 \bar{V}_w)\ e^{C_2 t} - C_1 \bar{V}_w} \right] \quad m\ s^{-1} \ . \tag{93}$$

90

Integrating with respect to time,

$$[x_c(t)]_i = [x_c(t)]_1 - \frac{1}{C_1}\left[\ln\left\{\left(1 + \frac{C_1\overline{V}_w}{C_2}\right)e^{C_2 t} - \frac{C_1}{C_2}\overline{V}_w\right\} - C_2 t\right] \quad m \quad .$$

For the characteristic diameter to use in Equations 90 and 91 to evaluate C_1 and C_2 for each size group, we again take the midpoint diameter of the range. Table 20 gives some C_1 and C_2 values for sea level air and the time it takes for the particle to reach 90 percent of the wind velocity for a $5 \ m \ s^{-1}$ wind. As would be expected, the small particles rapidly approach the wind speed, while the larger particles take progressive longer times to be accelerated by the wind.

Table 20. Horizontal velocity parameters.

Particle Diameter (cm)	$C_1 \ (m^{-1})$	$C_2 \ (s^{-1})$	Time to Reach 90 Percent of Wind Speed (s)
0.001	15.7	1250	0.00180
0.003	5.24	139	0.0155
0.006	2.62	34.8	0.0580
0.01	1.57	12.5	0.150
0.03	0.524	1.39	1.02
0.06	0.262	0.348	3.05
0.1	0.157	0.125	6.44
0.3	0.0524	0.0139	26.9
0.6	0.0262	0.00348	60.2
1.0	0.0157	0.00125	106.0

The larger particles will expand and diffuse at slower rates than the smaller particles. Following Pasquill (Reference 5) we have approximately

91

$$\left. \begin{array}{c} K \\ \text{or} \\ \dfrac{d\sigma^2}{dt} \end{array} \right\} \propto \left(\dfrac{V_t^2}{\bar{u}^2} + \dfrac{1}{\beta} \right)^{-1/2} \tag{95}$$

where

$\bar{u}$ = mean air velocity (m s^{-1})

β = ratio of Lagrangian and Eulerian time scales.

For β we take an average value of 4 (Reference 5). In the model of cloud rise and expansion, there are two time regimes. In the first regime buoyant rise and expansion dominate atmospheric diffusion; in the second regime atmospheric diffusion dominates. In the first time regime we take

$$(K)_i = \dfrac{(K)_1}{\left(\dfrac{16(V_t)_i^2}{V_H^2} + 1 \right)^{1/2}} \quad m^2 \ s^{-1} \tag{96}$$

where

K = effective horizontal or vertical diffusion coefficients
(m^2 s^{-1})

V_H = initial buoyant rise velocity of cloud (m s^{-1}).

In the second time regime, we take

$$\left(\dfrac{d\sigma^2}{dt} \right)_i = \dfrac{\left(\dfrac{d\sigma^2}{dt} \right)_1}{\left(\dfrac{16 \ (V_t)_i^2}{\bar{V}_w^2} + 1 \right)^{1/2}} \quad m^2 \ s^{-1} \tag{97}$$

where

$\sigma^2 = \dfrac{R^2}{C_r^2}$ = variance in dust mass concentration in the vertical or horizontal direction (m^2)

92

Table 21. Ratios of diffusion parameters.

Particle Diameter (cm)	$\dfrac{(K)_i}{(K)_1}$, $-\dfrac{\left(\dfrac{d\sigma^2}{dt}\right)_i}{\left(\dfrac{d\sigma^2}{dt}\right)_1}$
0	1.00
0.001	1.00
0.003	0.996
0.006	0.938
0.01	0.722
0.03	0.228
0.06	0.135
0.1	0.099
1.0	0.030

Table 21 shows the ratio of the effective diffusion coefficients
or the variance derivatives for V_H or V_H equal to 3 m s^{-1}. Parti-
cles larger than about 0.006 cm (60 μm) diffuse at the full cloud
rate, while the larger particles diffuse at decreasing rates.

93

SECTION 8
SAMPLE CALCULATION

As an example, we will compare the cloud model results with the experimentally measured data for Dugway test D4. Figure 26 shows the test layout. The sight paths for transmission measurements were along rows Q, O, and M; the test instruments were located 1.5 m above ground level. The mean wind speed was 4.7 m s^{-1} (measured at 8 m) blowing from 320 degrees (about 6 degrees off vertical with respect to the sight paths). The charge was 8 lbs of TNT buried so that the charge top was flush with the ground surface. We take a wavelength of 3.4 µm for the transmission experiments.

Figures 27 and 28 show the horizontal and vertical radii for various particle sizes. Also shown on the figures are the data for the visible cloud radii which we are assuming correspond to the zero diameter particle model results. The agreement is quite reasonable. Figure 29 shows the altitude versus time for various particle sizes. We have no altitude data for comparison. Figure 30 shows the distance the various particle sizes are carried by the wind. The zero diameter particles travel with the mean wind speed. Note that we are ignoring any wind shear and simply take a constant wind speed with altitude. Again we have no data for comparison.

Since the sight paths are only 1.5 m above ground level, only the larger particles (diameter $\gtrsim$ 100 µm) will fall out of the cloud into the sight paths in the time it takes the cloud to traverse the test grid (~40 s). Hence we can ignore the minor mass in the smaller mode A particles and take the size distribution of the particles to be the hybrid distribution for unconsolidated soils of Table 18. Using the cross section routines given in the appendix, Table 22 gives a printout

94

AD-A072 281   GENERAL ELECTRIC CO SANTA BARBARA CA TEMPO   F/G 19/4
                MODELS FOR MUNITION DUST CLOUDS.(U)
                JUN 79   J H THOMPSON   DAAD07-78-C-0005
UNCLASSIFIED   GE78TMP-99   ERADCOM/ASL-CR-79-0005-2   NL

2 OF 2
AD
A072281

END
DATE
FILMED
9-79
DDC

1.0

4.5
5.0
5.6
6.3

2.8

2.5

3.2

2.2

3.6

1.1

4.0

2.0

1.8

1.25

1.4

1.6

MICROCOPY RESOLUTION TEST CHART
NATIONAL BUREAU OF STANDARDS-1963-A
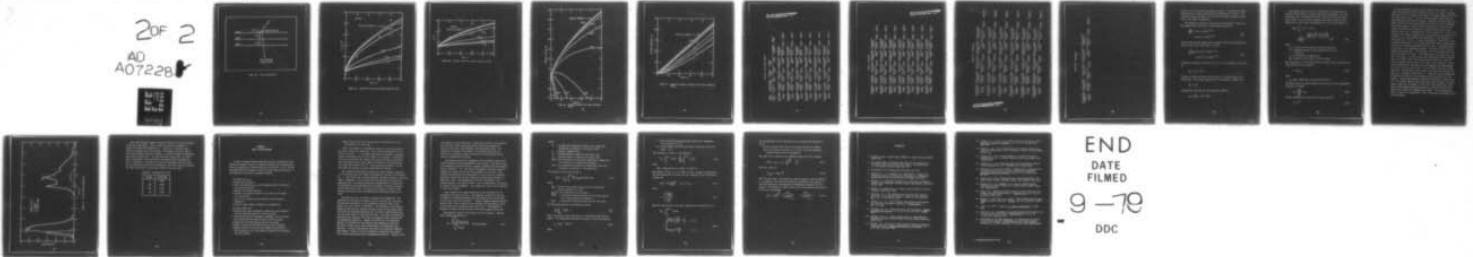
Figure 26. Test configuration.

Figure 27. Horizontal radii for various particle sizes.

96

Figure 28. Vertical radii for various particle sizes.
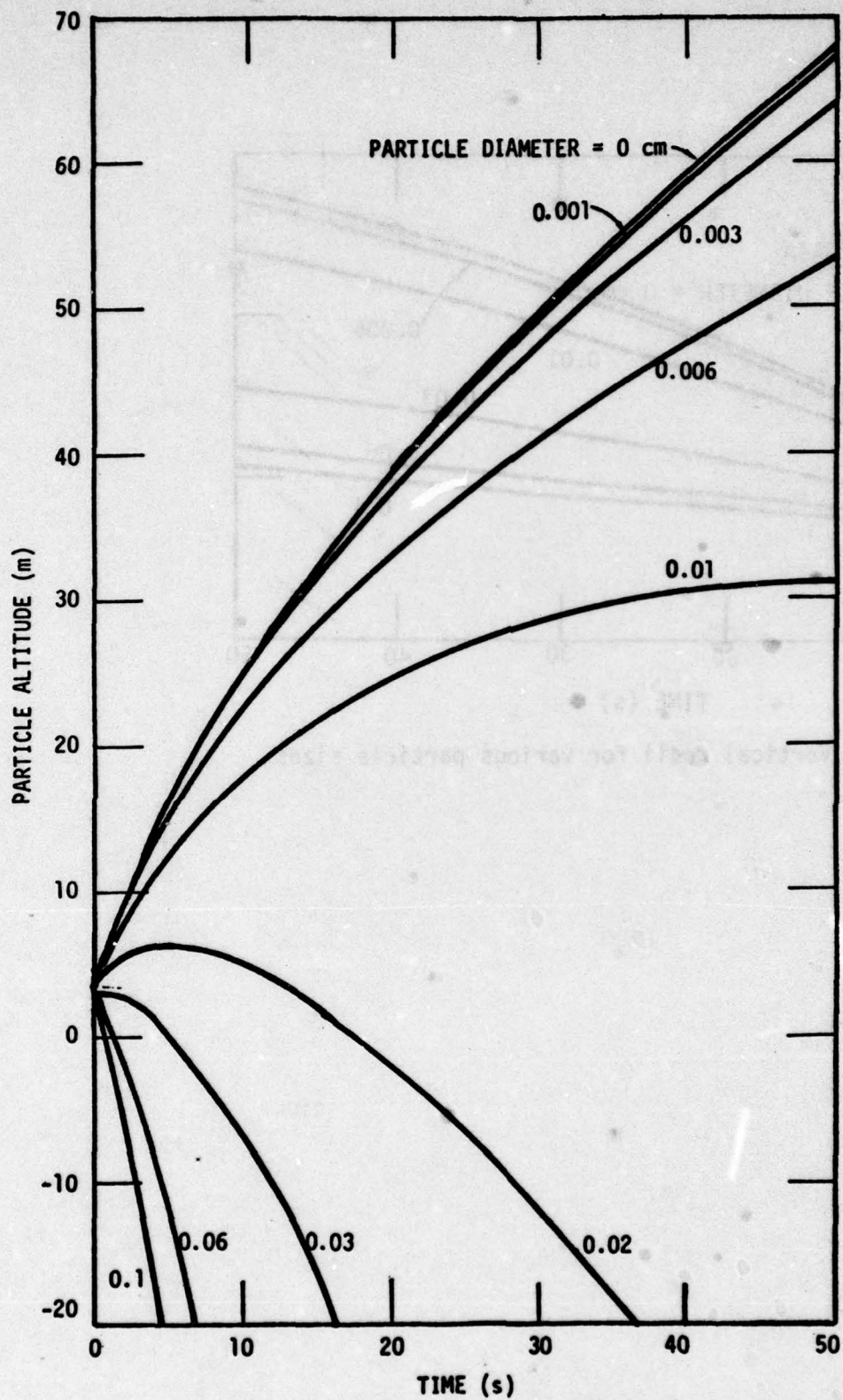
Figure 29. Altitude histories for various particle
sizes.

93
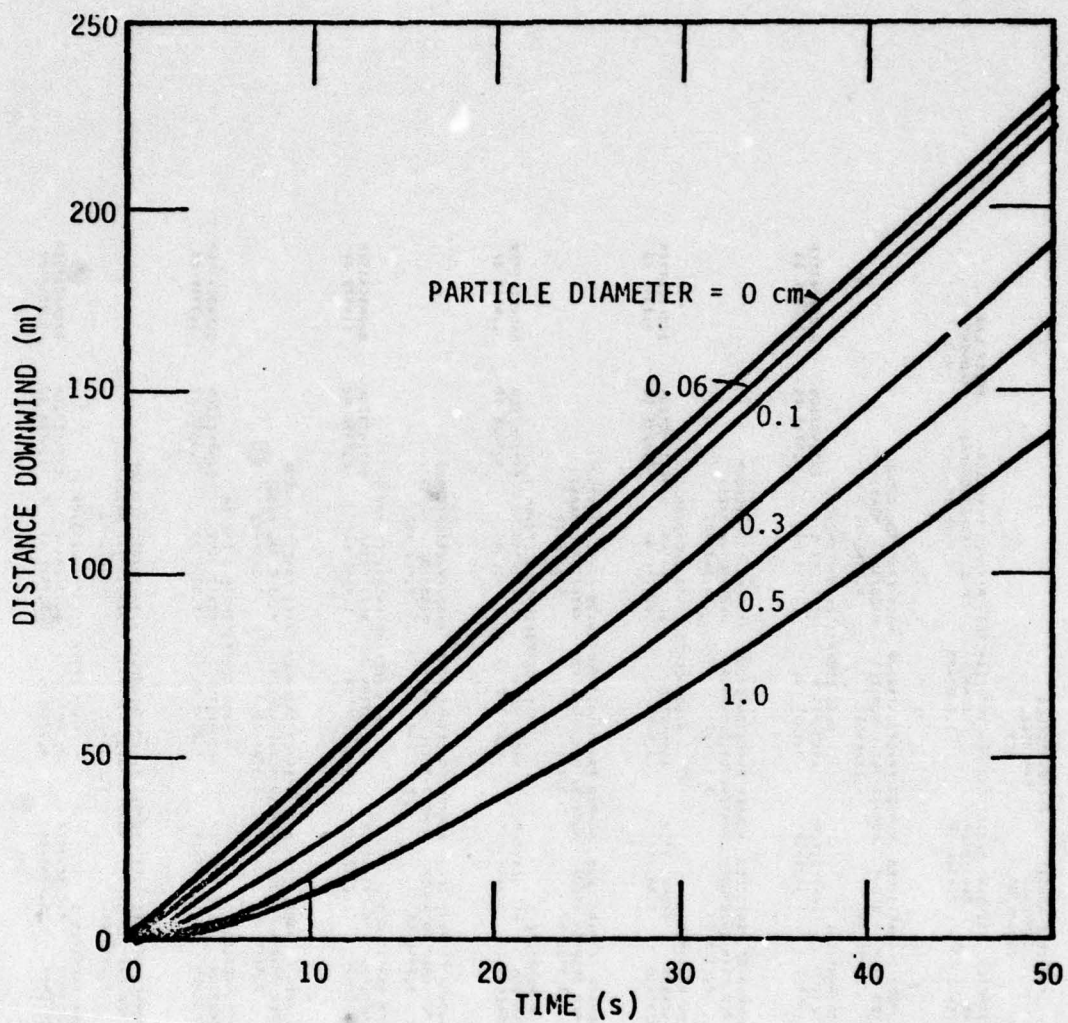
Figure 30. Downwind distance histories for various particle sizes.

Table 22. Cross section results.

```
WAVELENGTH         INDEX OF REFRACTION        PARTICLE DENSITY   ARE PARTICLES
 (CM)              REAL PART   IMAG PART        (GM/CM3)          SPHERICAL
3.803E-04          1.800E 00   1.800E-02        2.500E 00         YES

DISTRIBUTION   COMPUTE SCATTERING   MEAN DIAMETER   STANDARD DEVIATION   MERGING DIAMETER   MAXIMUM DIAMETER        POWER LAW
TYPE           PATTERN              (CM)            PARAMETER            (CM)               OF DISTRIBUTION(CM)     EXPONENT
MYBRID         NO                   2.000E-03       2.000E 00            1.000E-02          1.000E 00               4.0

MINIMUM DIAMETER   MAXIMUM DIAMETER    NUMBER OF PARTICLES   NUMBER FRACTION(GROUP   MASS FRACTION(GROUP
IN SIZE GROUP(CM)  IN SIZE GROUP(CM)   PER GRAM IN GROUP     NUMBER/TOTAL NUMBER)    MASS/TOTAL MASS)
0.                 1.000E-03           1.001E 09             1.560E-01               4.850E-04
CROSS SECTIONS ( CM2 PER PARTICLE )                          MASS COEFFICIENTS ( CM2/GM )
   SCATTERING   EXTINCTION   BACKSCATTER                       SCATTERING   EXTINCTION   BACKSCATTER
   8.833E-07    1.113E-06    1.335E-06                          3.001E 02    1.071E 03    2.204E 03
   ABSORPTION                                                  ABSORPTION
   2.290E-07                                                   3.001E 02

MINIMUM DIAMETER   MAXIMUM DIAMETER    NUMBER OF PARTICLES   NUMBER FRACTION(GROUP   MASS FRACTION(GROUP
IN SIZE GROUP(CM)  IN SIZE GROUP(CM)   PER GRAM IN GROUP     NUMBER/TOTAL NUMBER)    MASS/TOTAL MASS)
1.000E-03          2.000E-03           2.113E 08             3.412E-01               8.302E-03
CROSS SECTIONS ( CM2 PER PARTICLE )                          MASS COEFFICIENTS ( CM2/GM )
   SCATTERING   EXTINCTION   BACKSCATTER                       SCATTERING   EXTINCTION   BACKSCATTER
   3.112E-06    4.316E-06    3.851E-06                          2.545E 02    9.376E 02    6.139E 02
   ABSORPTION                                                  ABSORPTION
   1.204E-06                                                   2.545E 02

MINIMUM DIAMETER   MAXIMUM DIAMETER    NUMBER OF PARTICLES   NUMBER FRACTION(GROUP   MASS FRACTION(GROUP
IN SIZE GROUP(CM)  IN SIZE GROUP(CM)   PER GRAM IN GROUP     NUMBER/TOTAL NUMBER)    MASS/TOTAL MASS)
2.000E-03          4.000E-03           3.090E 07             3.412E-01               5.678E-02
CROSS SECTIONS ( CM2 PER PARTICLE )                          MASS COEFFICIENTS ( CM2/GM )
   SCATTERING   EXTINCTION   BACKSCATTER                       SCATTERING   EXTINCTION   BACKSCATTER
   4.871E-06    5.214E-06    5.214E-06                          2.791E 02    4.351E 02    1.011E 02
   ABSORPTION                                                  ABSORPTION
   5.209E-06                                                   1.609E 02

MINIMUM DIAMETER   MAXIMUM DIAMETER    NUMBER OF PARTICLES   NUMBER FRACTION(GROUP   MASS FRACTION(GROUP
IN SIZE GROUP(CM)  IN SIZE GROUP(CM)   PER GRAM IN GROUP     NUMBER/TOTAL NUMBER)    MASS/TOTAL MASS)
4.000E-03          6.000E-03           6.594E 06             1.021E-01               7.905E-02
CROSS SECTIONS ( CM2 PER PARTICLE )                          MASS COEFFICIENTS ( CM2/GM )
   SCATTERING   EXTINCTION   BACKSCATTER                       SCATTERING   EXTINCTION   BACKSCATTER
   2.256E-05    3.932E-05    2.271E-06                          1.624E 02    2.593E 02    1.607E 01
   ABSORPTION                                                  ABSORPTION
   1.670E-05                                                   1.105E 02

MINIMUM DIAMETER   MAXIMUM DIAMETER    NUMBER OF PARTICLES   NUMBER FRACTION(GROUP   MASS FRACTION(GROUP
IN SIZE GROUP(CM)  IN SIZE GROUP(CM)   PER GRAM IN GROUP     NUMBER/TOTAL NUMBER)    MASS/TOTAL MASS)
6.000E-03          8.000E-03           2.309E 06             3.372E-02               7.305E-02
CROSS SECTIONS ( CM2 PER PARTICLE )                          MASS COEFFICIENTS ( CM2/GM )
   SCATTERING   EXTINCTION   BACKSCATTER                       SCATTERING   EXTINCTION   BACKSCATTER
   4.374E-05    7.612E-05    1.617E-06                          1.027E 02    1.635E 02    3.798E 00
   ABSORPTION                                                  ABSORPTION
   3.438E-05                                                   8.074E 01

MINIMUM DIAMETER   MAXIMUM DIAMETER    NUMBER OF PARTICLES   NUMBER FRACTION(GROUP   MASS FRACTION(GROUP
IN SIZE GROUP(CM)  IN SIZE GROUP(CM)   PER GRAM IN GROUP     NUMBER/TOTAL NUMBER)    MASS/TOTAL MASS)
8.000E-03          1.000E-02           1.000E 06             1.203E-02               5.901E-02
CROSS SECTIONS ( CM2 PER PARTICLE )                          MASS COEFFICIENTS ( CM2/GM )
   SCATTERING   EXTINCTION   BACKSCATTER                       SCATTERING   EXTINCTION   BACKSCATTER
   7.153E-05    1.291E-04    5.036E-06                          7.791E 01    1.400E 02    5.485E 00
   ABSORPTION                                                  ABSORPTION
   5.757E-05                                                   6.271E 01
```
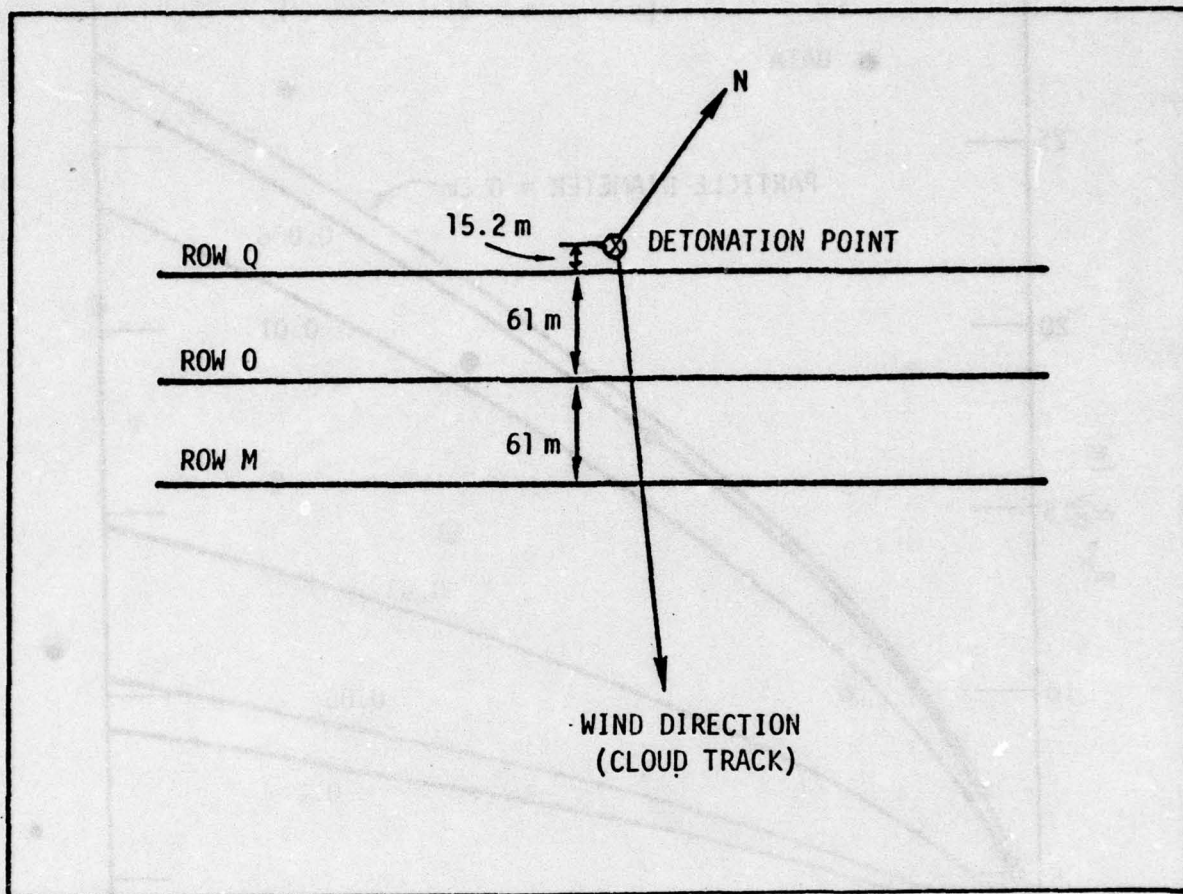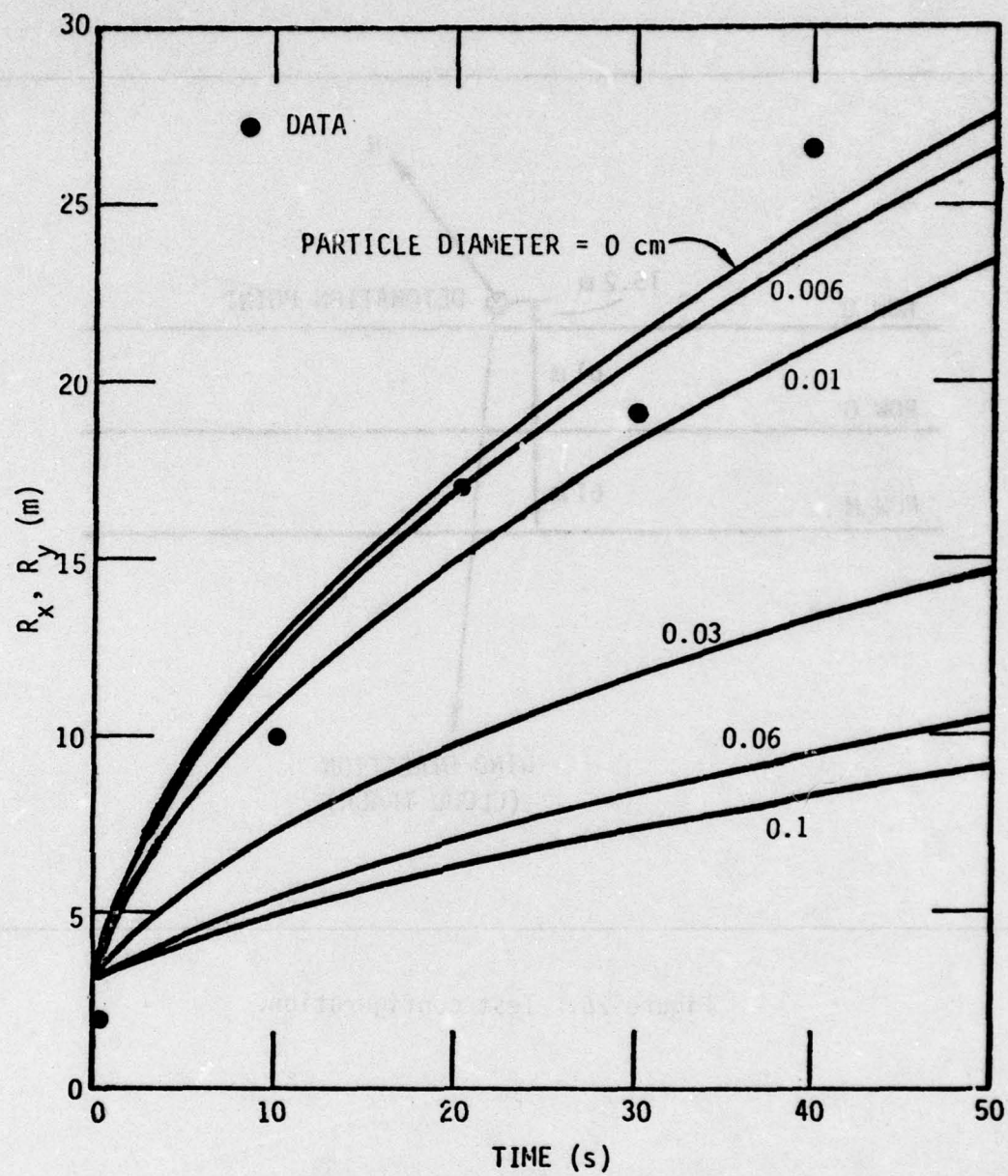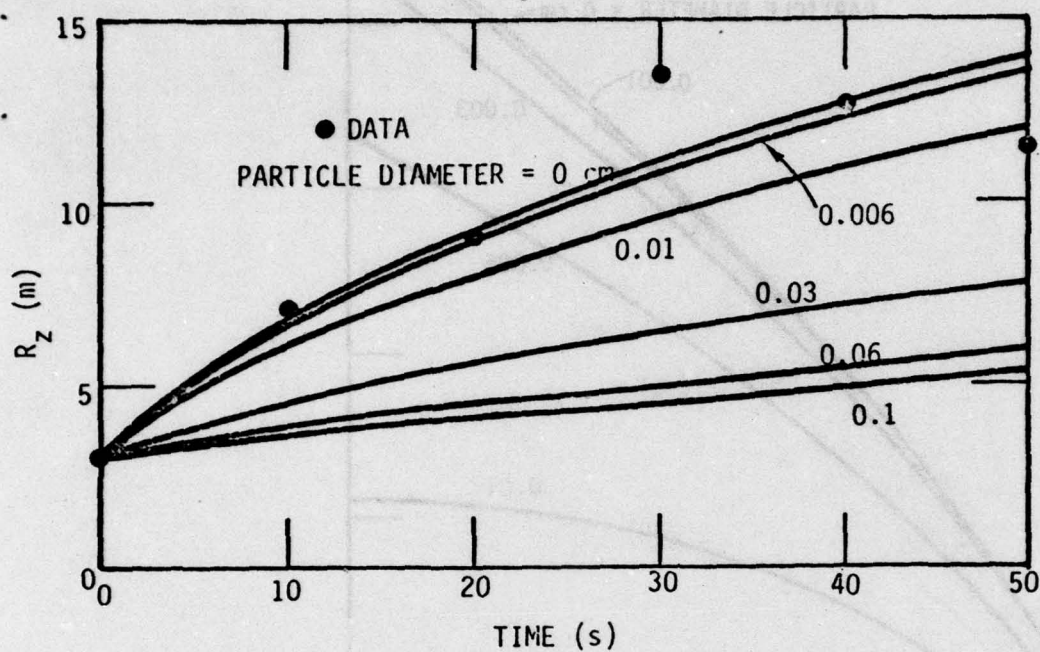
100

Table 22. Continued.

MINIMUM DIAMETER IN SIZE GROUP(CM)	MAXIMUM DIAMETER IN SIZE GROUP(CM)	NUMBER OF PARTICLES PER GRAM IN GROUP	NUMBER FRACTION(NUMBER/TOTAL NUMBER)	MASS FRACTION(GROUP MASS/TOTAL MASS)
1.000E-02	2.000E-02	3.550E 05	9.093E-03	1.603E-01

CROSS SECTIONS (CM2 PER PARTICLE)			MASS COEFFICIENTS (CM2/GM)			
SCATTERING	EXTINCTION	BACKSCATTER	ABSORPTION	SCATTERING	EXTINCTION	BACKSCATTER
1.441E-08	2.602E-04	8.007E-06	4.120E 01	5.120E 01	9.249E 01	2.874E 00
ABSORPTION
1.161E-04

MINIMUM DIAMETER IN SIZE GROUP(CM)	MAXIMUM DIAMETER IN SIZE GROUP(CM)	NUMBER OF PARTICLES PER GRAM IN GROUP	NUMBER FRACTION(GROUP NUMBER/TOTAL NUMBER)	MASS FRACTION(GROUP MASS/TOTAL MASS)
2.000E-02	3.000E-02	5.520E 04	6.490E-04	6.028E-02

CROSS SECTIONS (CM2 PER PARTICLE)			MASS COEFFICIENTS (CM2/GM)			
SCATTERING	EXTINCTION	BACKSCATTER	ABSORPTION	SCATTERING	EXTINCTION	BACKSCATTER
5.170E-03	9.335E-04	2.923E-05	2.301E 01	2.856E 01	5.157E 01	1.015E 00
ABSORPTION
4.165E-05

MINIMUM DIAMETER IN SIZE GROUP(CM)	MAXIMUM DIAMETER IN SIZE GROUP(CM)	NUMBER OF PARTICLES PER GRAM IN GROUP	NUMBER FRACTION(GROUP NUMBER/TOTAL NUMBER)	MASS FRACTION(GROUP MASS/TOTAL MASS)
3.000E-02	4.000E-02	1.895E 04	1.575E-04	8.273E-02

CROSS SECTIONS (CM2 PER PARTICLE)			MASS COEFFICIENTS (CM2/GM)			
SCATTERING	EXTINCTION	BACKSCATTER	ABSORPTION	SCATTERING	EXTINCTION	BACKSCATTER
1.602E-03	1.917E-03	6.004E-05	1.021E 01	2.013E 01	3.034E 01	1.113E 00
ABSORPTION
4.355E-05

MINIMUM DIAMETER IN SIZE GROUP(CM)	MAXIMUM DIAMETER IN SIZE GROUP(CM)	NUMBER OF PARTICLES PER GRAM IN GROUP	NUMBER FRACTION(NUMBER/TOTAL NUMBER)	MASS FRACTION(GROUP MASS/TOTAL MASS)
4.000E-02	5.000E-02	8.702E 03	5.600E-05	3.314E-02

CROSS SECTIONS (CM2 PER PARTICLE)			MASS COEFFICIENTS (CM2/GM)			
SCATTERING	EXTINCTION	BACKSCATTER	ABSORPTION	SCATTERING	EXTINCTION	BACKSCATTER
1.289E-03	3.231E-03	1.012E-04	1.254E 01	1.557E 01	2.811E 01	8.003E-01
ABSORPTION
1.441E-03

MINIMUM DIAMETER IN SIZE GROUP(CM)	MAXIMUM DIAMETER IN SIZE GROUP(CM)	NUMBER OF PARTICLES PER GRAM IN GROUP	NUMBER FRACTION(GROUP NUMBER/TOTAL NUMBER)	MASS FRACTION(GROUP MASS/TOTAL MASS)
5.000E-02	6.000E-02	4.707E 03	2.479E-05	2.708E-02

CROSS SECTIONS (CM2 PER PARTICLE)			MASS COEFFICIENTS (CM2/GM)			
SCATTERING	EXTINCTION	BACKSCATTER	ABSORPTION	SCATTERING	EXTINCTION	BACKSCATTER
2.609E-03	4.877E-03	1.526E-04	1.025E 01	1.270E 01	2.295E 01	7.163E-01
ABSORPTION
2.176E-03

MINIMUM DIAMETER IN SIZE GROUP(CM)	MAXIMUM DIAMETER IN SIZE GROUP(CM)	NUMBER OF PARTICLES PER GRAM IN GROUP	NUMBER FRACTION(GROUP NUMBER/TOTAL NUMBER)	MASS FRACTION(GROUP MASS/TOTAL MASS)
6.000E-02	7.000E-02	2.752E 03	1.261E-05	2.290E-02

CROSS SECTIONS (CM2 PER PARTICLE)			MASS COEFFICIENTS (CM2/GM)			
SCATTERING	EXTINCTION	BACKSCATTER	ABSORPTION	SCATTERING	EXTINCTION	BACKSCATTER
3.790E-03	6.045E-03	2.143E-04	8.645E 00	1.073E 01	1.934E 01	6.000E-01
ABSORPTION
3.053E-03

MINIMUM DIAMETER IN SIZE GROUP(CM)	MAXIMUM DIAMETER IN SIZE GROUP(CM)	NUMBER OF PARTICLES PER GRAM IN GROUP	NUMBER FRACTION(GROUP NUMBER/TOTAL NUMBER)	MASS FRACTION(GROUP MASS/TOTAL MASS)
7.000E-02	8.000E-02	1.455E 03	7.078E-06	1.905E-02

CROSS SECTIONS (CM2 PER PARTICLE)			MASS COEFFICIENTS (CM2/GM)			
SCATTERING	EXTINCTION	BACKSCATTER	ABSORPTION	SCATTERING	EXTINCTION	BACKSCATTER
5.003E-03	8.102E-03	2.003E-04	7.445E 00	9.292E 00	1.678E 01	5.253E-01
ABSORPTION
4.079E-03

101

Table 22. Continued.

Block 1

MINIMUM DIAMETER IN SIZE GROUP(CM)	MAXIMUM DIAMETER IN SIZE GROUP(CM)	NUMBER OF PARTICLES PER GRAM IN GROUP	NUMBER FRACTION(GROUP NUMBER/TOTAL NUMBER)	MASS FRACTION(GROUP MASS/TOTAL MASS)
8.000E-02	9.000E-02	1.257E 03	4.276E-06	1.749E-02

CROSS SECTIONS (CM2 PER PARTICLE)				MASS COEFFICIENTS (CM2/GM)			
SCATTERING	EXTINCTION	BACKSCATTER	ABSORPTION	SCATTERING	EXTINCTION	BACKSCATTER	ABSORPTION
6.515E-03	1.177E-02	3.060E-04	5.251E-03	8.193E 00	1.079E 01	4.033E-01	6.600E 00

Block 2

MINIMUM DIAMETER IN SIZE GROUP(CM)	MAXIMUM DIAMETER IN SIZE GROUP(CM)	NUMBER OF PARTICLES PER GRAM IN GROUP	NUMBER FRACTION(GROUP NUMBER/TOTAL NUMBER)	MASS FRACTION(GROUP MASS/TOTAL MASS)
9.000E-02	1.000E-01	4.085E 02	2.734E-06	1.565E-02

CROSS SECTIONS (CM2 PER PARTICLE)				MASS COEFFICIENTS (CM2/GM)			
SCATTERING	EXTINCTION	BACKSCATTER	ABSORPTION	SCATTERING	EXTINCTION	BACKSCATTER	ABSORPTION
8.150E-03	1.073E-02	4.611E-04	6.570E-03	7.328E 00	1.323E 01	4.165E-01	5.903E 00

Block 3

MINIMUM DIAMETER IN SIZE GROUP(CM)	MAXIMUM DIAMETER IN SIZE GROUP(CM)	NUMBER OF PARTICLES PER GRAM IN GROUP	NUMBER FRACTION(GROUP NUMBER/TOTAL NUMBER)	MASS FRACTION(GROUP MASS/TOTAL MASS)
1.000E-01	2.000E-01	3.215E 02	6.336E-06	1.030E-01

CROSS SECTIONS (CM2 PER PARTICLE)				MASS COEFFICIENTS (CM2/GM)			
SCATTERING	EXTINCTION	BACKSCATTER	ABSORPTION	SCATTERING	EXTINCTION	BACKSCATTER	ABSORPTION
1.55?E-02	2.915E-02	4.810E-04	1.256E-02	5.012E 00	9.050E 00	2.834E-01	4.038E 00

Block 4

MINIMUM DIAMETER IN SIZE GROUP(CM)	MAXIMUM DIAMETER IN SIZE GROUP(CM)	NUMBER OF PARTICLES PER GRAM IN GROUP	NUMBER FRACTION(GROUP NUMBER/TOTAL NUMBER)	MASS FRACTION(GROUP MASS/TOTAL MASS)
2.000E-01	4.000E-01	4.013E 01	8.004E-07	1.030E-01

CROSS SECTIONS (CM2 PER PARTICLE)				MASS COEFFICIENTS (CM2/GM)			
SCATTERING	EXTINCTION	BACKSCATTER	ABSORPTION	SCATTERING	EXTINCTION	BACKSCATTER	ABSORPTION
6.237E-02	1.126E-01	3.526E-03	5.024E-02	2.506E 00	4.525E 00	1.417E-01	2.019E 00

Block 5

MINIMUM DIAMETER IN SIZE GROUP(CM)	MAXIMUM DIAMETER IN SIZE GROUP(CM)	NUMBER OF PARTICLES PER GRAM IN GROUP	NUMBER FRACTION(GROUP NUMBER/TOTAL NUMBER)	MASS FRACTION(GROUP MASS/TOTAL MASS)
4.000E-01	6.000E-01	6.906E 00	8.087E-08	6.023E-02

CROSS SECTIONS (CM2 PER PARTICLE)				MASS COEFFICIENTS (CM2/GM)			
SCATTERING	EXTINCTION	BACKSCATTER	ABSORPTION	SCATTERING	EXTINCTION	BACKSCATTER	ABSORPTION
2.068E-01	3.734E-01	1.169E-02	1.666E-01	1.428E 00	2.578E 00	8.074E-02	1.150E 00

Block 6

MINIMUM DIAMETER IN SIZE GROUP(CM)	MAXIMUM DIAMETER IN SIZE GROUP(CM)	NUMBER OF PARTICLES PER GRAM IN GROUP	NUMBER FRACTION(GROUP NUMBER/TOTAL NUMBER)	MASS FRACTION(GROUP MASS/TOTAL MASS)
6.000E-01	8.000E-01	2.360E 00	1.069E-08	4.277E-02

CROSS SECTIONS (CM2 PER PARTICLE)				MASS COEFFICIENTS (CM2/GM)			
SCATTERING	EXTINCTION	BACKSCATTER	ABSORPTION	SCATTERING	EXTINCTION	BACKSCATTER	ABSORPTION
4.244E-01	7.670E-01	2.402E-02	3.422E-01	1.000E 00	1.817E 00	5.690E-02	8.107E-01

Table 22. Continued.

MINIMUM DIAMETER IN SIZE GROUP(CM)	MAXIMUM DIAMETER IN SIZE GROUP(CM)	NUMBER OF PARTICLES PER GRAM IN GROUP	NUMBER FRACTION(GROUP NUMBER/TOTAL NUMBER)	MASS FRACTION(GROUP MASS/TOTAL MASS)
8.000E-01	1.000E 00	1.08RE 00	7.010E-09	3.314E-02

	CROSS SECTIONS (CM2 PER PARTICLE)		
ABSORPTION	SCATTERING	EXTINCTION	BACKSCATTER
5.765E-01	7.15?E-01	1.292E 00	4.047E-02

	MASS COEFFICIENTS (CM2/GM)		
ABSORPTION	SCATTERING	EXTINCTION	BACKSCATTER
6.271E-01	7.765E-01	1.404E 00	4.602E-02

of the results for the 20 size groups of Table 3. The index of refraction chosen is a typical value for soils (References 21 and 22). For particles larger than about 30 μm the cross sections are quite insensitive to the index of refraction.

The charges are buried so that the top of the charge is flush with the ground level; this gives a scaled depth of burst of

$$\frac{DOB}{W^{1/3}} = 0.04 \text{ m (1b TNT)}^{-1/3}$$

$$= 0.131 \text{ ft (1b TNT)}^{-1/3} \qquad . \tag{98}$$

If we assume that the Dugway soil is similar to NTS area 10 alluvium or Utah dry sand, then from Figures 16 and 18

$$\frac{V_A}{W^{1.111}} \approx 0.60 \text{ ft}^3 \text{ (1b TNT)}^{-1.111}$$

$$= 0.0170 \text{ m}^3 \text{ (1b TNT)}^{-1.111} \qquad . \tag{99}$$

Assuming an average soil density of 1.5 g cm^{-3}, the apparent crater mass is

$$M_A = 2.57 \times 10^5 \text{ g} \qquad .$$

We have a limited set of data for the ratio of the total mass to apparent mass. The average value for the 5 cases shown in Table 17 is

$$\overline{F}_T = 1.68 \qquad .$$

Assuming this value for F_T, the total mass lofted is

$$M_T = F_T M_A = 4.32 \times 10^5 \text{ g} \qquad .$$

The Gaussian form for the mass distribution is particularly convenient for horizontal or vertical sight path integrations. The test grid sight paths are horizontal and are essentially along the y-axis of the cloud. Hence the mass penetrated (CL value) along the row Q sight path for the volume corresponding to one of the size groups is

$$M_{PQ} = \int_{-\infty}^{\infty} \rho(X, Y, Z) \, dy$$

$$= \frac{F_m M_T}{2\pi\sigma_x\sigma_y} e^{-\frac{1}{2}\left[\left(\frac{X_C - X_Q}{\sigma_x}\right)^2 + \left(\frac{Z_C - Z_Q}{\sigma_z}\right)^2\right]} \quad \text{g m}^{-2} \tag{101}$$

where

X_C = X-coordinate of centroid of particle group (m)

σ_x = standard deviation of mass concentration in the X direction

X_Q = X-coordinate of sightpath (m)

F_M = fraction of total mass in the size group.

The contribution to the extinction optical depth of the cloud along the sight path for the size group is

$$\tau = M_{PQ} \, \mu_E \tag{102}$$

where

μ_E = mass coefficient for extinction $(\text{m}^2 \, \text{g}^{-1})$.

The total extinction optical depth is then the sum of the contributions from each size group

$$\tau_T = \sum_{i=1}^{20} (\tau)_i \tag{103}$$

and the transmission is given by the usual expression

$$T = e^{-\tau_T} . \tag{104}$$

105

We have computed the total optical depth for rows Q and M. The cloud crosses row Q at early times and row M at later times. We would expect that the cloud fallout would reduce the optical depth by the time the cloud reaches row M. Figure 31 shows the model results and the experimentally measured optical depths. Compared to the test data, the model results are lower in magnitude and narrower in time distribution. The general behavior of both the model and the data is what we would expect—the early line of sight has a higher narrower time history than the later line. Considering all of the uncertainties in the crater volumes, mass loadings, fallout rates, mass distributions, particle size statistics, and cross sections the disagreement in the magnitudes is not surprising. In fact it is quite encouraging to achieve this level of magnitude agreement with an untuned model (the model parameters have not been set to maximize agreement with the data). The disagreement in time spread is more fundamental however. The model cloud is not wide enough near ground level. The expansion rates of the larger particles may be depressed excessively. The assumed model rise rate of the cloud may be too large. A slower rising cloud would both increase the magnitude of the model results and increase the time duration. When the test rise data become available, this effect can be examined. A more likely explanation is that both the extra magnitude and time duration are due to a low-lying dust layer. The dust model implicitly assumes that when a falling dust particle impacts the ground the particle stays there (ie, we assume a sticky earth). A large dust particle impacting the ground can break up or scour additional dust particles from the surface. Smaller dust particles impacting the ground may simply bounce off. The surface wind can carry these dust particles along. The test line of sight was low enough (1.5 m) to be in the surface dust layer. When the photography data become available we should be able to tell which effect caused the lengthened time effect. If the surface dust layer is found to be significant, a dust layer model can be added to the dust cloud model.

DUGWAY TEST D4
$\lambda = 3.4\ \mu m$
—— DATA
--- CLOUD MODEL
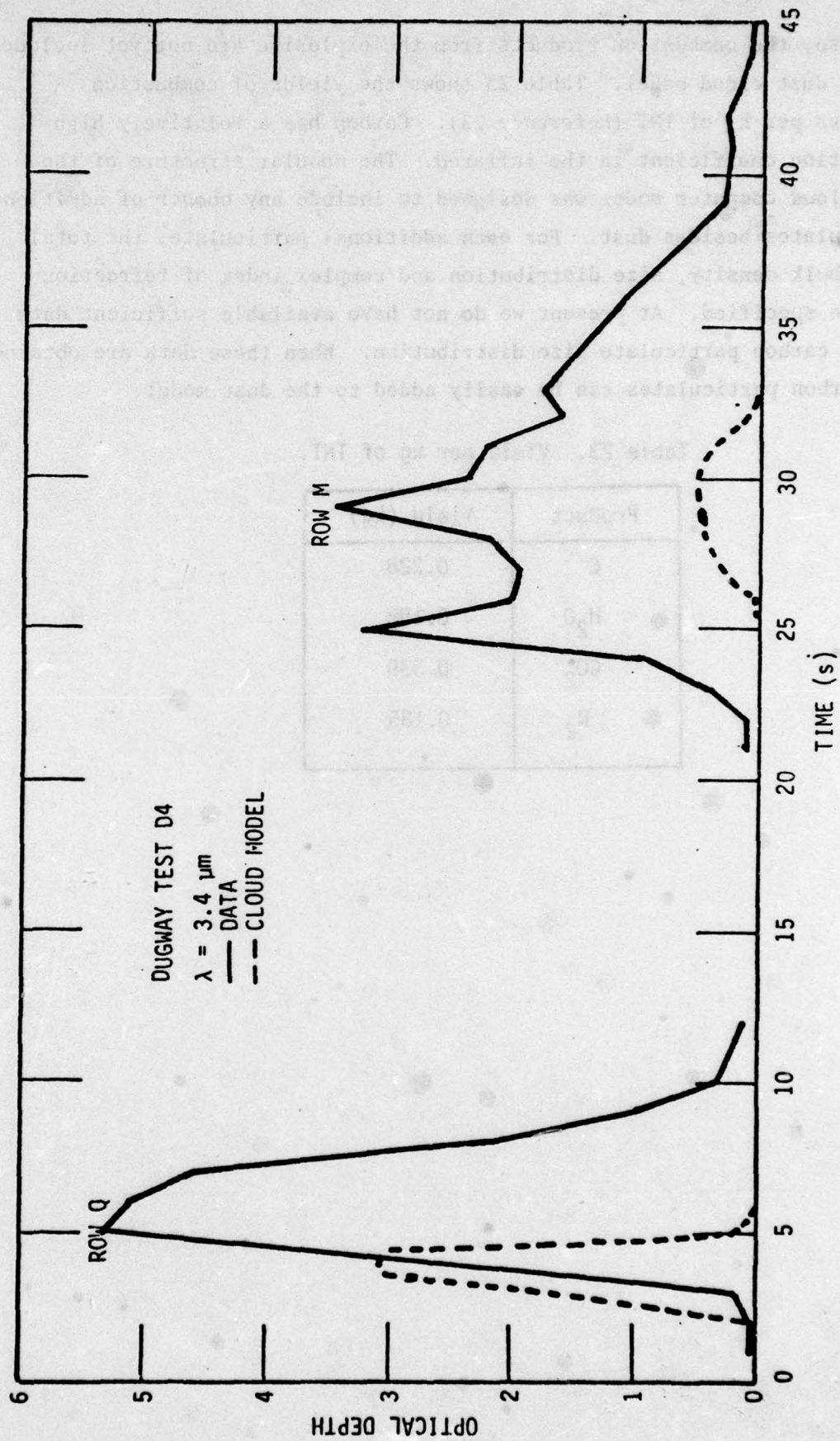
ROW Q

ROW M

OPTICAL DEPTH

TIME (s)

Figure 31. Optical depth comparisons.

Also, the combustion products from the explosive are not yet included in the dust cloud model. Table 23 shows the yields of combustion products per kg of TNT (Reference 23). Carbon has a relatively high extinction coefficient in the infrared. The modular structure of the dust cloud computer model was designed to include any number of additional particulates besides dust. For each additional particulate, the total mass, bulk density, size distribution and complex index of refraction must be specified. At present we do not have available sufficient data on the carbon particulate size distribution. When these data are obtained, the carbon particulates can be easily added to the dust model.

Table 23. Yield per kg of TNT.

Product	Yield (kg)
C	0.228
H_2O	0.198
CO_2	0.339
N_2	0.185

APPENDIX
CROSS SECTION ROUTINES

In order to compare model predictions with the experimental trans-
mission and radiance results, we need to calculate the scattering and
absorbing properties of the dust particles in the dust cloud. We have
developed generalized computer routines to make these calculations. In
this appendix we describe the program routines.

The code inputs are:
- Radiation wavelength
- Real and imaginary parts of the complex index of refraction
  of the dust particles
- Density of the dust particles
- Minimum and maximum diameters of the particle size group
  to be calculated
- Type of size probability distribution and distribution
  parameters
- Particle shape (whether spherical or nonspherical).

The code outputs are:
- Average scattering, backscatter, absorption, and extinction
  cross sections per particle in the size group
- Average scattering, backscatter, absorption, and extinction
  mass coefficients per gram of dust in the size group
- Normalized scattering pattern for the size group
- Number of particles per gram of mass in the size group
- Number fraction—the ratio of the number of particles in
  the size group to the total number of particles in the whole
  size distribution

● Mass fraction—the ratio of the mass of the particles in the
size group to the total mass.

Three size probability distributions are built into the routines—
log normal, power law, and hybrid. These three distributions are dis-
cussed in Section 6. Any other probability distribution including a
tabular distribution can be easily added to the program. The program
is set up to calculate the outputs for a given size group of particles.
This size group can be a small subset of the whole size distribution,
as in the case of one of our 20 dust particle size groups. Or the
size group can include the whole probability distribution.

The standard Mie calculation routine for single spherical particles
is a new routine which was recently developed for the WOE code (Reference
18). The routine uses a stable backwards recursion technique, utilizing
Lentz's (Reference 19) continued fraction algorithm to evaluate the
beginning term. The backward recursion technique does not suffer from
the instabilities and inaccuracies of the forward recursion techniques
of many earlier Mie codes. The present Mie routine is compact, fast
running, and accurate for any combination of wavelengths and particle
sizes.

Dust particles are, in general, irregular and nonspherical. The
spherical Mie solutions are normally used to calculate the scattering
and absorption properties of any nonspherical particle that is not
planar (ie, flat, such as a snowflake). The rationale is that the non-
spherical particles are randomly oriented so that on the average their
scattering and absorbing properties are the same as spherical particles
with the same volume or cross sectional area. For total scattering and
absorbing cross sections, the results are generally quite accurate for
the nonspherical particles. However, the details of the scattering
pattern are different for the spherical and nonspherical particles.
The back and side scatter from a distribution of nonspherical dust
particles can differ significantly from that of an equivalent spherical
distribution. There are various techniques available for the calcula-
tion of the scattering pattern of nonspherical particles. Pinnick, et al,

110

in Reference 20 have shown that a simple modification to the standard Mie solutions yields scattering pattern results for nonspherical particles that are in good agreement with experimental data. The modification eliminates the effects of the surface waves that are present in scattering by spherical particles but are absent in scattering by nonspherical particles.

A preliminary version for nonspherical Mie calculation based on the Pinnick method has been incorporated in the routines. The outputs from the nonspherical calculations are in general agreement with the examples given in Reference 20. But further development is needed before the nonspherical option can be used with confidence in all cases. The routines described here were developed as a tool to use for comparing measured transmissions with the calculated transmissions through the model dust cloud. The development of the dust cloud model is the primary purpose of the present effort. Thus, minimum effort was devoted to the Mie routine development. The nonspherical option can be improved in some future effort.

A new variable step length algorithm has been developed for the integration over particle sizes. The algorithm accounts for the rate of change of integrand magnitude with step length and the contribution of the step to the total integral. A rapidly changing integrand requires smaller steps, while a portion of the integral that contributes little to the total can be calculated with larger steps. The algorithm is designed to produce maximum accuracy with minimum computational time.

The equations solved in the routines are the following The mean cross section per particle is

$$\bar{\sigma} = \frac{\int_{a_1}^{a_2} \frac{\pi a^2}{4} Q(a)P(a)da}{\int_{a_1}^{a_2} P(a)da} \quad \text{cm}^2 \text{ per particle} \quad \text{(A-1)}$$

111

where

$\bar{\sigma}$ = average cross section per particle for scattering, backscatter, absorption, or extinction (cm^2)

a   = particle diameter (cm)

a_1 = minimum diameter of particle size group (cm)

a_2 = maximum diameter of particle size group (cm)

Q(a) = Mie efficiency for scattering, backscatter, absorption, or extinction for a particle of diameter a

P(a) = size probability distribution (log normal, power law, or hybrid, see Section 6 for equations).

The normalized scattering pattern is

$$S_N(\theta) = \frac{1}{\bar{\sigma}_{SCA}} \int_{a_1}^{a_2} \frac{\pi a^2}{4} Q_{SCA}(a) P(a) S(\theta,a) da \qquad \text{(A-2)}$$

where

$\bar{\sigma}_{SCA}$ = average cross section per particle for scattering, given in Equation A-1 (cm^2)

$Q_{SCA}(a)$ = Mie efficiency for scattering

$S(\theta,a)$ = normalized scattering pattern at scattering angle θ for a single particle of diameter a

$S_N(\theta)$ = normalized scattering pattern for the size group.

The scattering patterns are normalized so that

$$\frac{1}{4\pi} \int_{4\pi} S(\theta) d\Omega = 1 \qquad . \qquad \text{(A-3)}$$

Hence an isotropic scattering pattern is identically unity for all angles. The coefficients per gram of material in the size group are

$$\mu = N_T \bar{\sigma} \qquad cm^2 \ g^{-1} \qquad \text{(A-4)}$$

where

112

μ = mass coefficient for scattering, backscatter, absorption, or extinction $(cm^2\ g^{-1})$

N_T = total number of particles per gram of material in the size group (g^{-1}).

The integration strategy is the following

$$I_T = \int_{a_1}^{a_2} I(a)da = \sum_{j=1}^{n} \int_{a_j}^{a_{j+1}} I(a)da \qquad (A-5)$$

where

$I(a)$ = integrand of the integral of interest.

The interval from a_1 to a_2 is broken up into a number of subintervals. For each subinterval we assume that the integrand can be described by a power law

$$I(a) = I(a_j)\left(\frac{a}{a_j}\right)^x \qquad a_j \le a \le a_{j+1} \qquad (A-6)$$

where

$$x = \frac{\ln \dfrac{I(a_{j+1})}{I(a_j)}}{\ln \dfrac{a_{j+1}}{a_j}} . \qquad (A-7)$$

Then the contribution to the total integral of this subinterval is

$$\Delta I_T = \int_{a_j}^{a_{j+1}} I(a)da$$

$$= \begin{cases} \dfrac{I(a_j)a_j}{x+1} \left[\dfrac{a_{j+1}^{x+1}}{a_j} - 1 \right] & x \ne -1 \\[20pt] I(a_j)a_j \ \ln \dfrac{a_{j+1}}{a_j} & x = -1 . \end{cases} \qquad (A-8)$$

113

The contributions of the subintervals are calculated and summed until either
  (1) the diameter limits of the size group interval are reached,
  (2) or the integral converges to its final value (the remaining unsummed subintervals are negligible).

The step size is chosen as the e-folding distance for the integrand

$$(\Delta a)_i = a_{j+1} - a_j = a_j \left[e^{\frac{1}{|x|}} - 1 \right] . \tag{A-9}$$

With this step size

$$I(a_{j+1}) = I(a_j) \, e^{\pm 1} \tag{A-10}$$

where the plus sign is for positive x and the negative sign for negative x. In addition, for those cases where the integrand is decreasing so that the subinterval contributions are decreasing, the step size is increased. The increase is taken as the ratio of the previous contribution to the last contribution

$$(\Delta a)_j = a_j \left[e^{\frac{1}{|x|}} - 1 \right] \frac{(\Delta I_T)_{j-1}}{(\Delta I_T)_{j-2}} \qquad \text{if } \frac{(\Delta I_T)_{j-1}}{(\Delta I_T)_{j-2}} > 1 . \tag{A-11}$$

114

REFERENCES

1. Thompson, James, *S-Shock Code*, GE75TMP-14, General Electric-TEMPO, March 1975.

2. *Dust Trial Phase of Inventory Smoke Munition Test (Phase IIa)*, Preliminary draft copy of Final Test Report, 7-CO-RD7-DP1-002, U.S. Army Dugway Proving Ground, May 1978.

3. Preliminary Fort Sill Munitions Test Data, May 1978.

4. Jordano, R.J., J.H. Thompson, R.R. Rutherford, B. Gambill, Jr., *Sensitivity of H.F. System Blackout Predictions to Atmospheric Parameters*, GE77TMP-16, General Electric-TEMPO, April 1977.

5. Pasquill, F., *Atmospheric Diffusion, The Dispersion of Windborne Material from Industrial and Other Sources*, 2nd Edition, John Wiley & Sons, 1974.

6. Briggs, G.A., *Plume Rise*, U.S. Atomic Energy Commission Division Technical Information, 1969.

7. Batchelor, G.K., "The Application of the Similarity Theory of Turbulence to Atmospheric Diffusion," Quart. J. Roy. Meteorol. Soc., vol 76, pp 133-146, 1950.

8. Gifford, F.A., Jr., "Use of Routine Meteorological Observations for Estimating Atmospheric Dispersion," Nuclear Safety, 2, pp 47-51, 1961.

9. Terlecky, P.M., Jr., "Mass Partition in Soil Cratering," Journal of Geophysical Research, vol 78, no 32, pp 7671-7674, November 1973.

10. Terlecky, P.M., Jr., *Crater and Mass Data for High-Explosive Cratering in Playa*, AFWL-TR-73-269, Air Force Weapons Laboratory, January 1974.

11. Vortman, L.J., "Ten Years of High Explosive Cratering Research at Sandia Laboratory," Nuclear Applications and Technology, vol 7, pp 269-304, September 1969.

12. Vortman, L.F., "Craters from Surface Explosions and Scaling Laws," *Journal of Geophysical Research*, vol 73, no 14, pp 4621-4636, July 1968.

13. Thompson, James, *Dust Cloud Modeling and Propagation Effects for Radar and Communications Codes*, GE78TMP-81, General Electric-TEMPO, October 198.

14. Layson, W.M., et al, *Nuclear Surface Burst Debris and System Vulnerability*, Vol. I, General Research Corporation, August 1969 (unpublished).

15. Gicking, D., et al, *Technology Support for Environmental Defense*, Science Applications, Inc., September 1975 (unpublished).

16. Patterson, E.M. and D.A. Gillette, "Commonalities in Measured Size Distributions for Aerosols Having a Soil-Dervied Component," *Journal of Geophysical Research*, vol 82, no 15, pp 2074-2082, May 1977.

17. Kirsch, J.W., et al, *Near-Surface Dust Cloud Phenomenology*, DNA 3962F (SSS-R-76-2827), Systems, Science, and Software, April 1976.

18. Stanton, M.J., J.H. Thompson, et al, *Nuclear-Induced Optical Phenomenology Program (1976-1977)*, General Electric-TEMPO, August 1977 (unpublished).

19. Lentz, W.J., "Generating Bessel Functions in Mie Scattering Calculations Using Continued Fractions," *Applied Optics*, vol 15, no 3, pp 668-671, March 1976.

20. Chylek, P., G.W. Grams, R.G. Pinnick, "Light Scattering by Irregular Randomly Oriented Particles," *Science*, vol 193, pp 480-482, August 1976.

21. Ivlev, L.S. and S.I. Popova, *Izv. Atmos. Oceanic Phys.* 9, 1034, 1973.

22. Patterson, E.M., "Atmospheric Extinction Between 0.55 μm and 10.6 μm Due to Soil-Dervied Aerosols," *Applied Optics*, vol 16, no 9, pp 2414-2418, September 1977.

23. Proceedings of the Smoke Symposium - II, sponsored by the Office of the Project Manager for Smoke/Obscurants at Harry Diamond Laboratories, Adelphi, Maryland, 25 & 26 April 1978 (unpublished).